

UNIVERSITY OF PÉCS

Doctoral School of Physics

Nonlinear optics and spectroscopy program

Ellipsometric study of nanostructured silicon materials

PhD Thesis

Bálint Fodor



Supervisor:

Dr. Péter Petrik

scientific advisor

PÉCS, 2018

Contents

Preface.....	1
List of frequently used acronyms.....	4
1 Overview of the ellipsometric principle.....	5
1.1 Principles of polarized light and ellipsometry	5
1.2 Optical models.....	8
1.2.1 Reflection from an interface	9
1.2.2 Reflection from a thin layer	11
1.2.3 Reflection from a multi-layer system.....	12
1.3 Data analyses and fitting	15
1.4 Ellipsometric setup and sensitivity	17
1.5 Models for the optical properties of materials	20
1.6 Effective medium theory.....	21
1.6.1 Lorentz-Lorenz equation	21
1.6.2 Maxwell-Garnett approximation	22
1.6.3 Bruggeman effective medium approximation	23
1.6.4 Birefringence, dichroism and ellipsoid shape	24
1.6.5 Limitations of effective medium theories.....	25
2 Buried cavities in ion-implanted and annealed silicon.....	26
2.1 Experimental details.....	27
2.1.1 Sample preparation details	27
1.1.1 Measurement details	27
2.2 Modelling and evaluation strategies.....	29
2.2.1 Ellipsometric modeling.....	29
2.2.2 Transmission electron microscopic analyses	32
2.3 Evaluation of as-implanted samples.....	34

2.4	Evaluation results of buried cavities	35
2.4.1	Depth resolution from transmission electron microscopy and ellipsometry	35
2.4.2	Implantation and annealing dependencies on cavity formations	37
2.5	Conclusions.....	40
3	Porous silicon layers of broad thickness range.....	44
3.1	Experimental details	46
3.1.1	Porous silicon etching conditions.....	46
3.1.2	Porous silicon oxidizing conditions	48
3.1.3	Ellipsometric measurement setup	49
3.2	Optical model development	50
3.2.1	Comparison of increasingly complex models.....	52
3.2.2	Influence of the number of sublayers	55
3.2.3	Oxidation effects	56
3.3	Evaluation results	58
3.3.1	Thin porous silicon layers	58
3.3.2	Thick porous silicon layers	60
3.3.3	Oxidized porous silicon layers	61
3.4	Conclusions.....	63
4	Anisotropic behavior of silicon-based nanostructures.....	65
4.1	Experimental details	66
4.1.1	Porous silicon layers of a broad porosity range.....	66
4.1.2	Layers formed from silicon nanowires.....	67
4.1.3	Ellipsometric measurement details	68
4.2	Revealing optical and structural anisotropy for porous silicon.....	69
4.2.1	Finding the appropriate effective medium based models.....	69
4.2.2	Characterization results	72
4.3	Characterization of silicon nanowires	75
4.3.1	Extension of Maxwell-Garnet model to the nanowires.....	75

4.3.2	Characterization results	78
4.4	Conclusions.....	80
5	Simulation of microscopic surface roughness	81
5.1	Simulation details	82
5.1.1	Stochastic surface generation	82
5.1.2	Finite element method details	84
5.1.3	Effective medium layer details.....	87
5.2	Comparison of effective medium approximation and finite element method results.	88
5.2.1	Limitations of the simulations.....	88
5.2.2	Quadratic relation between root-mean-square roughness and effective medium thickness	91
5.2.3	Revealing another correlation	92
5.3	Conclusions.....	93
	Acknowledgments.....	94
	Summary	96
	Összefoglaló	99
	List of publications	102
	Publications strictly related to the thesis.....	102
	Articles published in peer-reviewed journals:	102
	Results presented at conferences:	102
	Other publications	103
	Articles published in peer-reviewed journals:.....	103
	Results presented at conferences:	105
	Bibliography	107

Preface

Since the renowned 1959 lecture of Richard Feynman “There’s plenty of room at the bottom”, visioning the incredible possibilities of nanotechnology, enormous progress has been made in the domain. As of 2017, semiconductor manufacturing is attaining the “10 nm” process node as defined by the International Technology Roadmap for Semiconductors 2.0 [1]. It would be difficult to cite all the domains of applications that are related to nanotechnology today, and the benefits gained along the way of pursuing the “smaller, faster, lighter, denser, cheaper” concept. Rather, to give a fascinating example from my amateur chess interest: nowadays the world chess champion would not be able to win once out of 100 games against an ordinary smartphone equipped with the leading chess-software.

This incredible development of miniaturization is closely interweaved with the advances attained in “seeing” of what has been made. The ellipsometric technique has followed such a path, with most ellipsometers today being spectroscopic. Ellipsometry is an optical method based on the measurement of the change of polarization upon reflection from, or transmission through a sample. In fact, by measuring the polarization change, we obtain not only amplitude, but also phase information of the light interacting with the sample. This remarkable property enables an incredible sensitivity to the properties of thin layers, with a sub-nanometer precision, hence valued in industrial processes as an *ex situ* feedback between process steps with more and more demand for even *in situ* measurements. Although the first ellipsometer was developed by Paul Drude, in 1888, that could already be thought of as a nanoprobe device, only since the 80s can we see a boom in ellipsometric characterizations paralleling the progress in computation capabilities, with the first spectroscopic devices appearing at that time. This is explained by the fact that ellipsometry is an indirect technique, meaning that any information on the sample is obtained through the modeling and inversion of the ellipsometric

response, often through simulation and iterative fitting, and for complex optical models, fitting the measurements of spectroscopic ellipsometry (SE) is computationally intensive.

In electronics miniaturization, silicon-based semiconductor technology is approaching its theoretical limits, but silicon industry has grown to such an extent, that it would be hard to imagine the near future without the basic building block of monocrystalline silicon (c-Si). Many different c-Si based nanostructures have emerged in the last two to three decades, that are finding (potential) applications, but industrial ellipsometric characterizations remains limited because the development of highly complex optical models is challenging and often limited to academic research.

In my thesis, I aim to show the versatility of SE characterization for some c-Si-based nanostructured materials. I not only wish to increase the understanding of the fundamental properties and formation mechanisms of these materials but also hope to boost their spreading for industrial productions in any modest way by the development of ellipsometric models. In more details, the goals include the development of complex optical models to determine the most of the relevant structural information of buried cavities in Si, of porous silicon (PSi) and of silicon nanowire (SiNW) carpets for ellipsometric measurements. With the appropriate models, the description of optical anisotropy induced by structural anisotropy from PSi layers and from SiNW layers is also an aim of the thesis. Another important goal is the investigation of the correlation between the surface roughness determined by ellipsometry and that by atomic force microscopy.

In Chapter 1, I will first introduce the basics of ellipsometry and some of the more advanced modeling methods related to the thesis. Chapter 2 will be dedicated to the description of cavities formed in c-Si due to He-implantation through a screening oxide layer followed by an annealing step. Chapter 3 will show the characterization of PSi layers by optical and infrared SE. In Chapter 4, I will describe the anisotropic behavior of thin layers formed from

PSi and silicon nanowires. Chapter 5 will reveal some interesting relationships between surface roughness and ellipsometry.

My results obtained in Chapters 2–4 are the fruit of a collaboration between two laboratories to whom I have been both affiliated to: the photonics laboratory of the Institute for Technical Physics and Materials Science¹ (MFA), being part of the Hungarian Academy of Sciences, and the French GREMAN² laboratory affiliated to the François Rabelais University of Tours. The photonics laboratory has a great expertise in optical, and mostly ellipsometrical characterizations, while GREMAN has a huge experience in porous silicon synthesis, explaining the synergy and the choice of my thesis topic. The results obtained in Chapter 5 were achieved by a non-formal collaboration between MFA and Zuse Institute Berlin, where the latter provided access to their optical finite element software with helpful support.

Concerning the abbreviations and acronyms used throughout the thesis, I should note, that they first appear when defined, but for reasons of clarity, they are sometimes re-introduced in later chapters as well. The following page also lists some of the most used acronyms.

¹ MTA EK MFA, Konkoly-Thege Miklós út 29–33, H–1121, Budapest, Hungary; www.mfa.kfki.hu

² GREMAN UMR 7347, Université de Tours – CNRS – INSA, Tours, France ; greman.univ-tours.fr

List of frequently used acronyms

AFM	atomic force microscopy
AOI	angle of incidence
a-Si	amorphous silicon
B-EMA	Bruggeman effective medium approximation
CC	Cross-correlation
c-Si	single-crystal silicon
EML	effective medium layer
EMT	effective medium theory
FEM	finite element method
MG-EMA	Maxwell-Garnett effective medium approximation
MIR	mid-infrared
OPD	optical penetration depth
PSi	porous silicon
RMS(E)	root-mean-square (error)
SE	spectroscopic ellipsometry
SEM	scanning electron microscopy
SiNW	silicon nanowires
TEM	transmission electron microscopy
TMM	transfer-matrix method
UV-NIR	ultraviolet-near-infrared

1 Overview of the ellipsometric principle

The present chapter will introduce the reader to the concepts of ellipsometry focusing on the aspects essential to the understanding of the thesis. A good first encounter with the basics can be found in *Spectroscopic Ellipsometry and Reflectometry: A User's Guide* authored by H.G. Tompkins and W.A. McGahan [2]. An excellent educational book with many comprehensible illustrations was written by H. Fujiwara [3]. For the reader interested in a more profound understanding of the ellipsometric technique, the *Handbook of Ellipsometry* edited by H.G. Tompkins and E.A. Irene [4] or the book titled *Ellipsometry and Polarized Light* written by R.M.A. Azzam and N.M. Bashara [5] could be suggested. Some of the recent multidisciplinary developments can be found in *Ellipsometry at the Nanoscale* [6].

1.1 Principles of polarized light and ellipsometry

The description of our electromagnetic waves will be based on the time dependent behavior of the electric field strength at a fixed spatial point. In the whole thesis, "light wave" will mean the whole electromagnetic spectrum and not just the visible part if not explicitly stated. The electric field, displacement field, magnetic field and magnetic induction are related to each other according to the macroscopic Maxwell's equations and the constitutive material relations. We will focus on the special case of monochromatic plane waves because with these it is straightforward to calculate the optical response of many complex systems. We separate the transverse electric field vector into two perpendicular components. Generally, we choose these two components to be parallel and perpendicular to the plane of incidence. Furthermore, by introducing the complex representation for the time-harmonic solution, the complex valued

field strength components will take the following form:

$$E_{p,s}(t, r) = E_{p,s}^0 e^{i(\omega t + \delta_{p,s})} e^{-iKr}, \quad (1.1)$$

for a time (t) dependent frequency (ω) solution at the spatial location r in the propagating direction with a wavenumber K . The p and s indices indicate the parallel and the perpendicular components, respectively. $E_{p,s}^0$ are the amplitudes, while $\delta_{p,s}$ represent the initial phases of the two oscillating components. We should note that we have adopted [the optics convention for the representations, i.e. the phase of light is defined by $(\omega t - Kr + \delta)$, and the wave advances forward with an increase in the initial phase (cf. App. 2, p. 347/348 in Ref. [3]). To obtain the real valued components of the field strength, one simply takes the real part of Eq. 1.1, while intensity values are obtained by the product of E by its complex conjugate. The complex representation in fact allows a more convenient study of the polarization. Without any loss of generality, the time as well as the spatial information can be omitted. In the spirit of this simplification, we define the complex amplitudes as

$$E_{p,s} = E_{p,s}^0 e^{i\delta_{p,s}}. \quad (1.2)$$

To recover the temporal and spatial dependence we multiply Eq. 1.2 by $e^{\omega t}$ and e^{-iKr} , respectively.

The state of polarization of a plane wave can be defined by the complex polarization coefficient

$$\chi = \frac{E_p}{E_s}. \quad (1.3)$$

In Fig. 1.1, we can see the usual graphical representation of such a general polarization state. The example shows an elliptical polarization with an arbitrary ratio of the amplitudes and phase separation between the two components. The polarization vector sweeps an elliptic path on the plane perpendicular to the propagation. Assuming again the convention of the optics

community (i.e. the direction of the rotation is defined from the point of view of the receiver), the shown elliptical polarization is considered right-handed.

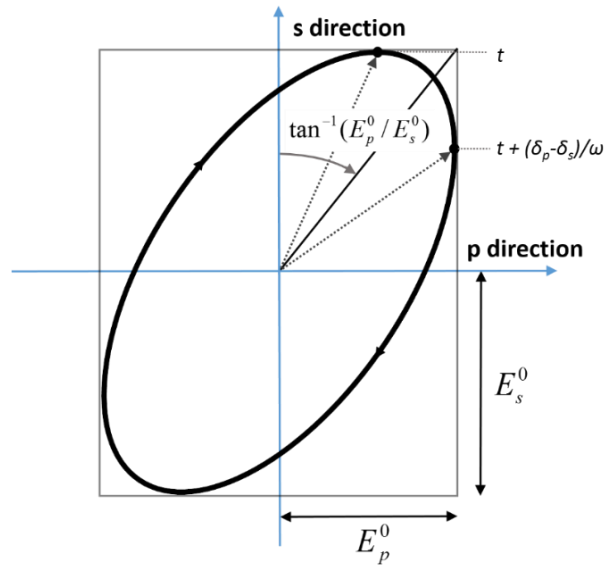


Figure 1.1: Example of a right-handed polarization ellipse taken in the coordinate system defined by the p and s directions and from the point of view of the receiver. The propagation direction is towards the reader considering the right-hand rule. The electric field strength amplitudes of the two components and the angle defined by the arctangent of the ratio of the two amplitudes are also shown.

An ellipsometric measurement describes the variation in the polarization state after the light wave has interacted with the material. To measure the ellipsometric response of a reflection, we introduce the ratio of the polarization coefficients of the reflected (index r) and incident (index i) light:

$$\rho = \frac{\chi_r}{\chi_i}. \quad (1.4)$$

This complex value describes how the shape of the polarization ellipse varies and it is equivalent to the ratio of the Fresnel reflection coefficients ($r_{p,s}$):

$$\rho = \frac{\frac{E_{r,p}}{E_{r,s}}}{\frac{E_{i,p}}{E_{i,s}}} = \frac{\frac{E_{r,p}}{E_{i,p}}}{\frac{E_{r,s}}{E_{i,s}}} = \frac{r_p}{r_s}. \quad (1.5)$$

In the late 19th century Paul Karl Drude, who made the first ellipsometric measurements, has introduced the following terminology:

$$\rho = \tan \Psi \cdot e^{i\Delta}. \quad (1.6)$$

In this notation, $\tan \Psi$ expresses the ratio of the absolute values of the reflected and incident polarization coefficients which is equivalent to the ratio of the absolute values of the p and s Fresnel-reflection coefficients:

$$\tan \Psi = \frac{|\chi_r|}{|\chi_i|} = \frac{|r_p|}{|r_s|}, \quad (1.7a)$$

while Δ describes the shift in the phase difference of the two components or which can readily be seen to be equal to the difference of the phase shifts of the two components after reflection:

$$\Delta = \delta_r - \delta_i = (\delta_{r,p} - \delta_{r,s}) - (\delta_{i,p} - \delta_{i,s}) = (\delta_{r,p} - \delta_{i,p}) - (\delta_{r,s} - \delta_{i,s}) = \Delta_p - \Delta_s, \quad (1.7b)$$

where the bi-indexed δ values are the phases of the components before and after reflection. To phrase Eq. 1.7a and b in a simpler way, we can say that Ψ and Δ indicate the differential changes in amplitude and phase during reflection. They are two independent parameters of an ellipsometric measurement and are often referred to as the ellipsometric angles, given in degrees (cf. p. 274 in Ref. [5]).

1.2 Optical models

Ellipsometry is an indirect measurement technique, meaning that any characteristic information about the investigated material is obtained through the analysis of the variation of the polarization state. Usually this requires modeling and simulation of the ellipsometric angles followed by an iterative regression analysis with free parameters. For explanatory purposes, in the following sub-sections, we will derive a few characteristic optical models of increasing complexity.

1.2.1 Reflection from an interface

The behavior of light at a planar interface between two isotropic media are governed by the Fresnel equations. The complex reflection coefficients³ for the two polarizations are stated as

$$\frac{E_{r,p}}{E_{i,p}} = r_p = \frac{\bar{N}_1 \cos \theta_0 - \bar{N}_0 \cos \theta_1}{\bar{N}_1 \cos \theta_0 + \bar{N}_0 \cos \theta_1} \text{ and} \quad (1.8a)$$

$$\frac{E_{r,s}}{E_{i,s}} = r_s = \frac{\bar{N}_0 \cos \theta_0 - \bar{N}_1 \cos \theta_1}{\bar{N}_0 \cos \theta_0 + \bar{N}_1 \cos \theta_1}, \quad (1.8b)$$

where \bar{N}_0 and \bar{N}_1 are the complex refractive indices of the two media (Medium 0 and Medium 1, respectively) separating the boundary in such a way that the plane wave is initially propagating from Medium 0 to Medium 1, as shown in Fig. 1.2. θ_0 is the angle of incidence (AOI), and θ_1 is the angle of refraction. Of course, θ_1 can be expressed with Snell's law as

$$\bar{N}_0 \sin \theta_0 = \bar{N}_1 \sin \theta_1. \quad (1.9)$$

The complex refractive indices are defined as

$$\bar{N} = n - ik, \quad (1.10)$$

where n is the real valued refractive index and k is the extinction coefficient.

In brief, if the incident wave has $\chi = 1$ (linear polarization of $\pm 45^\circ$ azimuthal rotation), ρ can be formulated as a function of the refractive indices and the AOI:

$$\rho = \frac{\bar{r}_p}{\bar{r}_s} = \rho(\bar{N}_0, \bar{N}_1, \theta_0). \quad (1.11)$$

If the index of refraction of Medium 0 is known (e.g. \bar{N}_0 for air is approximated as equal to 1 for all wavelengths) with the AOI and the incident state of polarization known from the measurement setup after appropriate calibrations, we can invert Eq. 1.11 to calculate \bar{N}_1 . In practice, for an SE measurement assuming no backside reflection, this means that from the Ψ

³ The Verdet sign convention is being used as in Refs. [2,3,5], whereas occasionally the Fresnel convention is more practical (cf. p 74 in Ref. [4]).

and Δ spectra we can obtain the optical properties of a bulk material (n and k) at the specified wavelength range. Unfortunately, in this way, any systematic and random errors as well as unmodeled structural and material properties (surface roughness, surface overlayer, inhomogeneity, etc...) are propagated to the calculated n and k values biasing them compared to the real optical properties of the bulk material. In section 1.5 of this chapter we will introduce some dispersion functions with which these errors can be reduced.

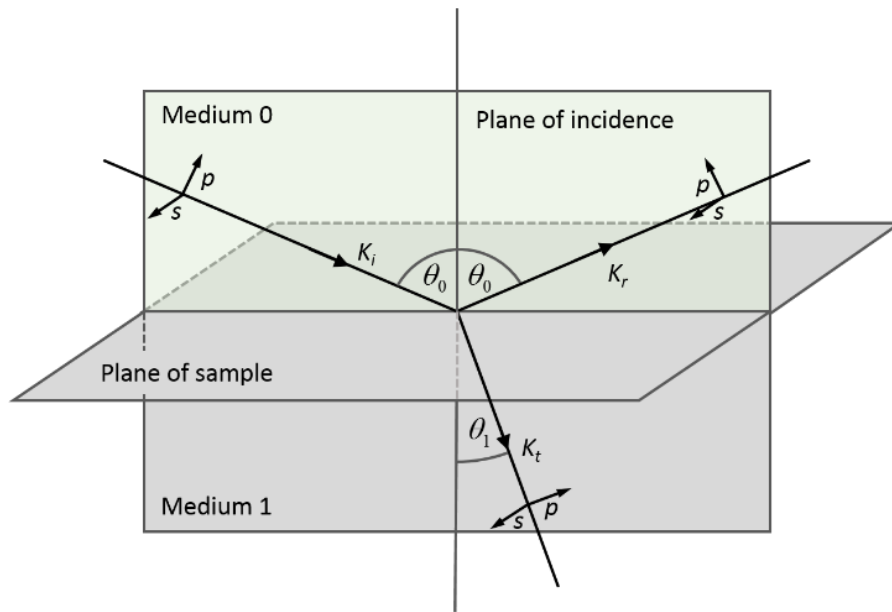


Figure 1.2: Schematic representation of a reflection and transmission of a p and s polarized light at a planar boundary interface. K_i , K_r and K_t represent the wavevectors of the incident, reflected and transmitted light, respectively.

In case the relative permeability is negligible, the complex valued refractive index can be expressed with the complex relative permittivity (or dielectric function, ε_r) as

$$\bar{N} = \varepsilon_r^{1/2}. \quad (1.12)$$

The dielectric function is of course related to the macroscopic Maxwell's equations in case of a linear, isotropic medium through the electric displacement field as

$$D = \varepsilon_0 \varepsilon_r E, \quad (1.13)$$

where ε_0 is the vacuum permittivity. Henceforward, the 'r' index will be omitted, and ε will always indicate the dimensionless complex relative permittivity.

1.2.2 Reflection from a thin layer

An optical model to characterize thin layers consists of a structure of three media separated by parallel planes. Let us consider the case of an ambient/film/substrate structure (cf. p. 283 in Ref. [5]). The incident light penetrates the thin film from the ambient and undergoes multiple reflections and refractions as depicted in Fig. 1.3. The resultant reflected and transmitted wave will thus be formed from the interference of an (ideally) infinite series of partial waves. For the case of a reflection measurement setup, the optical model considers the substrate to be semi-infinite, that is, the model does not consider backside reflections from the substrate. To obtain the total reflected amplitude E^{tot} for the ambient/film/substrate structure, one has to sum up the infinite geometric series of the partial waves, leading to the following equation:

$$E_{p,s}^{tot} = \frac{r_{01}^{p,s} + r_{12}^{p,s} \exp(-i2\beta)}{1 + r_{01}^{p,s} \exp(-i2\beta)} E_{p,s}^i, \quad (1.14)$$

where r_{01} and r_{12} are the Fresnel reflection coefficients at the 0|1 and 1|2 interfaces. β is the phase shift endured by the wave multiply reflected inside the thin film (otherwise known as the film phase thickness), and is given by

$$\beta = 2\pi \left(\frac{d}{\lambda} \right) \bar{N}_1 \cos \theta_1 \quad (1.15)$$

or

$$\beta = 2\pi \left(\frac{d}{\lambda} \right) \bar{N}_1 \sqrt{\bar{N}_1^2 - \bar{N}_0^2 \sin^2 \theta_0}, \quad (1.16)$$

if Snell's law is applied. In Eq. 1.15 and 1.16 λ is the free-space wavelength, d is the film thickness and \bar{N}_1 is the complex index of refraction of this film. Because the reflection coefficients at the interfaces will be different for the two linear polarization states, Eq. 1.14 will also be different for the two cases. This is the basis of an ellipsometric thin layer measurement. For example, by knowing the AOI, the initial polarization state, the wavelength of illumination

and the refractive indices of the three media, we can determine the layer thickness. With the

previously introduced notations, this will mean the inversion of $\rho = \frac{E_p^{tot}}{E_s^{tot}} \cdot \frac{1}{\chi_i}$ (cf. p. 315 in

Ref. [5]) \Rightarrow

$$d = \rho^{-1}(\bar{N}_0, \bar{N}_1, \bar{N}_2, \lambda, \theta_0, \chi_i). \quad (1.17)$$

Eq. 1.17 in general has more than one solution due to the square root and the cyclic complex exponential function $e^{-i2\beta}$ appearing in the explicit equation, so there should be an *a priori* knowledge of the range of film thickness to determine the correct physical value. It should be noted, that Eq. 1.14 is limited by the (sub-)layer thickness. For the infinite summation to be an accurate representation of our physical system, the lateral dimension of the film illuminated by the beam must be several times the thickness of the (sub-)layer.

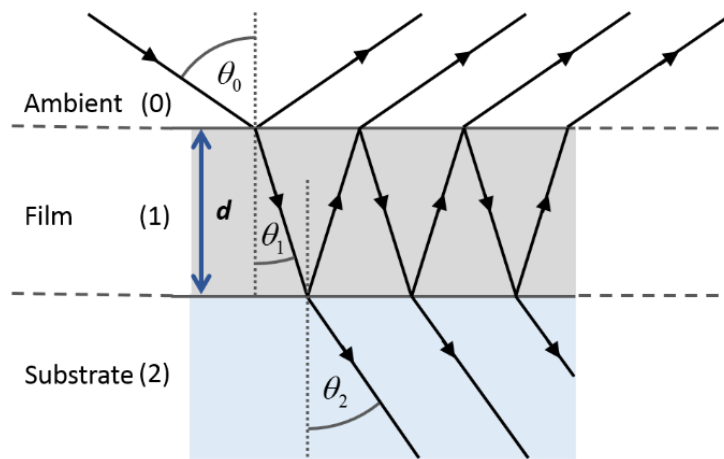


Figure 1.3: Schematic representation of a multiple reflection and transmission through a thin film with parallel planar interfaces. The relation between the angle of incidence and of refractions for this example depicts a case were the refractive index of the film is the highest.

1.2.3 Reflection from a multi-layer system

The procedure to formulate ρ for the thin layer structure can be generalized to stratified multi-layer systems as well by recursive steps. However, this formulation becomes quite cumbersome and impractical to implement in numerical calculations. A more elegant approach would be the transfer-matrix method (TMM), which employs 2×2 matrices to describe the

individual response at the interfaces and due to the propagation through the sublayers (cf. p. 332 in Ref. [5] and pp. 51 ff. in Ref. [7]).

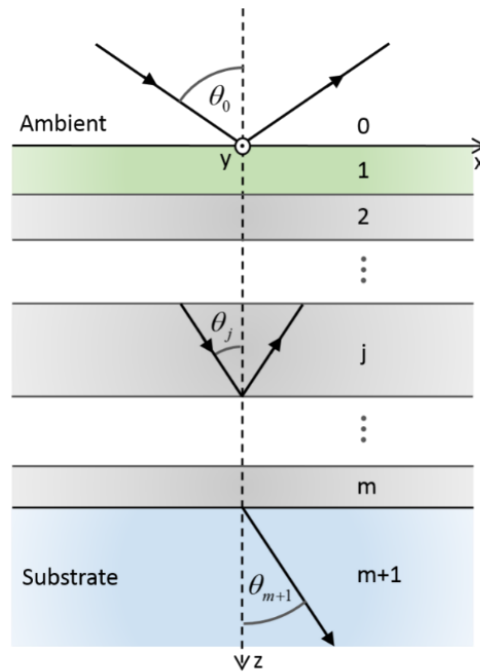


Figure 1.4: Schematic representation of a plane wave reflection and transmission through a stratified multilayered structure (m number of sublayers) sandwiched between a semi-infinite ambient (0) and substrate ($m+1$) media. θ_0 is the illumination angle of incidence, while θ_j and θ_{m+1} are the angles of refraction in the j^{th} film and substrate respectively.

Consider the stratified structure shown in Fig. 1.4: a stack of m number of plane-parallel layers sandwiched between an ambient and a substrate. The layers are indexed from 0 (ambient) to $m+1$ (substrate). Let all media be linear homogeneous and isotropic and let d_j indicate the thickness and \bar{N}_j the complex refractive index of the j^{th} layer with the z coordinate axis being perpendicular to the boundaries and pointing towards the substrate. The system is translation symmetric in the x and y coordinates. By virtue of the linearity of the equations that govern the propagation of light, we can in fact consider the total field at the plane z to be equal the sum of the fields of a forward and a backward traveling plane wave denoted by $E^+(z)$ and $E^-(z)$ linked to the component fields at a different z plane (z') by a linear transformation. If

we represent the total field by a 2-component vector, the above transformation translates to the following matrix representation:

$$\begin{bmatrix} E^+(z) \\ E^-(z) \end{bmatrix} = \begin{bmatrix} S_{11} & S_{12} \\ S_{21} & S_{22} \end{bmatrix} \begin{bmatrix} E^+(z') \\ E^-(z') \end{bmatrix}, \quad (1.18)$$

or more concisely to:

$$E(z) = \hat{S}E(z'). \quad (1.19)$$

If we take the plane z to lie in the ambient immediately above the $0|1$ interface and z' in the substrate immediately below the $m|m+1$ interface, then the so-called scattering matrix \hat{S} will define the overall reflection and transmission properties of the stratified system. \hat{S} can be in fact built up from the matrices describing the individual transitions through the interfaces (\hat{I}) and through the sublayers (\hat{L}) by ordered successive matrix multiplications, as follows:

$$\hat{S} = \hat{I}_{01} \hat{L}_1 \hat{I}_{12} \hat{L}_2 \cdots \hat{I}_{(j-1)j} \hat{L}_j \cdots \hat{L}_m \hat{I}_{m(m+1)}, \quad (1.20)$$

with

$$\hat{I}_{(j-1)j} = \frac{1}{t_{(j-1)j}} \begin{bmatrix} 1 & r_{(j-1)j} \\ r_{(j-1)j} & 1 \end{bmatrix} \quad (1.21)$$

and

$$\hat{L}_j = \begin{bmatrix} e^{i\beta_j} & 0 \\ 0 & e^{-i\beta_j} \end{bmatrix}, \quad (1.22)$$

where $r_{(j-1)j}$ and $t_{(j-1)j}$ are the Fresnel reflection and transmission coefficients between the interface separating the $(j-1)^{\text{th}}$ and j^{th} sublayer, while β_j is the phase thickness of the j^{th} sublayer. If we assume that there is no forward propagating plane wave in the substrate, then the total reflection coefficient of the stratified structure can be expressed by the \hat{S} matrix elements as

$$R = \frac{S_{21}}{S_{11}}. \quad (1.23)$$

To find the quantities measurable by an ellipsometer, we have to make the above calculation to both the p and s polarizations. Finally, we obtain ρ as the ratio of the total reflection coefficients of the two components:

$$\rho = \frac{R_p}{R_s}. \quad (1.24)$$

The simulations of ellipsometric spectra with readily available evaluation software are almost always performed by TMM, as it is able to describe a large range of systems.

1.3 Data analyses and fitting

The number of variables in Eq. 1.24 increases with the number of sublayers. The measurable ellipsometric response of a structure composed of m number of layers has the following parameter dependence:

$$\rho = \rho(\bar{N}_0, \bar{N}_1, \dots, \bar{N}_{m+1}, d_1, d_2, \dots, d_m, \Phi_0, \lambda). \quad (1.25)$$

As Eq. 1.25 has two measurable quantities (the previously introduces Ψ and Δ for example), two unknown parameters can be determined. The other parameters have to be either known a priori by other means (reference independent measurements of the optical constants, layer thicknesses), or the amount of independent information has to be increased. For the latter, examples are multi-sample analyses⁴, or measurements carried out at several AOIs, however, nowadays, the most widespread ellipsometric method would be the multi-wavelength approach (aka spectroscopic ellipsometry as introduced previously). Of course, for highly complex multi-layered structures a combination of several of the methods would be advisable (SE at multiple AOI). In the present work, detailed information about the actual method, i.e. the wavelength range and the AOIs used for the measurements, will be presented in the experimental sections for each chapter. Multi-sample analyses were not performed on the

⁴ Multi-sample analysis is a characterization technique where thin layers are fabricated with identical material quality but with different layer thickness. The parameters describing the material are coupled to each other during the fitting procedure while the thickness values are fitted independently.

different sets of nanostructures because their optical properties differed significantly from each other.

In general, the non-linear transcendental function standing on the right-hand side of Eq. 1.25 cannot be analytically inverted. We have seen the *reverse* problem for the special cases to determine the optical constants of one of the phases of a two-phase system and to determine the layer thickness of a three-phase system, for other problems, numerical inversions should be applied. Current ellipsometric instruments include evaluation software capable to compute the *forward* problem of complex systems by TMM almost in real time, however the *reverse* problem has to be solved by numerical fitting. For this purpose, we introduce a fitting error which represents the “goodness” of fit with a single value. It is defined as the root-mean-square error (or unbiased estimator):

$$RMSE = \sqrt{\frac{1}{J-P-1} \sum_{j=1}^J \left\{ \left(X_j^{meas} - X_j^{calc} \right)^2 \right\}} \quad (1.26)$$

where X^{meas} are the measured and X^{calc} are the calculated ellipsometric values, J is the number of independently measured values, and P is the number of unknown model parameters. Then, some kind of search algorithm is performed on the $RMSE$ hypersurface and generally we accept the parameters belonging to the case of minimum $RMSE$. Typically, in the software used for fitting, the Levenberg-Marquardt regression analysis method is included (cf. pp. 196 ff. in Ref. [3] and Ref. [8]). When we develop and compare several optical models with different P (and/or J), other considerations should be also made, like the errors (standard 90% confidence limits) or cross-correlations (CCs) of the fitted parameters. These are calculated from the diagonal and off-diagonal elements of the covariance matrix of the fit parameters, respectively [9]. The specific form of the $RMSE$ will depend on the type of ellipsometer used in the measurements and will be defined in the relevant chapters.

1.4 Ellipsometric setup and sensitivity

Spectroscopic ellipsometers usually consist of a polarizer and an analyzer arm, a sample holder, a goniometer, a detection system, and an appropriate control equipment (Fig. 1.5). To achieve spectroscopy, different methods can be used depending on the spectral range. For measurements in the ultraviolet-near-infrared (UV-NIR) range, dispersive spectrometers are used either with a step-by-step motor directing a monochromatic wave on a photomultiplier or with a multichannel detection system (photodiode or CCD array). For measurements in the mid-infrared range (MIR) however, Fourier-transform infrared spectroscopy (FTIR) is generally used because the infrared radiation sources are weak. In brief, a FTIR setup consists of a Michelson interferometer, where the intensity spectra are obtained by Fourier transformation of the interferograms.

To obtain the ellipsometric information (polarization variations upon reflection), the light is modulated somewhere between the optical path. Typically rotating polarizer or compensator elements are used. In a UV-NIR setup, the detected intensity signal will have a harmonic form because one of the optical elements is continuously rotating. On this intensity signal Fourier analyses is performed to calculate the ellipsometric angles. In Fig. 1.5, a rotating compensator spectroscopic ellipsometer is shown that I used for some of my characterizations. In a FTIR setup, several interferograms are collected at different fixed azimuthal angles for one of the polarizer elements from which the ellipsometric angles can be calculated.

For my thesis work, I used several different ellipsometers, whose main attributes will be detailed in the appropriate chapters (one of these ellipsometers is shown in Fig. 1.5). Before every measurement set, I first performed an AOI offset calibration with a reference oxide sample. This is especially important when measurement is made through microfocusing lenses, as differences between real and nominal AOI can appear that must be accounted for in the evaluations.

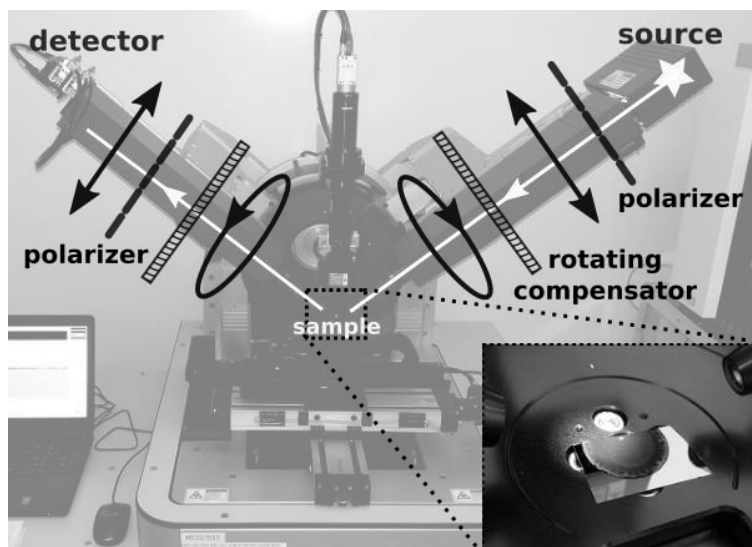


Figure 1.5: Schematic diagram of the principal optical elements of a rotating compensator ellipsometer projected on an image of a Semilab SE-2000.

To illustrate the sensitivity of a typical contemporary spectroscopic ellipsometer, avoiding entering into mathematical details, in Fig. 1.6 a few characteristic Ψ and Δ simulations are shown. TABLE 1.1 lists the *RMSE* values that represent here the root-mean-square deviations between the simulated spectral points from a bulk Si and three different layer structures respectively. Roughness has been simulated as 50–50% void/Si ratio with effective medium approximation detailed in section 1.6. We can see that even an ultrathin layer produces a distinguishable difference in the spectra compared to a bulk Si. Two angles of incidence simulations are shown to demonstrate the increased sensitivity when the Brewster angle of the Si substrate is at a wavelength within the spectral range (75° for $\lambda = 738.5$ nm). Furthermore, it can be seen that differences are higher in Δ spectra, indicating that phase variations carry more information, as typical noise rates are around 0.1° for both Ψ and Δ .

TABLE 1.1: *RMSE* values of simulated Ψ and Δ angles between bulk Si and three different thin layer structures.

	<i>RMSE</i> at 75°	<i>RMSE</i> at 70°
SiO₂ 0.5 nm	7.492	0.749
SiO₂ 1 nm	11.727	1.495
Roughness 1 nm	3.149	0.223

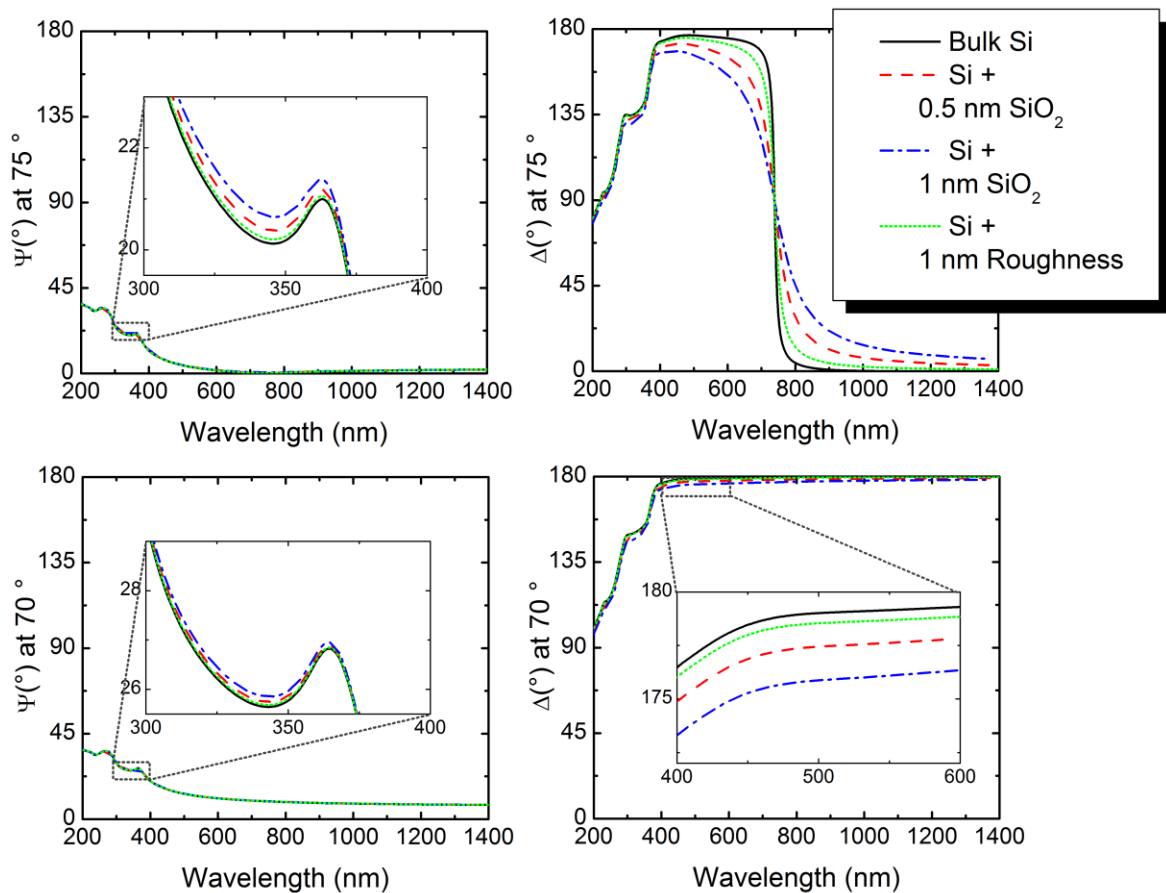


Figure 1.6: Simulated SE spectra of slightly different surface structures at an AOI of 75° (top left and right) and at an AOI of 70° (bottom left and right) to demonstrate surface characterization sensibility. Sensitivity is much higher at 75° because it is the Brewster angle of Si at $\lambda = 738.9$ nm.

1.5 Models for the optical properties of materials

We have seen (Eq. 1.25) that in order to model the ellipsometric response, the dielectric functions of the layers have to be known. When we have no reference measurements, the dielectric functions have to be described parametrically (cf. pp. 158–176 in Ref. [3]). One such parametrization consists of the Lorentz oscillator model, which will be briefly presented below with one of its extensions.

The model can be phenomenologically understood from the classical dynamics of an excited damped harmonic oscillator. The polarization behavior of a localized electron submitted to an external AC electric field can be analogized by a linearly oscillating spring. With this simple model and from the definition of electric polarization and its relation to the dielectric function, the latter can be expressed as

$$\varepsilon(\omega) = 1 + \frac{A}{(\omega_0^2 - \omega^2) + i \cdot \Gamma \omega}, \quad (1.27)$$

where ω_0 is the natural frequency, A is the amplitude and Γ is the damping coefficient of the oscillation responsible for the broadening of the critical points. These three parameters are usually fitted in an ellipsometric evaluation scenario. A remarkable property of Eq. 1.27 is that it is intrinsically Kramers-Kronig consistent, that is, there is a one-on-one correspondence between the real and imaginary part of the dielectric function (and thus between n and k) as a consequence of causality.

The shape of the peaks of the imaginary part of the dielectric function (ε_2) calculated from the Lorentz model is completely symmetric and thus not able to well describe most amorphous materials as they show generally asymmetric shapes. Jellison et al. [10–12] have developed a better model suitable for fitting amorphous materials. They incorporated the Tauc absorption law [13] to describe the near bandgap behavior to that of the Lorentz oscillator for the determination of ε_2 . They named it the Tauc-Lorentz oscillator model. To obtain the real part of the dielectric function (ε_1), they used Kramers-Kronig integration with an additional

$\varepsilon_{\text{inf}} = \varepsilon(\omega \rightarrow \infty)$ parameter accounting for contributions out of the sampling frequency range⁵. Usually in evaluations ε_{inf} can be set to = 1 and fitting is performed with 4 independent parameters, that is, 3 describing the excitation peak and an additional bandgap energy parameter (E_g).

1.6 Effective medium theory

There exists another ensemble of methods to describe the optical properties of an investigated material. The main concept is to formulate the macroscopic optical properties of a composite medium by the optical properties of its microscopic constituting parts. In fact, within the ellipsometric community, these so called effective medium theories (EMTs) are the most widely accepted methods to obtain structural information about thin films. In the past decades, great number of EMTs have appeared, all with different theoretical background and so having different pros and cons when describing nanostructured materials. All of them have two delimitations concerning the typical feature sizes of the constituent components. First, the connected volume (aggregates) have to be large enough to keep their bulk like optical behavior⁶. Secondly, they have to be small enough compared to the wavelength of illumination so that scattering effects can be neglected. In the following subsections, I will present three EMTs; the first, the simplest one, because it is easily understood from atomistic first principals and the second two because they are the most widely used in general and in my thesis work as well.

1.6.1 Lorentz-Lorenz equation

From the prototypical inhomogeneous material of simple cubic lattice points, we can deduce a relation between the dielectric function of the material and the polarizability of the

⁵ The equations for ε_1 and ε_2 are lengthy and thus omitted; cf. Eq. 4 in Ref. [9] for ε_2 and the erratum [10] for ε_1 .

⁶ This limitation is not always mandatory, because even the optical properties of the constituent parts can be described parametrically, correlating to shape and size effects.

individual atoms, considered as independent dipoles, and their atomic density. First, the microscopic problem is solved exactly, then the macroscopic counterparts are obtained by volume averaging of these microscopic solutions [14,15]. We can in fact eliminate all fields from the obtained equations and deduce the Clausius-Mosotti relation:

$$\frac{\varepsilon - 1}{\varepsilon + 2} = \frac{4\pi}{3} \rho_v \cdot \alpha^*, \quad (1.28)$$

where ρ_v is the volumetric point density and α^* the polarizability of an atom. If we consider a heterogeneous medium composed of two randomly mixed phases with polarizabilities α_a^* and α_b^* , we obtain the following formula for the dielectric function of the composite:

$$\frac{\varepsilon - 1}{\varepsilon + 2} = \frac{4\pi}{3} (\rho_{v,a} \cdot \alpha_a^* + \rho_{v,b} \cdot \alpha_b^*). \quad (1.29)$$

In fact, this equation involves microstructural parameters that are not measured directly, but if the dielectric functions of the pure individual phases are known (ε_a and ε_b), then we can rewrite Eq. 1.29 as

$$\frac{\varepsilon_{\text{eff}} - 1}{\varepsilon_{\text{eff}} + 2} = f_a \frac{\varepsilon_a - 1}{\varepsilon_a + 2} + f_b \frac{\varepsilon_b - 1}{\varepsilon_b + 2}. \quad (1.30)$$

This is the Lorentz-Lorenz effective medium expression, where $f_a = \rho_{v,a} / (\rho_{v,a} + \rho_{v,b})$ and $f_b = \rho_{v,b} / (\rho_{v,a} + \rho_{v,b})$ are the volume fractions of the two phases. We added the “*eff*” subscript, indicating that the macroscopic dielectric function is an effective value of those of the individual phases.

1.6.2 Maxwell-Garnett approximation

If the characteristic volume of the two phases are large enough to possess their own dielectric identity, then an intuitive step would be to consider Eq. 1.30 with the assumption of not vacuum, but a host medium (with ε_h as host dielectric function) in which the phases are embedded. Eq. 1.30 can be then written as

$$\frac{\varepsilon_{eff} - \varepsilon_h}{\varepsilon_{eff} + 2\varepsilon_h} = f_a \frac{\varepsilon_a - \varepsilon_h}{\varepsilon_a + 2\varepsilon_h} + f_b \frac{\varepsilon_b - \varepsilon_h}{\varepsilon_b + 2\varepsilon_h}. \quad (1.31)$$

Often, the approximation of a $\varepsilon_h = \varepsilon_a$ (or $\varepsilon_h = \varepsilon_b$) is made indicating that one of the phases is well diluted, and the other can be considered as the host. In this case, from Eq. 1.31 we obtain the Maxwell-Garnett effective medium approximation (MG-EMA):

$$\frac{\varepsilon_{eff} - \varepsilon_h}{\varepsilon_{eff} + 2\varepsilon_h} = f_b \frac{\varepsilon_b - \varepsilon_h}{\varepsilon_b + 2\varepsilon_h}. \quad (1.32)$$

Eq. 1.31 and 1.32 describe spherical inclusion, but it can be generalized to describe a medium with ellipsoidal inclusions as well [16]. If the ellipsoids are all aligned in the same axial direction, ε_{eff} is stated by the following mixing rule:

$$\varepsilon_{eff} = \varepsilon_h \left(1 + \frac{f \cdot \mathbf{B}}{1 - f \cdot \mathbf{B} \cdot \mathbf{L}} \right), \quad (1.33a)$$

with

$$\mathbf{B} = \frac{\varepsilon_a - \varepsilon_h}{\varepsilon_h + L \cdot (\varepsilon_a - \varepsilon_h)}, \quad (1.33b)$$

where the additional L parameter is an orientation dependent shape parameter, called the depolarization factor. It describes electric field screening in the three perpendicular directions x , y or z with $L_x + L_y + L_z = 1$. This generalized MG-EMA is good to describe anisotropic media (cf. pp. 209 ff. in Ref. [3]), it will serve a useful purpose in Ch. 4.

1.6.3 Bruggeman effective medium approximation

Eq. 1.32 (and 1.33) is appropriate when one of the constituents is much smaller than the other, with the latter being the host material. In cases where f_a and f_b are comparable however, we can make the self-consistent choice of $\varepsilon_h = \varepsilon_{eff}$. This leads to the Bruggeman effective medium approximation (B-EMA) with the following mixing formula:

$$f \frac{\varepsilon_A - \varepsilon_{eff}}{\varepsilon_A + 2\varepsilon_{eff}} + (1 - f) \frac{\varepsilon_B - \varepsilon_{eff}}{\varepsilon_B + 2\varepsilon_{eff}} = 0, \quad (1.34)$$

with $f_a = f$ and $f_b = 1 - f$.

It is also called symmetric effective medium approximation because the two constituents can be interchanged in the equation. Eq. 1.34 can be easily extended to incorporate more than two components, however, to model anisotropic layers, similarly to that of the MG-EMA, a more generalized formula with a depolarization factor should be used [17,18]:

$$f \frac{\varepsilon_A - \varepsilon_{eff}}{\varepsilon_{eff} + L \cdot (\varepsilon_A - \varepsilon_{eff})} + (1 - f) \frac{\varepsilon_B - \varepsilon_{eff}}{\varepsilon_{eff} + L \cdot (\varepsilon_B - \varepsilon_{eff})} = 0. \quad (1.35)$$

1.6.4 Birefringence, dichroism and ellipsoid shape

For both anisotropic models (MG-EMA, B-EMA), in case $L=1/3$ for all directions, Eq. 1.33 and Eq. 1.35 reduce to their isotropic cases, respectively. When modeling an effective medium layer (EML) of uniaxial anisotropy with MG-EMA or B-EMA, other than the layer thickness, fitting is performed on the void volumetric ratio (f) and on one of the depolarization factors, e.g. L_z , while fixing the other ones to be $L_x = L_y = (1 - L_z)/2$. Additionally, for an arbitrarily oriented optic axis, the Euler angles are also fitted in relation to the sample normal – plane of incidence coordinate system. We obtain in fact a distinct ε_{eff} in the z direction (ε_{eff}^z) and in the xy plane (ε_{eff}^{xy}). Optical birefringence will be then:

$$\Delta n = n_e - n_o = \text{Re}[(\varepsilon_{eff}^z)^{1/2}] - \text{Re}[(\varepsilon_{eff}^{xy})^{1/2}], \quad (1.36)$$

where n_e is the refractive index in the extraordinary direction (z in our case) and n_o is the refractive index in the ordinary direction (in the xy plane in our case). Similarly to Δn , we introduce the difference of the extinction coefficients of the two directions to describe dichroism:

$$\Delta k = k_e - k_o = \text{Im}[(\varepsilon_{eff}^z)^{1/2}] - \text{Im}[(\varepsilon_{eff}^{xy})^{1/2}]. \quad (1.37)$$

Furthermore, we can relate the L values to the shape of the ellipsoid [19–21]. For a uniaxial anisotropy,

$$L_z = \frac{a^2 c}{2} \int_0^\infty \frac{(s+c^2)^{-3/2}}{(s+a^2)} ds, \quad (1.38)$$

where a and c are the semi-minor and semi-major axes, respectively, of a prolate spheroid. $L_z = 0$ would describe an effective medium layer (EML) with needle-like inclusions parallel to z , while $L_z = 1$ would describe laminar inclusion perpendicular to z .

1.6.5 Limitations of effective medium theories

As mentioned at the beginning of the section, EMTs work well when the individual phases have large enough continuous extent to retain their bulk like dielectric behavior, and quantum confinement or other micro-surface related effects are negligible. In this case, the dielectric functions of the constituent parts can be taken from reference (literature) measurements, and only the volume ratios and depolarization factors are fitted. Otherwise, some parametric formulation like that of section 1.5 can be used to describe the optical properties of the individual components, but then often high cross-correlations appear between the volume fractions and the other parameters, and even the meaning of individual volume fractions becomes questionable.

The other limitation for EMTs arises, when the typical (lateral) feature sizes become too large compared to the wavelength of illumination (λ) and is related to scattering effects. These scatterings occur for instance in cases of very rough surfaces or interfaces, for periodic structuring or for pore or crystalline size comparable to λ . Multipole expansion calculations have shown, that isotropic B-EMA works well when the constituent parts have a typical size much smaller than the wavelength of the probing light [14,22] and size dependent quadratic corrections appear as the lowest-order corrections [23].

2 Buried cavities in ion-implanted and annealed silicon

High-fluence⁷ helium implantation followed by thermal annealing leads to extended defect formations, such as dislocations and buried cavities in single-crystal silicon (c-Si) [24]. Above a critical fluence, He forms nanosized bubbles that evolve into cavities due to the exodiffusion during thermal treatment. Cavities in these materials can be used for different applications, such as Smart-Cut™ process [25], gettering of metal impurities during device processing [26,27], diffusion control of dopants for ultrashallow junctions [27,28]. Transmission electron microscopy (TEM) is an established tool to investigate these structures, but unfortunately it is very time consuming and difficult to determine at a same time a depth distribution profile of the cavities and to observe defects of a few nm to thousands of nm that are encountered in the same area. These structures can be studied by SE and, with appropriate multilayered models, the in-depth profiles of the implantation-caused damaged Si [29–33,T4] and the cavity formation after thermal annealing [31,34–36,T4] can be evaluated. SE has the advantage over TEM that it is fast, non-destructive and so can be implemented even as a feedback control for industrial processes [31,37], in our case as potential *in situ* control for defect engineering.

In this chapter, we will discuss the ellipsometric evaluation of a large number of Si wafers subjected to different high energy implantations through sacrificial oxide layers and thermally treated with different annealing conditions. The formation of buried cavities in Si is investigated as a function of the implantation fluence, the annealing temperature and the thickness of the sacrificial oxide layer.

⁷ In this chapter, implantation fluence is used as the parameter defining the number of particles passing through a unit area (in cm⁻²), often referred to as implantation dose in other sources.

2.1 Experimental details

2.1.1 Sample preparation details

The sample preparations, the implantations and the annealings, as well as the TEM observations were made at GREMAN institute. Single crystalline p-type Czochralski (111) silicon substrates (resistivity of 0.026–0.034 $\Omega \times \text{cm}$), covered with a sacrificial oxide layer (130, 150 and 170 nm), were implanted at 7° tilt with high helium fluences ($2\text{--}6 \times 10^{16} \text{ cm}^{-2}$) at an energy of 20 keV. The oxide layers partially mask the penetration of the ions, and thus control their in-depth stopping-range. The SiO_2 layers were removed by chemical etching in a 10% hydrofluoric acid solution after implantation. Then, the samples were thermally annealed with conventional furnace annealing under N_2 atmosphere at 650, 800 and 1000 °C for 1 hour. TABLE 2.1 summarizes these implantation and annealing conditions totaling in 39 investigated sample (3 non-implanted, 3×3 as-implanted and 3×3×3 implanted and annealed).

TABLE 2.1: Implantation and annealing conditions for the investigated samples

SiO_2 thickness	Implantation energy	Implantation fluence	Annealing temperature	Annealing time	Number of samples
130 nm	20 keV	non-implanted	as-implanted	60 min	39
150 nm		$2 \times 10^{16} \text{ cm}^{-2}$	650 °C	conventional furnace	
170 nm		$4 \times 10^{16} \text{ cm}^{-2}$	800 °C		
		$6 \times 10^{16} \text{ cm}^{-2}$	1000 °C		

1.1.1 Measurement details

The SE measurements were performed on the non-implanted, the as-implanted and the annealed Si samples using the MFA⁸ Woollam M-2000DI variable angle spectroscopic ellipsometer. It utilizes the rotating compensator technology with two multichannel detection

⁸ In 2014, MFA was part of the Research Centre for Natural Sciences (MTA TTK MFA)

systems. This setup enables fast (~ 1 s) measurements of both ellipsometric angles in the wavelength range from 191 to 1690 nm (6.49–0.73 eV), with a spectral resolution of about 1.5 nm in the lower (short wavelength) part and about 3.5 nm in the upper part of the spectrum, totaling in 706 wavelength points. The angles of incidence of the illumination were chosen to be between 70° and 78° with a separation of 2° , in order to be close to the Brewster angle of Si for (most of) the wavelengths within the spectral range. The non-focused spot size has a diameter of around 2 mm, and so a projected major axis between 5.8 and 9.6 mm (for angles of 70° and 78° , respectively). Model development was performed with Woollam's WVASE v3.386 and CompleteEASE v4.72⁹ data acquisition and analysis software packages, but final fitting for evaluation and comparison purposes was only done with the latter. For the rotating compensator setup, the *RMSE* for fitting is best defined with the *N*, *C* and *S* ellipsometric parameters (cf. Eq. 1.26) as they are linearly related to the measured intensity harmonics modulated by a rotating compensator [3]:

$$RMSE = \sqrt{\frac{1}{J-P-1} \sum_{j=1}^J \left\{ \left(N_j^{meas} - N_j^{calc} \right)^2 + \left(C_j^{meas} - C_j^{calc} \right)^2 + \left(S_j^{meas} - S_j^{calc} \right)^2 \right\}}, \quad (2.1)$$

but for illustration purposes Ψ and Δ remain more convenient. In fact, as stated from the Woollam specification, both *N*, *C* and *S* have approximately the same precision and accuracy on any sample (~ 0.001) [38]. For a non-depolarizing sample, the squared sum of *N*, *C* and *S* values should be equal to one. A value < 1 would indicate some kind of polarization non-uniformity (scattering from high surface roughness, thickness inhomogeneity, illumination conical divergence, etc...).

The crystalline structures of the implanted samples were characterized at GREMAN using TEM and scanning TEM to investigate the material amorphization and the distribution of cavities within the different samples after annealing. 5 TEM lamellae were prepared and observed with an "FEI Strata 400" dual-beam system (scanning electron microscopy and

⁹ More recent version is available; <https://www.jawoollam.com/ellipsometry-software/completeease>.

focused ion beam) equipped with a flip stage for lamella transfer on TEM grid and with a scanning TEM detector for observations. A JEOL 2100F was used in classical observation modes for TEM observations.

2.2 Modelling and evaluation strategies

2.2.1 Ellipsometric modelling

To illustrate the sensitivity of ellipsometric response to the different samples, we show in Fig. 2.1a and b the Ψ and Δ spectra, respectively, of an as-implanted Si at $4 \times 10^{16} \text{ cm}^{-2}$ fluence (through 130 nm sacrificial layer) and its corresponding 800 °C annealed phase. The spectra calculated from the reflection from a bulk c-Si is also shown for reference. All the spectra are taken at 76° , which would correspond to the Brewster angle of Si at a wavelength of 570 nm. As the spectra reveal, SE is very sensitive to the different states, especially near the Brewster angle where Δ sweeps across a large portion of the whole phase band.

The ellipsometric models describing the as-implanted and the annealed samples followed a similar pattern. A surface native oxide layer, a (partially) damaged layer and a semi-infinite substrate layer were stacked for the as-implanted samples while an oxide (thermally grown), a cavity, and a substrate layer were used for the annealed samples. To account for the optical response of the intermediate layer (partially amorphous, or defected layer) a model consisting of several independent effective medium sublayers with varying fraction of component content was used: A mixture of c-Si and amorphous Si (a-Si) for the damaged region of the as-implanted Si samples and a mixture of c-Si and void for the cavity region of the annealed Si samples, as it was previously demonstrated to be a very good choice of model (cf. Model 4 in Ref. [35] and Model 10 in Ref. [36]). Both the Maxwell-Garnett (MG-EMA, cf. Eq. 1.32) and Bruggeman effective medium approximations (B-EMA, cf. Eq. 1.34) were tested but for the sublayers of a given cavity depth profile only one type was used for simplicity and inter-comparability. The B-EMA based models almost always resulted in a better fit, probably because the void

percentages span across large values and the MG-EMA is generally only applicable for small percentages of inclusions, consequently, only the former is presented in this chapter. Scattering effects were also negligible because the typical size of the cavities is much less than the wavelength of the probing light. The low depolarization values (less than 4% at the whole spectral region) also evidenced that there is no scattering effect, confirming the validity of effective medium theory (EMT) based models.

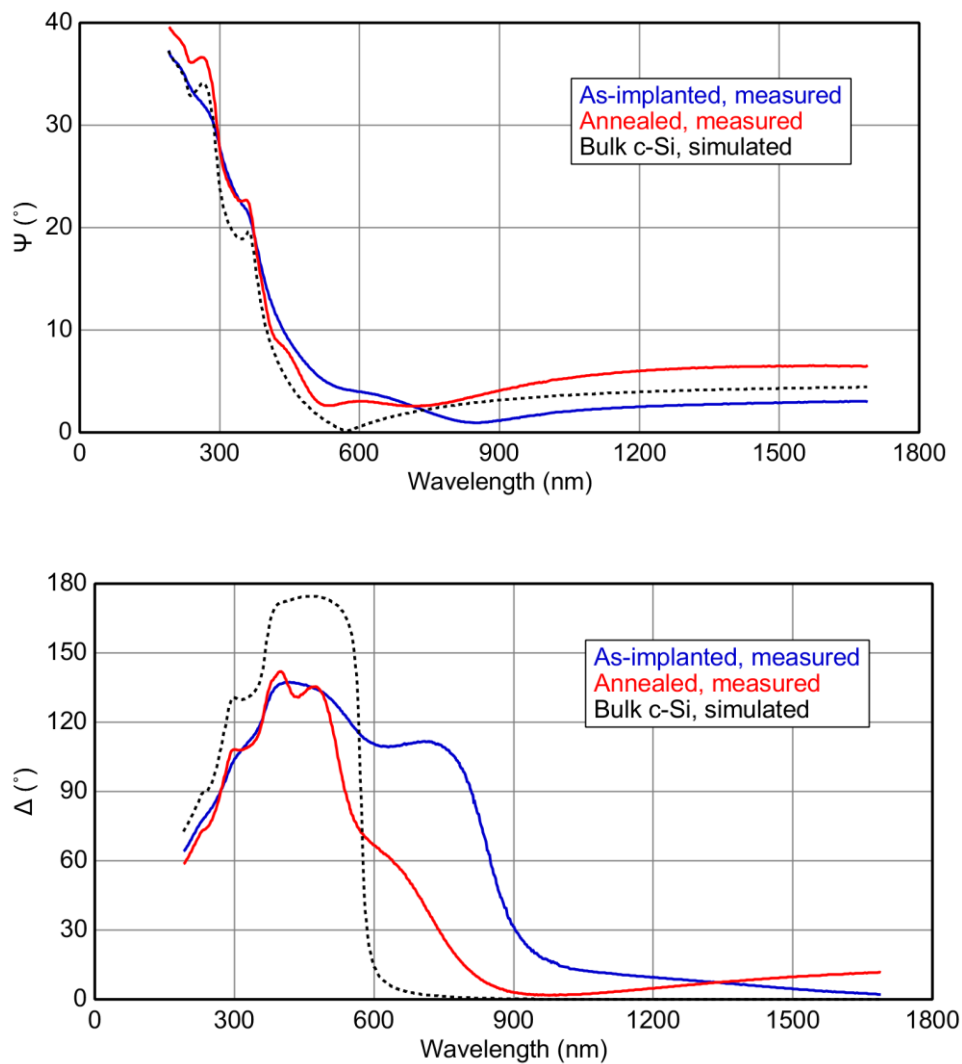


Figure 2.1: Measured and simulated ellipsometric angles to illustrate the ellipsometric sensitivity for different silicon states involved in the study. The spectra are shown for the angle of incidence of 76° , corresponding to a Brewster angle at 570 nm.

The complex dielectric functions of c-Si and SiO₂ were taken from the reference measurements of Herzinger, who did a thorough multi-sample, multi-AOI, spectroscopic ellipsometric investigation of these two materials and compared them to previous results [39]. These optical constants are included as-is in both evaluation software packages. On the other hand, the dielectric dispersion function of the a-Si component was described with a Tauc-Lorentz oscillator model of 4 fit parameters [12] (cf. Ch. 1.5) because optical properties of reference a-Si depend on the amorphization conditions. For example, they largely differ between a-Si prepared by evaporation and a-Si obtained by implantation [40]. Furthermore, they can even vary as a function of the implantation conditions as indicated by the fact that if an implanted a-Si reference is used to determine the damaged depth profile of a different implantation, a three-component B-EMA with an additional void content is better applicable [35]. We choose to fit all 4 parameters of the Tauc-Lorentz dispersion function describing ϵ_2 , and obtaining ϵ_1 with the Kramers-Kronig relations as explained in Ch. 1.5, with an ϵ_{inf} set to 1.¹⁰

The stacked layers can describe a vertically inhomogeneous dielectric function and, due to the B-EMA volume fraction fit parameters, the in-depth distribution of the substituent content can be obtained (defect or void distribution). The depth distribution of the amorphization can be described by several different semi-empirical graded models [32,40], such as two coupled half-Gaussians [30,40], two coupled error functions [34], with adaptive depth resolution depending on the slope of the profile [29]. Similar parametrizations can be used to describe the depth profile of the cavities, but often there are more than one peaks appearing in the SE and TEM void depth profiles [35,36]. For this reason, and also to demonstrate the depth resolution capabilities of SE, we choose a graded model with substituent volume fractions fitted independently for both the as-implanted and the annealed samples. Additionally, the thickness values of the sublayers were coupled to each other, and the thickness of the whole amorphous or cavity layer was fitted except for the top effective

¹⁰ Calculations are automated by the evaluation software.

medium layer (EML) of the annealed and for the top two EMLs of the as-implanted samples whose thickness values were fitted independently. This way a more detailed account can be made of the near surface region to which the probing light is more sensitive.

The number of EMLs (m) has been chosen in a way to maximize the fit quality while avoiding large fit errors (>5%) and unphysical fit parameters. A large cross-correlation (CC) between two parameters (>98%) is also an indication, that our model is over parameterized, and so we cannot give credit to these fitted values as being representative of the sample. Sensitivity analysis was also performed on some of the fitted critical parameters and onto those with high errors. Generally, when an error of a parameter is high, the *RMSE* is more flat at the minimum meaning that we are less sensitive to the parameter in question. An example of how m effects the fit quality, the maximum relative errors and the CC-s of the evaluation of the sample with a 130-nm sacrificial oxide, implanted with $4 \times 10^{16} \text{ cm}^{-2}$ and annealed at 800 °C is represented in TABLE 2.2. As it can be seen, when increasing the number of sublayers, the *RMSE* decreases. Between $m = 2$ and 6, *RMSE* decreases drastically, then it is less impacted by m . At $m = 8$ a large CC appears but the largest error is still acceptable, at $m = 10$, CC and errors are too large.

TABLE 2.2: *RMSE*, largest relative fit errors and largest absolute value of CC as a function of m

m	2	3	4	5	6	7	8	9	10
<i>RMSE</i>	15.38	10.5	5.44	2.763	1.981	1.895	1.802	1.794	1.737
~max. rel. err.	<1%	<1%	<1%	<1%	<1%	5%	5%	30%	100%
max. CC 	54%	48%	44%	56%	73.7%	89.5%	99.2%	99.9%	99.5%

2.2.2 Transmission electron microscopic analyses

The cavities from the TEM micrographs were analyzed in the following way: the cross-sectional images of each cavity layer were sliced into several parts (3 or 6). The surface area of

the projection of the cavities were added up, then divided by the total surface area of the sublayer. This way, a depth distribution of the cavities has been obtained (depth distribution of 2D cavity projection). Several cavities were cut into half on the image by two bordering sublayers. In this case, only the fraction of its surface belonging to the sublayer in question was counted into the sum (see schematic representation of Fig. 2.2). For each prepared TEM lamella, this has been done on three different micrographs to obtain average results. It is important to note, that the direct conversion from cavity profiles of 2D projected area to 3D volumetric cavity profiles is not straightforward. In the simple case when the distribution of cavities remains homogeneous in depth, and the cavities are sphere-like, then with the following simple formula one can calculate the volume ratio: $V = A / \left(\frac{3d}{4R} + 1 \right)$, here A stands for the area ratio, d for the cross-sectional thickness of the sample used in the analyses and R for the average radius of the spheres. One of the problems is, that it is very difficult to know or determine exactly the value of d . Also, the cross section of the sample can be wedge-shaped, meaning that d can be different from sublayer to sublayer, further complicating the conversion. And lastly, the cavities are clearly not distributed homogeneously as we will see from the evaluations. Because of these complications, cavity profiles are only compared between the original projected area of the TEM analysis's and the volumetric SE evaluations. These remarks reinforce the interest of ellipsometry for such type of analysis.

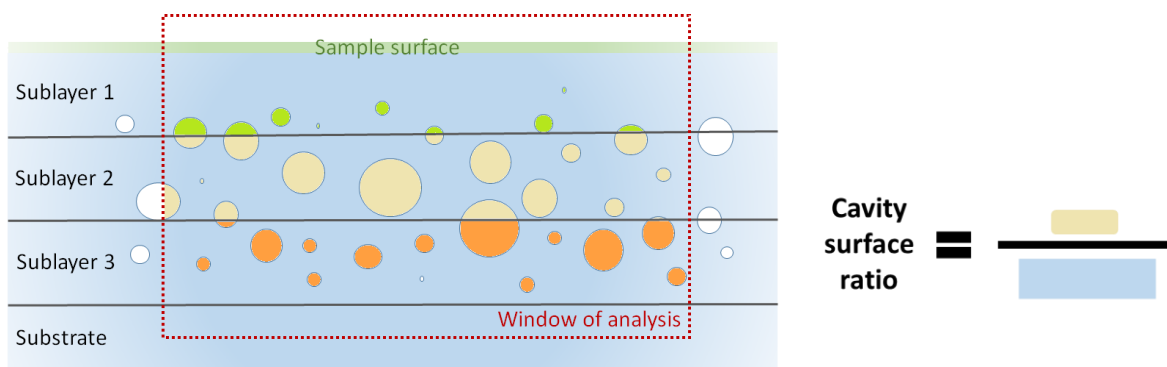


Figure 2.2: Schematic representation of the method used to determine the projected 2D area density of the cavities.

2.3 Evaluation of as-implanted samples

Ion-implantation distributions were simulated with J. Ziegler's "The Stopping and Range of Ions in Matter" freeware downloadable program [41]. Fig. 2.3a shows such a simulation, demonstrating He and vacancy distributions in Si after passing through a SiO₂ layer.

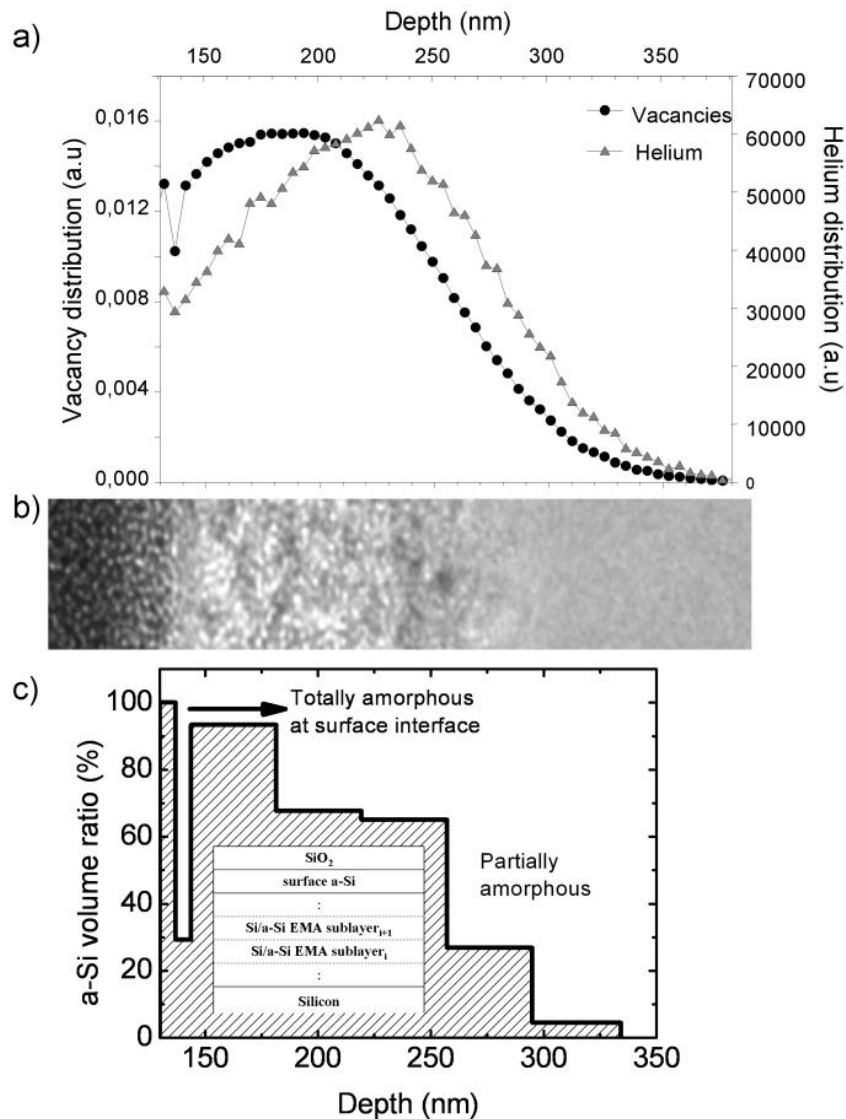


Figure 2.3: He and vacancy depth distribution from a simulation of 20 keV, $4 \times 10^{16} \text{ cm}^{-2}$ implantation through a 130 nm sacrificial oxide layer (a), corresponding cross-sectional TEM image (b) and amorphous volume fraction depth distribution from SE evaluation with ellipsometric model inset (c). Depth scale of SE plot has been shifted to match that of SRIM simulation (i.e. by the 130 nm thickness of the sacrificial oxide layer).

Beneath it, Fig. 2.3b displays a TEM image while 2.3c shows the SE evaluation results of the multilayered B-EMA model of the corresponding as-implanted sample. It can be seen that the damage profile is very similar to the vacancy distribution but the damage profile has its peak closer to the surface, with a 94% amorphous content decreasing in depth. At the top interface, there is a clear 7 nm thick layer that is totally amorphous. This anomalous surface amorphization effect has also been reported by previous SE studies [32,34,42,43] caused by the SiO₂/c-Si interface acting as a sink for point defects [44].

2.4 Evaluation results of buried cavities

2.4.1 Depth resolution from transmission electron microscopy and ellipsometry

As we increase the number of sublayers in the ellipsometric models, we could obtain better depth resolution. For the TEM analysis, the maximum sublayer number depends on the size of the cavities (max 6), while for the SE evaluations it depends on the errors of the fitted parameters. In Fig. 2.4 we can see the effect of increasing m . The left set (a, c and e) corresponds to the 800 °C annealing, while the right set (b, d and f) to the 1000 °C annealing of the samples covered by a 130 nm sacrificial oxide implanted at a fluence of $4 \times 10^{16} \text{ cm}^{-2}$. Figs. 2.4a and b show small portions of TEM images displaying cavity morphology, in Figs. 2.4c and d the cavity surface depth distributions analyzed on larger scales are shown. Figs. 2.4e and f (bottom three graphs) are the void depth distribution of SE evaluation fitted with $m = 3, 6,$ and $9,$ respectively, showing an increasing depth resolution, with the error bars of the fitting (90% confidence intervals) only appearing for the last case. Clearly, SE results are very similar to those made by TEM analyses, thus cross-validating each other, and showing that SE is applicable for cavity depth profile evaluations. Furthermore, the cavity layer thicknesses show a very good agreement between the two methods (within 10 nm), but the SE evaluations show a slightly larger thickness when using larger m . This is explained by the fact, that SE remains sensitive to

the smaller void fractions at the bottom interface not accounted for by the TEM analyses even though that the error bars show the least sensitivity for the last bottom B-EMA sublayer.

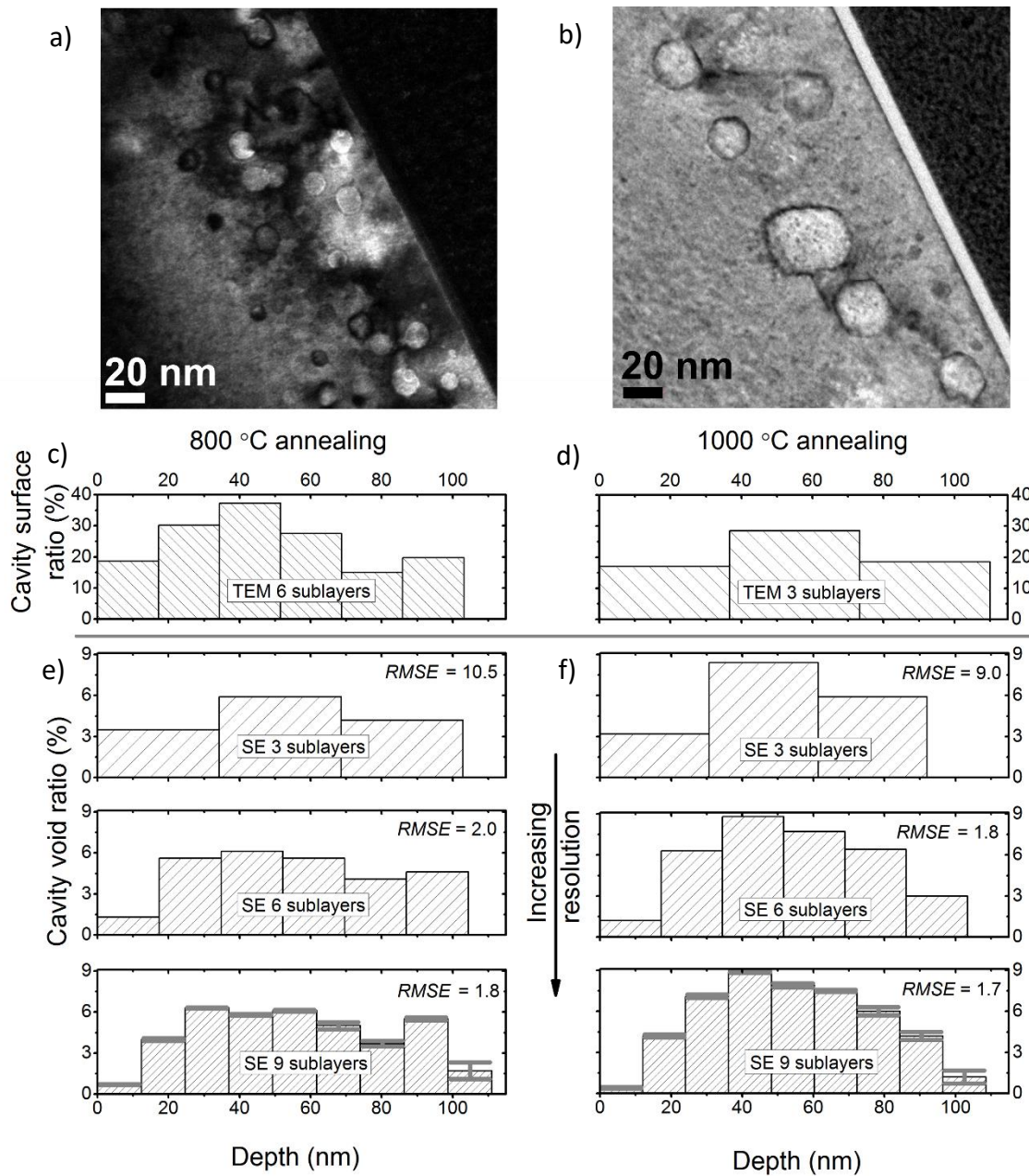


Figure 2.4: Small portions of TEM images displaying cavity morphology (a and b), 2D cavity depth distribution from TEM analyses (c and d) and 3D cavity depth distribution from SE evaluation fitted with 3, 6, and 9 number of sublayers showing an increasing depth resolution (e and f). Left set corresponds to the 800 °C annealing, right set to the 1000 °C annealing of the samples covered by a 130 nm sacrificial oxide implanted at a fluence of $4 \times 10^{16} \text{ cm}^{-2}$.

Although our current EMT-based SE model cannot describe cavity size or size distribution, it can account for a better depth resolution than those obtained from TEM images. For some of the samples, where cavities are too small or not well separated as seen on the TEM micrographs, 2D cavity content is impossible to obtain. In these cases, SE evaluations can still account for the volume content of these cavities from the fitting of multiple EMLs.

2.4.2 Implantation and annealing dependencies on cavity formations

One of the most apparent effects on cavity formation is the thickness of the sacrificial oxide layer through which the He radiations have been made. There is obviously a decrease of the cavity layer depth and also of the total cavity layer thickness when increasing the oxide thickness as demonstrated in Fig. 2.5. Represented samples are implanted by a fluence of $4 \times 10^{16} \text{ cm}^{-2}$ and annealed at $800 \text{ }^\circ\text{C}$. In this case for the $130 \rightarrow 150 \rightarrow 170 \text{ nm}$ oxide layer increase, a shift of $114 \rightarrow 87 \rightarrow 55 \text{ nm}$ for the depth of the cavity layer is observed, respectively.

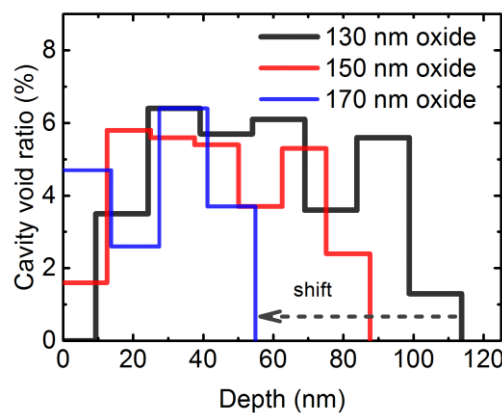


Figure 2.5: Sacrificial oxide dependency of the cavity distribution of the $4 \times 10^{16} \text{ cm}^{-2}$ implanted, $800 \text{ }^\circ\text{C}$ annealed samples.

While the maximum remains relatively the same at $\sim 6\%$ void, there is a slight sharpening at the bottom interface. The total cavity volume, i.e. the area under the curves in Fig. 2.5 changes the following way: $479 \rightarrow 373 \rightarrow 242 \text{ nm} \times \text{unit surface}$. This shift is observable for all the other implantation and annealing conditions (cf. Figs. 2.8, 2.9 and 2.10), but for the low fluence implantation ($2 \times 10^{16} \text{ cm}^{-2}$) through the 170 nm oxide, the cavity layer from the SE evaluations

reveal no depth structure and only a very small ($\sim 1\%$) void near the surface region (Fig. 2.10). This can be clearly explained by both the low density of initial vacancy-helium clusters due to the low He fluence and by the surface proximity allowing higher exodiffusion of He and surface absorption of the vacancies.

The second studied effect on the cavity layer structure is the fluence of the implantation. In Fig. 2.6 we can see the change of cavity void distribution for an increase of the fluence demonstrated with the sample covered by a 130-nm sacrificial oxide layer and annealed at 800 °C. There is a very large increase in the void density when the ion fluence changes from 2 to $6 \times 10^{16} \text{ cm}^{-2}$ (low, medium and high fluences). But more surprisingly, a shift of the peak from the bottom interface to the upper part of the cavity layer can also be seen. The total cavity volume changes in the following way: $164 \rightarrow 479 \rightarrow 1418 \text{ nm} \times \text{unit surface}$. These changes in the cavity distribution as a function of the ion fluence can be seen for the other samples as well (cf. Figs. 2.8, 2.9 and 2.10). A further general tendency is that the peaks are more broadened and less distinctive for the medium fluence, and these peaks tend to reach entirely the top interface at high fluences for the samples covered by a 150 or 170 nm sacrificial oxide.

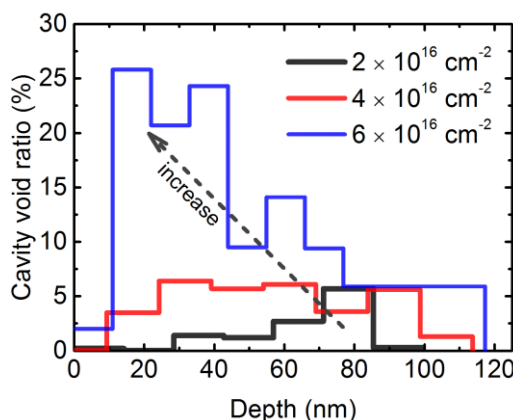


Figure 2.6: Fluence dependence of the cavity distribution of the samples covered with 130 nm sacrificial oxide layer and annealed at 800 °C.

The last investigated effect on the implanted samples is the influence of the annealing temperature on the evolution of the cavity distribution. Even with only three different

temperature conditions we can interpret some form of evolution. In Fig. 2.7, the temperature dependence of the cavity distribution of the samples covered with 130 nm thick sacrificial oxide layer and implanted at a fluence of $4 \times 10^{16} \text{ cm}^{-2}$ is shown. We can observe a sharpening in the cavity volume distribution peak while the total cavity volume is maintained constant (within 15%) when increasing the annealing temperature. The total cavity volumes are 548, 479, 572 $\text{nm} \times \text{unit surface}$ (corresponding to 4.7, 4.2, and 5.0% mean void ratio) for the 650, 800 and 1000 °C annealing temperatures respectively. A similar sharpening can be seen for the samples covered with 150 nm oxide and implanted with $4 \times 10^{16} \text{ cm}^{-2}$ fluence (Fig. 2.9). Additionally, the cavity density distribution often reveals a second peak closer to the bottom of the implanted layer (cf. Figs. 2.8, 2.9 and 2.10). Similar peaks have been also observed in Ref. [36] with SE and TEM analyses.

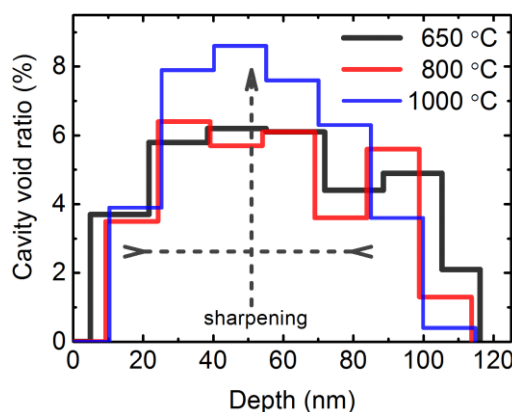


Figure 2.7: Temperature dependence of the cavity distribution corresponding to the samples covered by a 130 nm thick sacrificial oxide layer and implanted at a fluence of $4 \times 10^{16} \text{ cm}^{-2}$.

TEM studies revealed that the size of the cavities increases with increasing isochronal annealing temperatures [36], as would be expected, but the growth mechanism is still not entirely clarified. Previously, analyses of *in situ* TEM measurements suggested an Ostwald ripening (in the temperature interval of around 650–850 °C [45], or between 570 and 700 °C [46] as was also suggested due to the disappearance of the second peak with increasing annealing temperatures [36]. Later however, with a better processing and analyzing of the

video clips, Donnelly concluded that it must rather be migration and coalescence (at least in the temperature interval between 780 and 840 °C) (cf. p. 337 in Ref. [47]). At these temperature intervals migration is induced by the surface diffusion of adatom and surface vacancies at the surface of the bubbles (the activation energy of bulk diffusion is higher). Theoretical analysis also suggests migration and coalescence (700–1000 °C) [48] as does molecular dynamic simulations (but made at elevated simulation temperature of 1400 °C to decrease the demanding computations) [49].

Another general tendency can also be observed concerning the temperature evolution. For almost all of the samples the total void volume ratio has the following order depending on the temperature: “800 °C” < “650 °C” < “1000 °C”. To better understand this tendency and the diffusion dynamics in general, an *in situ* SE annealing investigation with the developed model would be recommended for future studies.

2.1 Conclusions

In this chapter I demonstrated that with multilayered effective medium models the in-depth profile of implantation-induced defects, and of annealing-induced cavities can be evaluated with SE at as good or better depth resolution than with the analysis of TEM micrographs. Various implanted Si substrates have been investigated as a function of the implantation fluence, the annealing temperature, and the thickness of the sacrificial oxide layer covering the Si. The cavity layer decreases and shifts to the surface with increasing oxide thickness. The total cavity volume increases significantly, when increasing the fluence, while the peak of the cavity densities becomes more localized to the surface region. The annealing temperature induces a sharpening of the peak of the cavity distributions while maintaining the total cavity volume nearly unchanged.

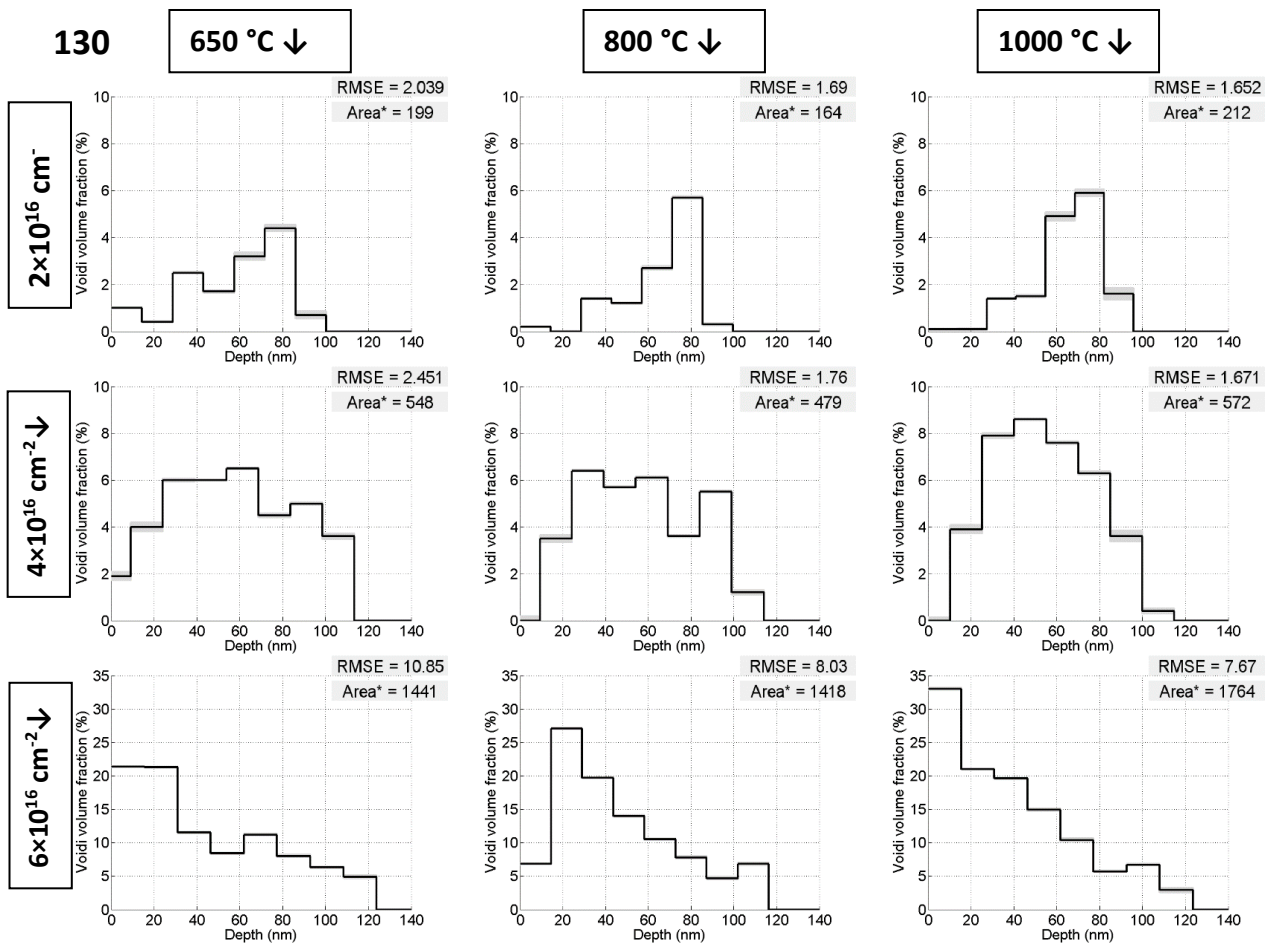


Figure 2.8: All of the cavity in-depth distribution of the samples covered by a 130 nm sacrificial oxide layer.

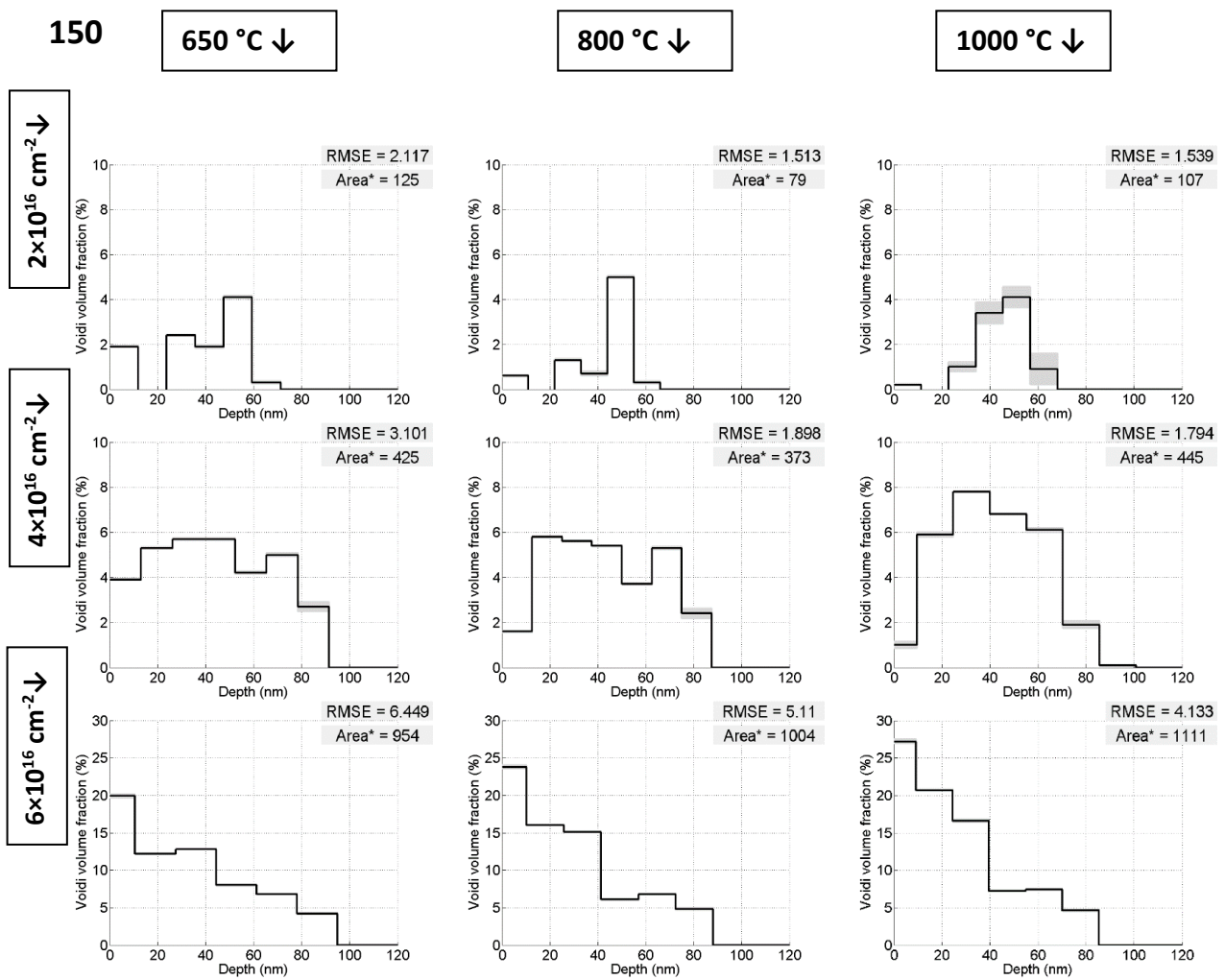


Figure 2.9: All of the cavity in-depth distribution of the samples covered with a 150 nm sacrificial oxide layer.

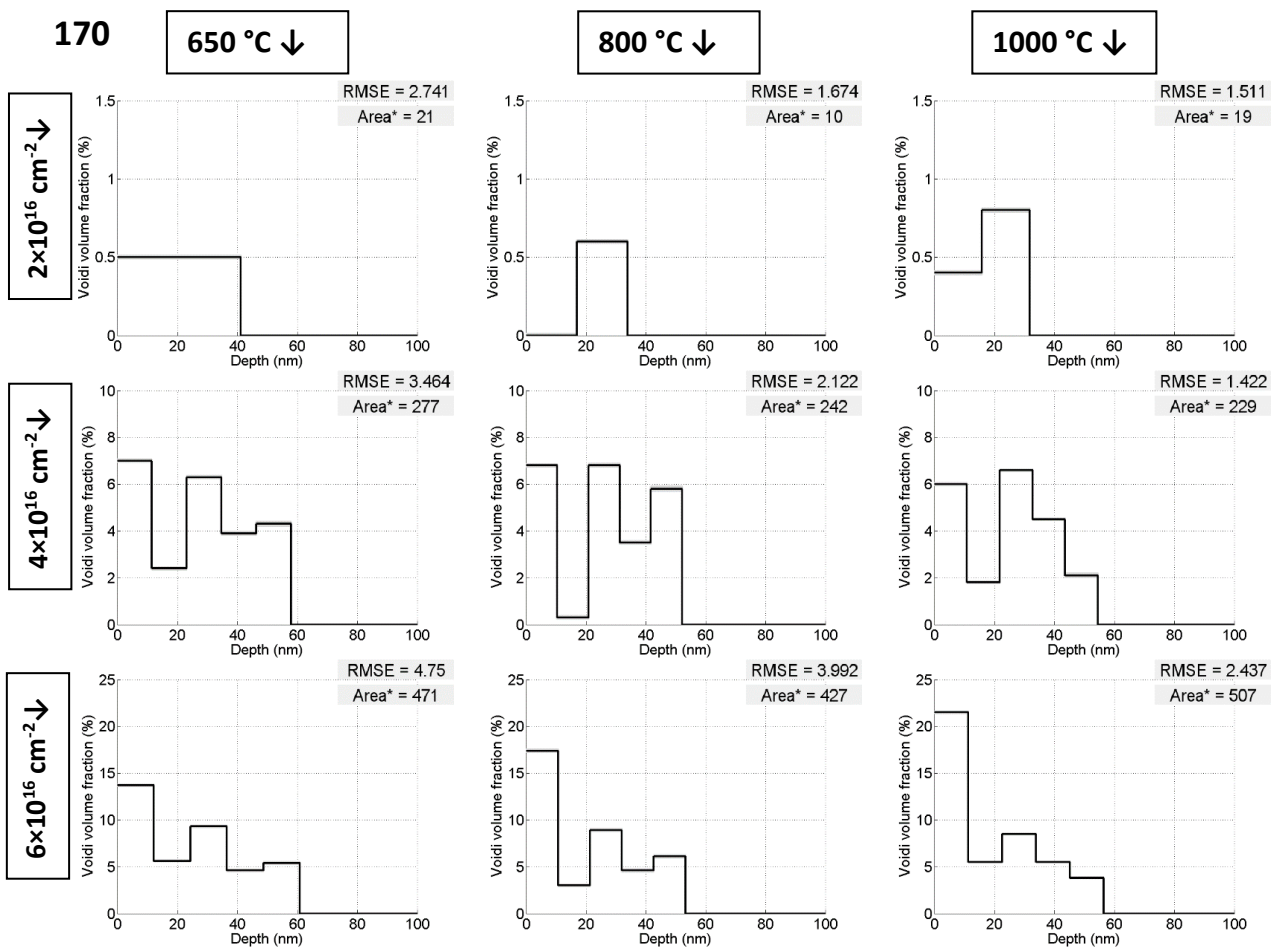


Figure 2.10: All of the cavity in-depth distribution of the samples covered with a 170 nm sacrificial oxide layer.

3 Porous silicon layers of broad thickness range

In the nineties, porous silicon (PSi) layers aroused enthusiasm due to its potential for (tunable) photoluminescence [50]. Since then, mostly over the last few years, many other possible industrial applications appeared due to its relative ease of fabrication and low production cost. For example, they can be used in microelectronics thanks to their electrical insulating properties [51]. Many of the applications are based on the structural feature of having a high specific surface area (surface to volume ratio). For instance, PSi layers have been shown to excel as chemical [52] or biosensors [53]. Both structural and chemical properties of PSi layers are key parameters in order to obtain the desired properties (p. 202/203 in Ref. [54]). For this purpose, indeed, electrochemical parameters (current density, electrolyte composition...) allow a fine tuning of the micro- or nanostructure: porosity, pore size or specific surface area [55]. On the other hand, the control of the surface chemistry (through oxidation, carbonization or metallization) is also indispensable to functionalize and stabilize PSi layers with the expectation of a better reliability [56].

Most of the above-mentioned applications of porous silicon require the synthesis of thin films on large surfaces to lower the production costs. However, nowadays porous silicon manufacturing is mainly limited to low throughput and small surfaces (a few cm²) for laboratory applications. Apart from the issues related to PSi manufacturing on large surfaces with good lateral homogeneity [57], accurate characterization of PSi is also challenging. Furthermore, in order to mechanize PSi layers in an industrial process flow, there is a need to set up a fast, reliable and non-destructive control of porous characteristics. Non-destructive porosity measurement techniques can generally be sorted depending on layer thickness. For ultrathin layers (less than 300 nm), X-ray techniques can be used such as X-ray reflectometry [58] or grazing-incidence small-angle X-ray scattering [59]. These techniques provide an accurate

measurement of the very superficial layer. When it comes to thicker layers, infrared spectroscopy is the most frequently used technique in the form of Fourier transform infrared spectroscopy (one reflectance spectrum) [60], infrared emittance spectroscopy [61] or spectroscopic liquid infiltration method (two reflectance spectra interfered) [62].

Since the 1980s several studies report spectroscopic ellipsometric characterizations of PSi layers using models with increasing complexity to obtain the most, physically relevant information complementing other techniques [63–74], such as layer thickness, porosity, inhomogeneity and anisotropy. Additionally, with the help of an adsorption setup, ellipsometric porosimetry can be performed [75] which enables pore size distribution evaluations. With illumination in the visible, ultraviolet and near infrared range, SE has a great potential to sensitively characterize PSi up to a few μm thick layers. However, for larger thicknesses, interference oscillations become too dense to be accurately resolved with multichannel detection systems. Of course, measurements with high-resolution monochromators could attain a better result, and thus thicker layer investigations would be possible (around 10 μm thickness). However, a wide spectral range measurement, which is necessary for accurate porosity content and porosity distribution determination, in this way would take orders of magnitude more time (\sim one day) than multichannel measurements. To surpass this limitation, mid-infrared (MIR) ellipsometric measurements performed on the porous samples allow the characterization of up to several tens of micrometers in thickness [T3]. Additionally, with visible ellipsometry it is difficult to separate the optical response of the oxide content from the porosity thus diminishing individual sensitivity for both [68,76–78]. However, with MIR ellipsometry, where this optical separation (in refractive index and extinction coefficient) is enhanced, due to the molecular resonance peaks of silicon dioxide [79], sensitivity is much greater for quantitative analysis of the oxidation level [61,T3].

PSi can be classified according to its typical pore size. The categorization originates from the context of physisorption [80]. In this chapter, I will focus on the characterization of

mesoporous Si layers, i.e. with pore diameters in the range of 2–50 nm, covering a wide thickness range measured with both visible and MIR ellipsometers. I was able to combine the advantages of the two measurements such as surface sensitivity in the visible and composition sensitivity in the infrared range and to demonstrate their individual limitations [T3]. I developed different optical models for ellipsometric evaluations with increasing complexity to achieve best fit on the measured spectra while maintaining low fit error and low parameter CCs, and thus obtained physically plausible and relevant information about the samples. To summarize in advance, this relevant information includes: porous layer average thickness, thickness non-uniformity, average porosity, in-depth porosity gradient, oxidation level and surface roughness. Anisotropy will somewhat be addressed in this chapter, but the next one (Chapter 4) will have its main focus on it with different sample sets.

3.1 Experimental details

3.1.1 Porous silicon etching conditions

The silicon layers of the present study were made at GREMAN by electrochemical etching of a monocrystalline silicon wafer in a 30 wt. % hydrofluoric acid (HF) – acetic acid (25 wt. %) solution. Fig. 3.1 schematically shows the formation process of the pores. The main driving force is the potential difference between the metallic cathode (Pt) and the Si substrate acting as anode. The oxide, locally grown at the Si surface, is dissolved by the HF present in the

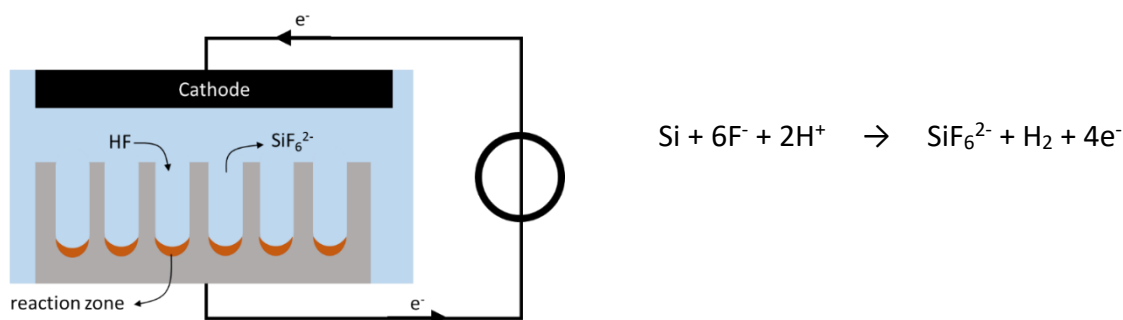


Figure 3.1: Schematic depiction of porous silicon formation in a hydrofluoric acid solution driven by an electrical potential and the equation of the principal (half-)reaction.

solution. Therefore, the formation of porous Si can be attributed to the competition of Si oxidation and silicon oxide dissolution by HF. If Si oxide grows too fast compared to its dissolution, another phenomenon, electropolishing occurs and pores will not form (pp. 5 ff. in Ref. [56]).

We focus on mesoporous silicon, i.e. with pore diameters in the range of 2–50 nm [80], obtained from (100)-oriented highly-doped n-type (0.01–0.015 $\Omega\cdot\text{cm}$) silicon. Anodizations were carried out in a single tank electrochemical cell with a surface of silicon exposed to the electrolyte with 5 cm^2 . By changing the anodization current density and duration, both thickness and porosity of the layers can be adjusted. After the electrochemical etching step, the PSi layers were carefully rinsed with deionized water and dried on a hotplate (120 $^\circ\text{C}$) to remove the remaining electrolyte- from the pores. TABLE 3.1 summarizes the electrochemical conditions of the different PSi layers investigated in the present work. The respective dimensions of the thin layers (samples N-01 to N-08) are determined with the help of UV-NIR ellipsometer and are distinguished from thicker layers (samples N-09 to N-11) whose characteristics are measured by FTIR ellipsometry. The PSi layer thicknesses have also been determined by scanning electron microscopy. Figs. 3.2a and b show samples with porous layer thicknesses of 3.3 μm (N-08) and 52 μm (N-11), respectively, focused at the silicon/porous silicon interface.

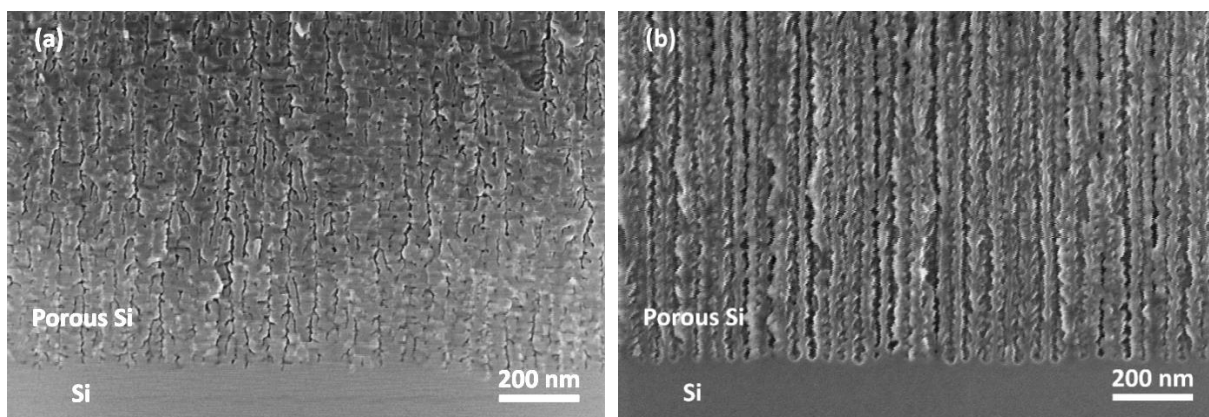


Figure 3.2: SEM images of (a) sample N-08 and (b) N-11 focused at the silicon/porous silicon interface.

TABLE 3.1: Electrochemical etching conditions and thickness measurement values of the investigated porous silicon layers.¹¹

Sample notation	Current density (mA/cm ²)	Etching duration (s)	Thickness by SE ¹² (μm)	Thickness by SEM (μm)
N-01	14.5	15	0.7	0.7
N-02	14.5	30	1.2	1.3
N-03	14.5	60	2.4	2.3
N-04	14.5	120	4.2	4.4
N-05	116.3	2	0.7	0.7
N-06	116.3	4	1.2	1.3
N-07	116.3	6	1.8	1.8
N-08	116.3	12	3.3	3.4
N-09	80.0	210	23.0	25.0
N-10	80.0	300	31.3	31.0
N-11	80.0	600	52.0	52.0

3.1.2 Porous silicon oxidizing conditions

It is well-known that PSi layers can be oxidized by various methods, including thermal oxidation (wet or dry), chemical oxidation or electrochemical oxidation (pp. 191-195 in Ref. [56]). We used p⁺-type (0.02 Ω.cm) samples to study the chemical composition of PSi layers after oxidation. A 6-inch silicon wafer was anodized with the same electrochemical conditions as sample N-10, and then cut in pieces. Oxidation was performed either by dry thermal oxidation in an O₂-rich atmosphere in a tubular furnace or by electrochemical oxidation in an aqueous solution composed of 10 wt. % acetic acid. After electrochemical oxidation, the oxidized PSi layers were rinsed with deionized water and dried on hotplate (120 °C). To improve the density of the electrochemical oxide, a high-temperature annealing post-treatment is usually performed [81]. Densification annealing was carried out with the same recipe as

¹¹ SE evaluation results are shown in Fig. 3.10.

¹² Thickness by SE values for N-01–N-08 are averages from UV-NIR and MIR fit results, while for N-09–N-11 they are obtained solely from MIR fit results.

thermal oxidation reference. TABLE 3.2 summarizes the different oxidation conditions investigated in the present chapter.

TABLE 3.2: List of investigated oxidized samples with oxidation technique and experimental condition descriptions.

Sample notation	Oxidation technique	Experimental conditions
Ox-ref	Reference sample without any post-treatments	Anodization in 30-wt.% HF and 25-wt.% acetic acid, using a current density of 80 mA/cm ² for 300 s.
Ox-1	Pre-oxidized sample	Ox-ref + thermal oxidation at 300 °C in O ₂ for 1 h
Ox-2	Electrochemically oxidized sample	Ox-ref + anodic oxidation (10 mA/cm ² for 0.5 h) in 10-wt.% acetic acid
Ox-3	Densified electrochemically oxidized sample	Ox-2 + thermal oxidation at 800 °C in O ₂ for 1 h
Ox-4	Thermal oxidation for 30 min	Ox-ref + thermal oxidation at 800 °C in O ₂ for 0.5 h
Ox-5	Thermal oxidation for 60 min	Ox-ref + thermal oxidation at 800 °C in O ₂ for 1 h

3.1.3 Ellipsometric measurement setup

The SE measurements performed on the PSi samples were made with an optical (ultraviolet-near-infrared, UV-NIR) and a MIR ellipsometer allowing evaluations in a wide spectral range. The UV-NIR measurements were performed with the same ellipsometer already introduced in the previous chapter (Woollam M-2000DI). The angles of incidence of the illumination were chosen to be between 65° and 75° producing a length of 4.7 and 7.7 mm for the major axis of the elliptical spot (2 mm for the minor axis). The MIR measurements were performed with a Semilab IRSE equipment¹³, which is a variable angle FTIR ellipsometer. This setup allows a spectral width of 600–7500 cm⁻¹ (1.3–16.7 μm) with a very high resolution of

¹³ Access to Semilab IRSE was allowed during my PhD studies in Hungary, at the Semilab Corporate Headquarters, Prielle Kornélia str. 2. H-1117 Budapest; semilab@semilab.com.

about 0.5 cm^{-1} , when using a liquid nitrogen cooled HgCdTe detector. Due to the resolution capabilities, IRSE is ideal for the measurement of layers of several $10 \text{ }\mu\text{m}$ thickness, as it can resolve the interference oscillations in the ellipsometric spectra. Infrared illumination at an angle of incidence of 70° through an aperture was chosen in our case to produce a spot size of 4 mm , as it is a good compromise to minimize PSi layer thickness non-uniformity on the illuminated area, while having a more than adequate reflected light intensity.

I evaluated the recorded ellipsometric spectra with the version 5.04 of the Woollam CompleteEASE and with the Semilab SEA v1.2.30 data analysis software products. The *RMSE* was defined with the usual *N*, *C* and *S* values for the UV-NIR measurements, but for the measurements performed with the IRSE ellipsometer functioning with a rotating analyzer, it is best to define the *RMSE* with $\alpha = -\cos(2\Psi)$ and $\beta = \sin(2\Psi)\cos(\Delta)$ as for this case they are the values directly related to the intensity harmonics [3,82], (pp. 523–534 in Ref. [83]). Additionally, I made the fitting separately on the spectra of the two measurements (for the same sample) to avoid weighting of the ellipsometric values due to the conversion from either of the ranges and also because the illumination is not sure to be incident on the same spot on the samples (with further complications arising from lateral inhomogeneities).

3.2 Optical model development

Many authors have shown, that for PSi layers, effective medium theories work perfectly [63–68,70–72,84–86]. For the modeling of the PSi layers listed in this chapter, I also chose the Bruggeman effective medium approximation (B-EMA, cf. Ch. 1.6.3) because the typical pore dimensions are much less ($< 50 \text{ nm}$) than the wavelength of the illuminating light, and so diffraction and non-specular scattering are negligible. Furthermore, expected porosity content and characteristic size of the Si skeleton is such that changes in the optical response due to nanocrystallinity (quantum confinement effects) are negligible, and so the effective medium layers can be consisted of varying ratio of bulk monocrystalline silicon (c-Si) and void with

additional stoichiometric SiO_2 present in the oxidized samples (two- or three-component B-EMA). The complex dielectric functions required for the B-EMA formulas were taken from the literature for c-Si and SiO_2 in the UV-NIR [39], and from reference n and k measurements (as included in the Semilab software) for the MIR range (Fig. 3.3).

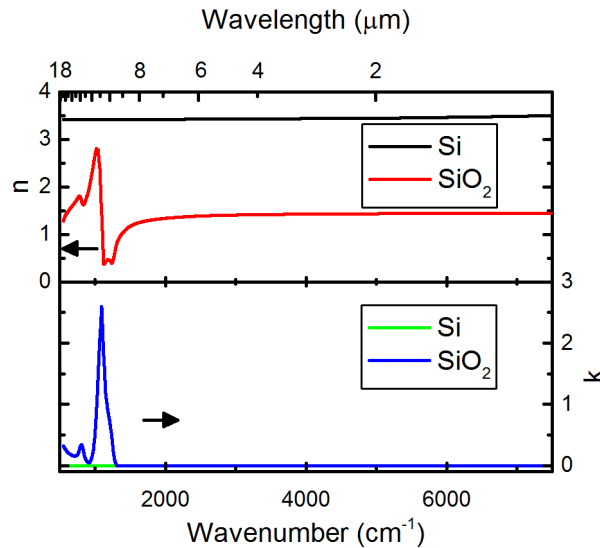


Figure 3.3: Reference optical constants (n and k) for Si and SiO_2 as included in the Semilab software.

The PSi layers span across a large thickness range, and above around $5\ \mu\text{m}$ the interference oscillations in the ellipsometric spectra become too dense to be resolved by UV-NIR measurements. As a consequence, two modeling schemes are considered. For the samples with a nominal thickness smaller than $5\ \mu\text{m}$ (N-01 to N-08) similar optical models can be used for the UV-NIR and MIR spectra, that is, one or more EMLs describing the porosity on top of a semi-infinite c-Si substrate. On the other hand, for the thicker layers (N-09 to N-11), fitting is only done at the shorter wavelengths (191–700 nm) for the UV-NIR measurements, describing the surface and near-surface porosity with a B-EMA layer and a separate semi-infinite B-EMA layer for the underlying part, without sensing the bottom of the porous layer due to the light absorption of the c-Si (thus the unresolvable 700–1690 nm part of the spectra are excluded from the fitting). For the MIR measurements of the thicker PSi layers, I chose the

part where the interferences can be well resolved (at longer wavelengths) for the fitting procedure, allowing a thickness and porosity evaluation similarly to the thinner samples.

3.2.1 Comparison of increasingly complex models

In Fig. 3.4, four different optical models are shown with increasing complexity. The top row represents the model structure, while the bottom row is a fit example, specifically, it is the difference between fitted and measured Ψ and Δ values for N-02 (1.2 μm thick PSi layer) measured at the UV-NIR range at 3 different angles of incidence. The number of independently fitted parameters (P) and $RMSE$ values are also shown. To describe porosity inhomogeneity in depth, multiple stacked B-EMA layers were used similarly to the model of the previous chapter describing cavity in-depth distribution. However, in case the sublayers are independently fitted, i.e. the thickness and void parameters are uncoupled between the different sublayers as shown

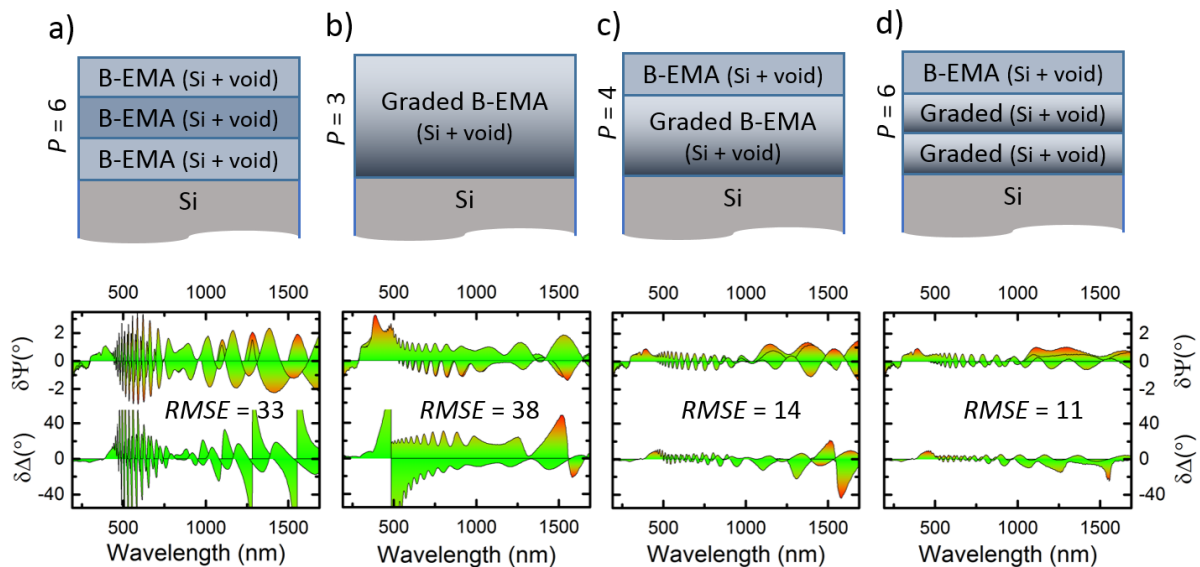


Figure 3.4: Ellipsometric models (top row) and difference (bottom row) between the measured and fitted Ψ and Δ values (for incident angles of 65° , 70° and 75°) of sample N-02 (1.2 μm PSi layer). The difference spectra belonging to the different angles of incidence are plotted conjointly as the area under the curves, thus pointing out the largest difference at each wavelength. Three independent effective medium layers (model M1) as leftmost (a), graded (model M2) as middle left (b), graded with surface roughness (model M3) as middle right (c) and coupled double-graded (model M4) as rightmost graph (d). Root-mean-square error of the fits ($RMSE$) and number of fitted parameters (P) are also shown.

in Fig. 3.4a, then the number of sublayers (m) cannot be increased to more than 3 (model M1), because parameter CCs become too high, making the fitted results questionable or even unphysical. Of course, by coupling the thickness values of the sublayers, we can slightly increase m (one or two additional sublayers), but other simulation artifacts can also appear if the void values are fitted independently to describe a continuous porosity gradient. In fact, simulations of a multi-EML structure, where a difference of porosity content more than a few percent between two neighboring independent sublayers is present, will cause additional small interference oscillations absent in the measurements (see Fig. 3.4a).

An improved model consists of a graded EML structure; in this case, the in-depth porosity gradient is described by a simple linear function with 3 fitted parameters: global thickness of the PSi layer and void ratios at the top and the bottom of the porous layer (model M2). As it can be seen from Fig. 3.4b, this model addresses the artificial oscillations seen in Fig. 3.4a, but a global difference of higher rate appears between the fitted and measured ellipsometric angles. Although there is a slight increase in the *RMSE* values compared to those obtained with the previous model, the few number of fit parameters indicates that the simple linear description of the porosity gradient is a good basis for further model improvements. The most probable reason why M2 does not produce a merit of fit as good as in the case of M1 is because with M1 the surface roughness was indirectly included as the top EML, which is not the case for M2. If we include a surface roughness layer on top of the graded linear layer (model M3), we will have a very good merit of fit, as it is demonstrated in Fig. 3.4c. Usually, the surface roughness layer is defined as a B-EMA layer composed of 50% void and 50% of the underlying layer, but in our case to better describe the unique surface of the porous silicon, no such fixation of the composition ratio has been made, i.e. a separate EML of c-Si and void with fitted thickness and void ratio has been chosen. Foreshadowing the last part of the thesis (Chapter 5), we already showed here the importance of a surface roughness layer in our optical models, and the effect of neglecting it.

A further improvement of the models is to consider an interface layer between the bottom of the PSi layer and the top of the substrate. For this purpose, a second graded EML structure was added as an interface in such a way that the top c-Si/void ratio of this layer is coupled to the bottom of the main graded EML structure and the bottom of this interface diminishes to zero void percent (model M4). The typical thickness values for the surface roughness (the top EML) are $\sim 10\text{--}20$ nm, for the bottom interface (the bottom EML) are $\sim 60\text{--}100$ nm, while the main graded EML gives up the rest of the PSi layer thickness for the samples thinner than $5\ \mu\text{m}$ (N-01 to N-08).

The infrared illumination is insensitive to the surface roughness and the bottom interface layer and so I have excluded them from the MIR evaluations, the simpler M2 model is more suitable for these cases. A scheme of the model M4 and a relative fit example can be seen in Fig. 3.4d. As it can be seen from the *RMSE*, there is an improvement in the fit quality compared to M3 but at the expense of two additional fit parameters. Nevertheless, if compared to M1 which has the same number of independent fit parameters, we obtain an increase in the fit quality by a factor of three, indicating that it is a proper optical model to accept. A further small improvement of fit quality can be attained by modeling thickness non-uniformities (model M5), slightly for samples N-01–N-08, more so for samples N-09–N-11. Thickness non-uniformities are modeled by convolving the data from multiple different generated data sets (set to 9 as default) with the model thickness varied over a range of values (Fig. 3.5a). For the samples N-01–N-11, I tested anisotropic optical models as well (anisotropic B-EMA, cf. Ch. 1.6.3), but fitting revealed that for the thinner layers it had no, or negligible effect on fit quality, while for the thickest layers, anisotropy of the layer has similar, but only a mild, effect on the evaluations as porosity depth inhomogeneity. In the following chapter (Chapter 4), I will utilize more advanced EMAs to model the morphological evolution from isotropic to highly anisotropic PSi layers.

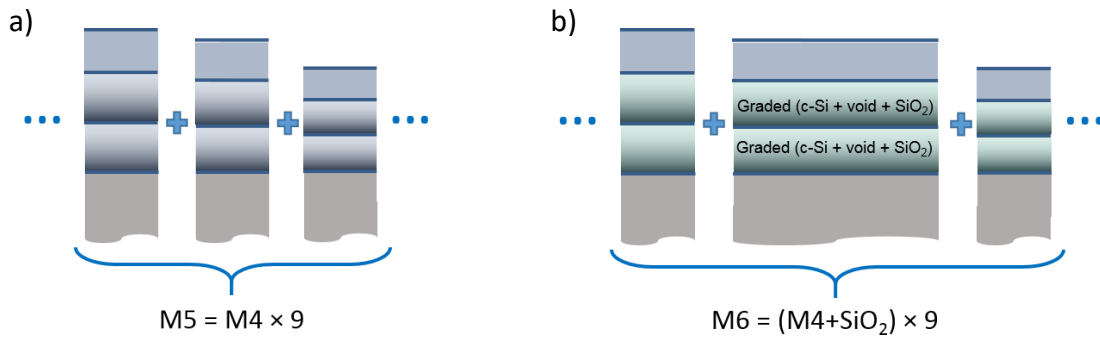


Figure 3.5: Schematic depiction of model $M5$, which incorporates the total layer thickness inhomogeneity by convolving multiple data sets calculated from $M4$ (a) and of model $M6$, which is similar to $M5$ but with the 2 component B-EMA replaced with 3 component counterparts (b).

3.2.2 Influence of the number of sublayers

It is important to note that because the ellipsometric models used for the simulation of the reflections consider optically homogeneous layers, any EML gradient described by a function must also be discretized into homogeneous sublayers. Because of computer CPU time considerations, choosing arbitrarily large number of sublayers is disadvised. To find the optimal number of sublayers (m), I investigated how the fit quality depends on it (see Fig. 3.6 for samples N-01 to N-04). The *RMSE* converges to a certain value, but the convergence degree

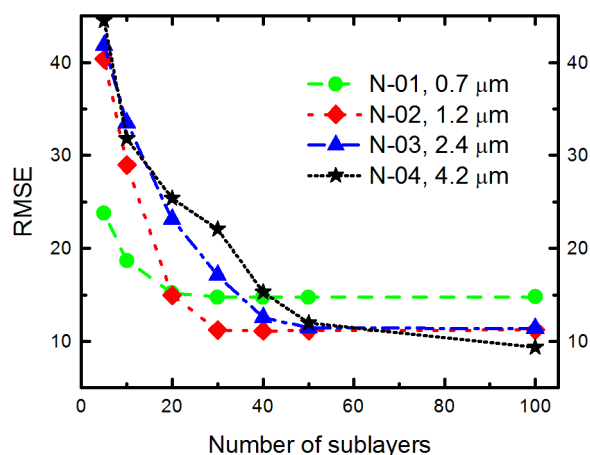


Figure 3.6: Root-mean-square error (*RMSE*) dependency as a function of the number of effective medium sublayers used in model $M5$ for fitting four of the *PSi* samples with different thicknesses (samples N-01 to N-04).

depends on the thickness: for thinner PSi layers, the *RMSE* will not improve significantly with *m* more than 20–30 while for the thickest PSi layers, 50 sublayers are preferred for the best fit.

3.2.3 Oxidation effects

As mentioned at the beginning of the chapter, the oxide content within the pores cannot be sensitively quantified with UV-NIR measurements, because it strongly correlates with the void content. In fact, the dielectric function of the oxide has a very small dispersion in the visible and near-IR wavelength range, and so when fitting to both porosity and oxide volume content, they highly cross-correlate, often leading to unphysical values when they are not bounded. By contrast, when fitting with a two component B-EMA (c-Si + void), the “void” parameter will represent the void and oxide volume content simultaneously. Because a porous layer with some SiO₂ instead of void would be a layer optically denser (higher refractive index – *n*), fitting the PSi layer only with Si and void components slightly underestimates the porosity. As expected oxide content would be only a few percent, this underestimation is negligible. This limitation can be surpassed by fitting the MIR measurements due to the characteristic line-shape of *n* and extinction coefficient (*k*) of SiO₂ at around a wavenumber of 1100 cm⁻¹ caused by molecular resonance peaks. To this end, the two-component EML was supplemented by an additional SiO₂ component (model M6, Fig. 3.5b) of which the *n* and *k* optical parameters were obtained from reference thin layer measurements. The SiO₂ component was modeled in a way to not have any in-depth distribution for simplicity.

In Fig. 3.7, the effect of such SiO₂ content is demonstrated with the simulation of a 20 μm thick PSi. The top graph shows the Ψ and Δ values in a narrow spectral range at an angle of incidence of 70° for a B-EMA composed of 60% Si, 40% void and 0% SiO₂, while the bottom graph simulates a B-EMA layer composed of 60% Si, 20% void and 20% SiO₂. The characteristic optical properties of SiO₂ at these wavelengths (see middle graph in Fig. 3.7) have a huge effect on the ellipsometric spectra, which makes the oxide content sensitively quantifiable. Although light absorption of porous layers with large SiO₂ content at peak values of *k* results in an optical

penetration depth (OPD) of only micrometer extent depending on the SiO_2 quantity, the rest of the spectra with lower k (and higher OPD) around the peak is enough to determine the average SiO_2 volume fraction.

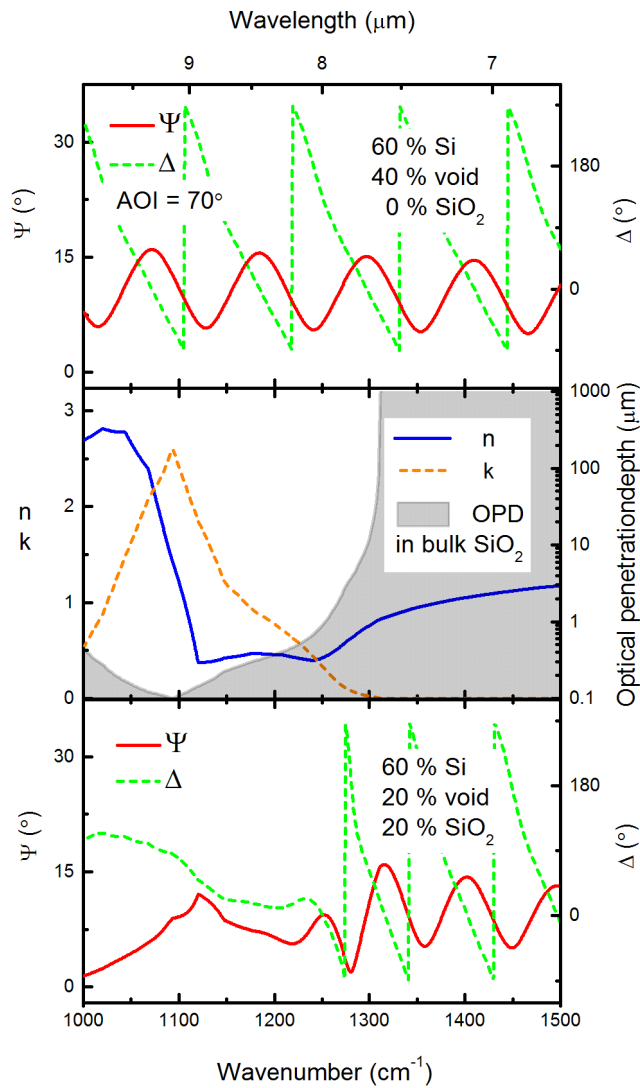


Figure 3.7: Comparison of a simulation of a $20\ \mu\text{m}$ thick effective medium layer with 60% Si, 40% void and 0% SiO_2 (top layer) and of an equally thick effective medium layer but with 20% void and 20% SiO_2 (bottom layer). The effect of the optical properties (n – refractive index, k – absorption coefficient and OPD – optical penetration depth) of the SiO_2 (middle layer) produces a very distinct difference in the simulations around $1100\ \text{cm}^{-1}$.

OPD is also shown for pure SiO_2 in the middle graph in Fig. 3.7. These values could be higher by several factors in a mixed EML, and ellipsometric depth sensitivity is typically three times larger than OPD (see Fig. 4 in Ref. [O10]). Depth profiling (SiO_2 vertical inhomogeneity

characterization) remains difficult, because of the narrow SiO₂ sensitive part of the spectra that can probe the entire layer.

3.3 Evaluation results

3.3.1 Thin porous silicon layers

From the optical models of M5 for UV-NIR and M6 for MIR, evaluations have been made for all the samples with a nominal PSi layer thickness smaller than 5 μm (i.e. for samples N-01 to N-08). For example, Fig. 3.8a (MIR) and Fig. 3.8b (UV-NIR) spectra represent the measured

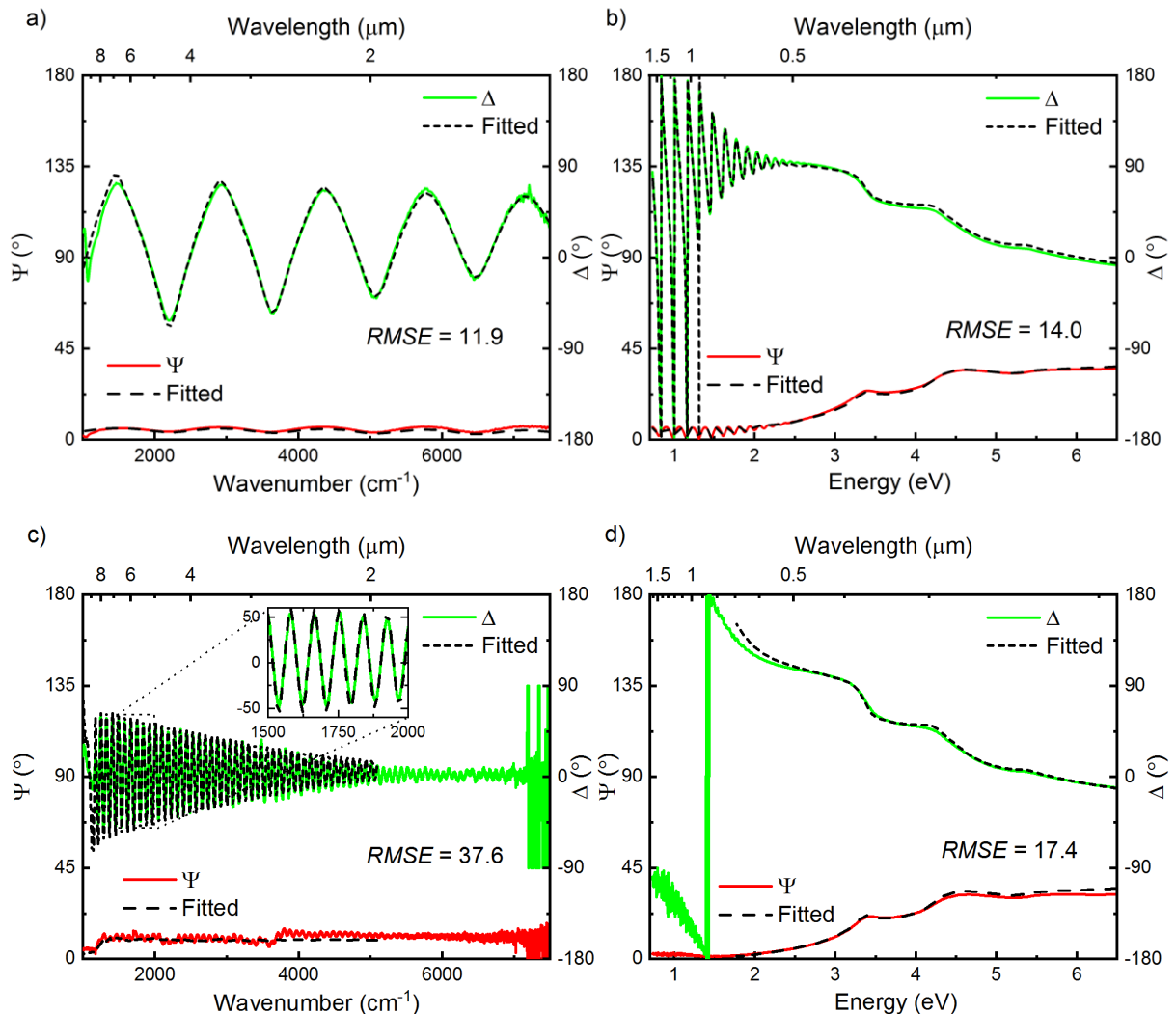


Figure 3.8: Measured and fitted ellipsometric angles of a less than 5 μm thick PSi layer (sample N-06, 1.2 μm thick) in the MIR wavelength range (a), and in the UV-NIR wavelength range (b) and of a more than 5 μm thick layer (sample N-09, 23 μm thick) in the MIR wavelength range (c), and in the UV-NIR wavelength range (d).

and fitted ψ and Δ values for sample N-06 (1.2 μm thick). It can be seen that the fit is excellent throughout the whole spectra for both wavelength range ($RMSE = 14.0$ for UV-NIR fit and $RMSE = 11.9$ for MIR fit). Similar excellent fits can be made on the other thin samples. Fig. 3.9 represents the evaluated thickness values plotted versus the consumed charge density. Results are averaged from the optical and the infrared SE measurements, with a typical difference of 3–4% between the two methods. A clear linearity can be observed, suggesting that, when restricted to this range, the current density has a limited impact on the etch rate of thin PSi layer and so, on the dissolution valence. The fitted ellipsometric thickness values also correlate well with SEM measurements (TABLE 3.1), confirming the optical model validity.

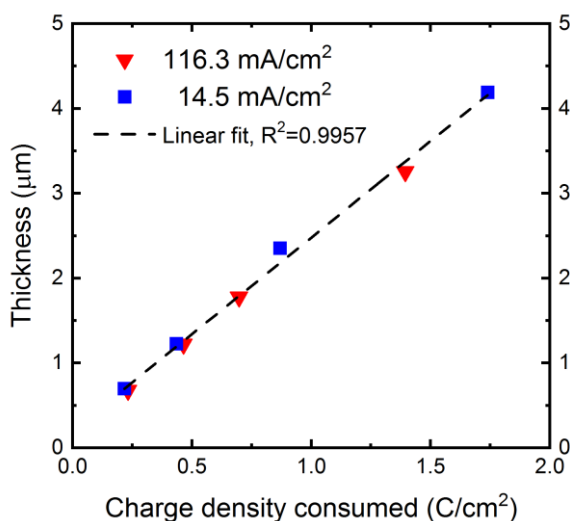


Figure 3.9: Evaluated thickness values for the injected charge density consumed during anodization for the samples obtained at 14.5 mA/cm² and for the ones obtained at 116.3 mA/cm² (samples N-01 to N-08). The results are averaged from the optical and the infrared SE measurements.

In Fig. 3.10a, porosities of the thin layers are shown as a function of the layer thickness. For the UV-NIR measurements fitted by M5, the in-depth average values of the doubly graded layers are shown, while for the MIR measurements, the plotted porosities are the sum of the fitted void and SiO₂ volume fractions obtained by M6. Firstly, it is important to notice that similar results were extracted from either of the spectra appertaining to the two ellipsometers.

Then, no definite characteristic tendencies can be observed; rather, porosities are constant within 6%, although higher current densities typically produce slightly higher porosities for similar layer thicknesses [87]. The relative thinness of the porous layers produced in this study may explain such limited variations in porosity with depth.

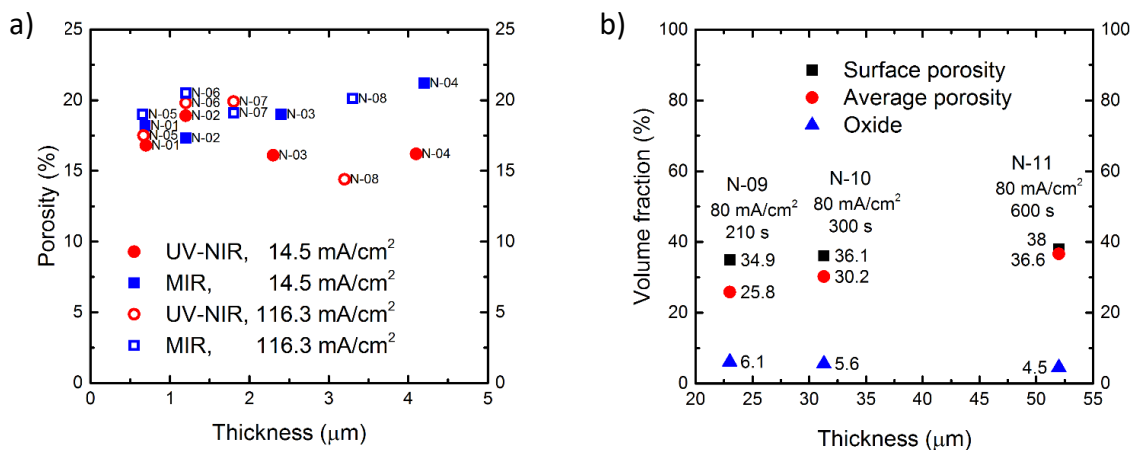


Figure 3.10: (a) Fitted average in-depth porosity values, i.e. void volume fractions for the UV-NIR and sum of void and SiO₂ volume fractions for the MIR measurement in function of the fitted thickness values evaluated with models M5 and M6, respectively, for N-01 to N-08 samples. (b) Surface porosity from UV-NIR evaluations and average porosity and oxide content from MIR evaluations represented by volume fractions as a function of the thickness for N-09 to N-11 samples.

3.3.2 Thick porous silicon layers

As for the thicker layers, an example of a fitted spectra (that of the 23 μm thick PSi, N-09) is demonstrated in Figs. 3.8c (MIR) and 3.8d (UV-NIR). The fits on the MIR spectra are good for wavelengths above 2 μm (below $\sim 5000\text{ cm}^{-1}$). For the remaining part of the wavelength range, the measurements are too noisy and the thickness non-uniformity smears the clear oscillations. Furthermore, fits on the UV-NIR spectra are good for wavelengths below 700 nm (above $\sim 1.8\text{ eV}$). At this wavelength range, there is no reflection from the silicon/porous silicon interface, because the OPD of light in the PSi is much shorter than the layer thickness. Above 700 nm, layer interference oscillations appear, but they are too dense to be resolved and thus fitted.

Porosity results are shown in Fig. 3.10b for the thickest samples (N-09 to N-11). Surface porosity from the UV-NIR evaluations and the average porosity and oxide content from the MIR evaluations are shown. Average porosity increases rapidly with thickness, while surface porosity does so slowly. The rise of average porosity with anodization duration was previously observed on both highly-doped p- and n-type silicon [88–91]. This phenomenon is generally attributed to a diffusion-limited renewal of the electrolyte at the silicon/porous silicon interface during long-duration anodizations. A progressive decrease in HF concentration at the reactive interface implies a simultaneous increase of the porosity [87]. Electrolyte exhaustion is all the more visible when the sample is thick, which explains why this tendency is only observable between the N-09, N-10 and N-11 samples. As for surface porosity, its slight increase with anodization duration can mainly be explained by a pure chemical etching phenomenon of silicon by HF (p. 23/24 in Ref. [92]).

3.3.3 Oxidized porous silicon layers

Concerning the evaluations of the oxidized porous samples, with the help of M6, the different volumetric contents (Si, void and SiO₂ components) could be obtained, as shown in Fig. 3.11a. After being anodized (Ox-ref), the oxide content of the PSi layer is less than 1%. However, a low-temperature oxidation at 300 °C is sufficient to increase the oxide content from 0.9% to 15% (Ox-1), indicating back-bond oxidation [93] in which oxygen atoms are inserted between silicon – silicon hydrides (Si-SiH_x) bonds.

The thermally oxidized samples Ox-4 and Ox-5 exhibit a high oxide content in the structure in which the void content tends to 0% with the oxidation duration. The anodically oxidized samples (Ox-2 and Ox-3) show a lower oxide content than the thermally oxidized ones. The oxide content of sample Ox-3, combining successively electrochemical and thermal oxidation, is surprisingly lower than the one of sample Ox-5, only subjected to thermal oxidation. This result may suggest a pore-closing on top of the layer preventing oxygen diffusion

to the remaining silicon. This hypothesis is confirmed by the significant fraction of remaining void in the electrochemically oxidized sample (almost 13%).

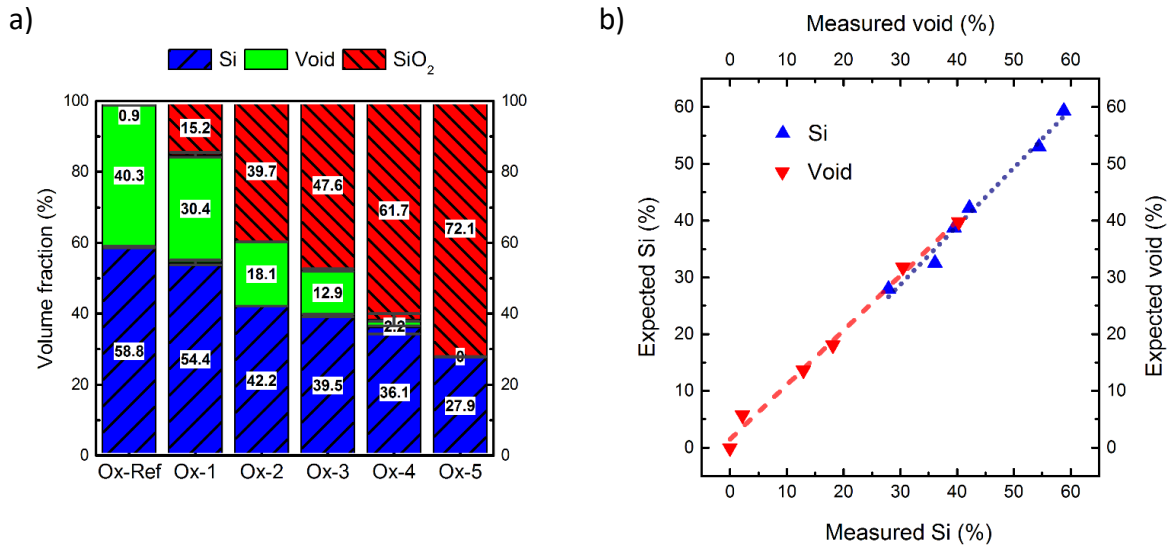


Figure 3.11: (a) Volume fraction percent of the Si, void and SiO₂ contents for the different oxidized porous samples with error bars for Si and void in dark gray obtained by the difference between fitted and expected values. The expected values are calculated from the initial porosity and the measured SiO₂ volume content by taking into account the 44/56 ratio of volumetric expansion when oxidizing Si. (b) Correlation between the independently measured and expected volume fractions (see Eq. 3.1a and 3.1b for the calculation of the expected values).

Volumetric expansion occurs during oxidation as SiO₂ consumes Si to grow. In case of a flat silicon wafer, 44% of SiO₂ total thickness is grown under the initial level of silicon. As a result, if the original porosity without any oxide is known, we can calculate an expected Si and void volume content from the measured SiO₂ volume fractions. In other words, the Si, SiO₂ and void contents are not independent from each other during the porous framework oxidation; the following equations describe their relation:

$$V_{\text{Si}} = 1 - V_{\text{ip}} - 0.44V_{\text{SiO}_2}, \quad (3.1a)$$

$$V_{\text{void}} = V_{\text{ip}} - 0.56V_{\text{SiO}_2}, \quad (3.1b)$$

where, V_{Si} , V_{SiO_2} and V_{void} are the volume fractions of Si, SiO₂ and voids respectively, while V_{ip} is the initial porosity before oxidation [60,94]. I could have implemented these equations in the

fitting procedure coupling these parameters together and reducing the overall number of fit parameters, but I preferred to fit it independently so I could verify the difference between the fitted and empirically calculated values afterwards.

In Fig. 3.11b we can see such an implementation, that is, the strong correlation between independently measured and expected (calculated from V_{ip} and V_{SiO_2}) volume fractions. V_{ip} could be chosen as the void volume fraction of the reference measurement, but a small, probably native oxide is already present (0.9%) in the pores, thus biasing the equations. To correct the volume fraction values of Si and void, the V_{SiO_2} has been extrapolated to 0 and V_{ip} , fitted in such a way as to minimize the measured and calculated V_{Si} and V_{void} . The error values plotted in Fig. 3.11b are the differences between the measured and expected values explained above (the errors from the fit of model M6 are smaller, less than 1%, not shown in the figure). Consequently, as the error values are rather small, the validity of M6 and of the fitted volume fractions are reinforced by this inner cross-check. Moreover, the validity of the model is not influenced by the type of oxide. Indeed, the oxide obtained by electrochemical oxidation can also be characterized accurately. The fit on the oxide content is coarsely based on the Si-O-Si absorption peak around 1100 cm^{-1} , thus making this technique robust and largely independent of the oxidation method.

3.4 Conclusions

Investigation of the PSi layers with optical and infrared ellipsometers allowed analyses in a broad spectral range, and thus the possibility to determine both the thickness (for over two orders of magnitude) and the porosity distribution of the samples. I developed several different optical models with increasing complexity and tested them to describe the porosity content of the layers, such as the multiple independent EML (model M1), graded EML (model M2), graded EML with surface roughness (model M3), coupled double-graded EML with surface roughness (model M4), and M4 with thickness non-uniformity (model M5). I chose the best model in a

way to minimize the *RMSE* while keeping the fitting error and the parameter *CC* low. As for UV-NIR ellipsometry, M5 takes into account the thickness inhomogeneity, surface roughness, pore initiation, in-depth porosity gradient and the silicon/porous silicon interface. I have shown, that UV-NIR ellipsometry is sensitive to surface and near surface characterizations without adequate optical separation of oxide and porosity values, while the MIR ellipsometry, is sensitive to the absorption peak of SiO_2 , and thus can be used to resolve the oxide content by adding a third phase in the effective medium (model M6). I revealed that, thin porous layers show no impact of current density on porosity and thickness when a constant charge density is maintained. For the thick samples, evaluation results highlight the in-depth porosity gradient when the anodization duration exceeds a few minutes, whereas surface porosity only slightly increases. Finally, I compared different oxidation techniques in terms of oxidation level and void content. I have shown, that volume expansion during PSi oxidation follows exactly the same behavior as that during the oxidation of planar silicon wafers. To conclude, I have proven, that with the appropriate optical models, ellipsometry proves to a powerful technique to swiftly and accurately evaluate the characteristics of porous silicon layers.

4 Anisotropic behavior of silicon-based nanostructures

In the previous chapter, I have shown, that SE is capable of analyzing PSi in a large porosity and thickness range. However, one important question remained mostly uninvestigated; The optical anisotropy induced by the preferential orientation of the pore formation.

It is well known that pore propagation during silicon electrochemical etching is governed by the monocrystalline Si wafer orientation [95]. However, the electrochemical parameters and specifically the etching current are also responsible for the pore growth direction and thus its structural anisotropy. If we take the example of mesoporous Si growth in highly-doped Si, at low current density, strongly branched mesopores are observed whereas increasing the current density close to the electropolishing regime leads to the formation of straight pores with smooth sidewalls [87]. Moreover, from an optical point of view, PSi layers produced at high current density present a significantly marked anisotropic behavior [96,T1]. Since the last decade, another promising kind of Si nanostructure is being studied owing to its similar or complementary properties to PSi: silicon nanowires (SiNWs) [97,98]. SiNW layers produced by metal-assisted chemical etching of silicon are in fact nanostructures with even more pronounced geometric anisotropy [98,99,T1].

This chapter has a twofold focus. Firstly, to investigate the transition from isotropic to anisotropic optical behavior of the PSi layers as a function of a broad applied current density range. For this purpose, I developed three different effective medium based optical models: an in-depth graded, an anisotropic and a hybrid one. The systematic comparison of these three models reveal some interesting behaviors. It is important to emphasize that the investigation is made on highly doped p-type Si as opposed to the highly doped n-type Si of the previous chapter, thus general conclusions are probably applicable to the previous investigations as well, but specific results would be different due to the different morphological properties as a

function of the applied current [87]. The second focus is the expansion of the ellipsometric characterization capabilities to SiNWs. As a by-product, optical anisotropy (birefringence – Δn and dichroism – Δk) and morphological parameters are also determined for both PSi and SiNW layers. I developed optical models to obtain fitted parameters for these two kinds of columnar silicon structure.

4.1 Experimental details

4.1.1 Porous silicon layers of a broad porosity range

The PSi layers studied in this chapter were formed by electrochemical etching with the same electrolyte composition as those of the previous chapter (30 wt. % hydrofluoric acid and 25 wt. % acetic acid). The wafers were purchased from Sil'tronix-ST with the following characteristics: single side polished highly-doped p-type, ($\rho = 3.5\text{--}3.68 \text{ m}\Omega\text{-cm}$) and (100) orientation. In the previous chapter, we concluded that to optimally characterize whole layers of PSi with UV-NIR ellipsometry, the thicknesses should be below 5 μm . We set the electrochemical conditions so that all the thin layers were below this value for the current study. To investigate how the anisotropy of PSi is influenced by the current density, we investigated the effect of increasing the latter under constant charge conditions. The electrochemical etching conditions are detailed in TABLE 4.1. I also investigated the PSi layers with scanning electron microscopy (SEM) to cross-check and validate the ellipsometric thickness measurements (listed in TABLE 4.1 as well).

TABLE 4.1: Electrochemical etching conditions and thickness measurement values of the investigated porous silicon layers.¹⁴

Sample notation	Current density (mA/cm ²)	Etching duration (s)	Thickness by SEM (μm)
PSi-002	2	800	2.23
PSi-004	4	400	2.04
PSi-010	10	160	1.81
PSi-020	20	80	1.67
PSi-040	40	40	1.47
PSi-100	100	16	1.19
PSi-200	200	8	0.95
PSi-300	300	5.3	0.84
PSi-400	400	4	0.75
PSi-600	600	2.7	0.72
PSi-800	800	2	0.68

4.1.2 Layers formed from silicon nanowires

The highly oriented, solid SiNWs were formed by metal-assisted chemical etching technique [100]. The parent substrate and the etching conditions were chosen in such a way that the formation of porous sidewalls is avoided. Porous SiNWs can only be formed in highly doped Si ($\rho < 10 \text{ m}\Omega\cdot\text{cm}$) and/or in presence of a sufficient concentration of oxidizing agent (e.g. H_2O_2 , cf. [101]). In the present study, we employed a low-doped, p-type ($\rho = 1.5\text{--}4 \Omega\cdot\text{cm}$), (100) oriented, single side polished Si wafer. The etching solution was composed of HF (4.8 M) and AgNO_3 (0.02 M) diluted with deionized water and no oxidizing agent was intentionally added. Similar post treatments were applied to the SiNWs as those to the PSi layers. Etching durations were set to produce SiNW lengths up to $4.1 \mu\text{m}$ with the following values: 2, 5, 10, 15 and 30 min.

¹⁴ Thickness values as a function of the applied current densities are graphically represented in Fig. 4.4a.

4.1.3 Ellipsometric measurement details

As mentioned in the introduction, pore growth is governed by the wafer crystallographic orientation and the current flow. Both favor the growth of pores normal to the surface. Therefore, as there is no preferential in-plane (xy-plane) pore formation orientation, we can consider our PSi layer as a uniaxial anisotropic layer with an optic axis parallel to the sample normal (defined as the z direction). For this kind of special anisotropy standard ellipsometric measurements are sufficient, as cross-polarization effects are nonexistent (cf. p. 221 in Ref. [3]). For arbitrarily anisotropic structures, a so called generalized ellipsometry (to determine the Jones matrix elements) or a Mueller-matrix measurement is advisable, not detailed in this study, but explanations can be found for example in Refs. [3,4,102].

I measured the PSi and SiNW samples of the present chapter by a rotating compensator Semilab SE-2000 spectroscopic ellipsometer. The recorded spectra range from deep-UV (193 nm, 6.42 eV) to near-IR (1650 nm, 0.75 eV) with 1182 measurement points, although I performed the fitting only on a reduced wavelength range because a cutoff wavelength (lower bound of the wavelength range used for the fitting, λ_{cut}) had to be applied as explained in section 4.2.2. Noise in the signal imputed to low reflected light intensities only appeared for wavelengths below ≈ 220 nm for PSi, well below the applied λ_{cut} . For the PSi samples, measurements were performed at three angles of incidence (AOIs), namely at 65, 70 and 75°. However, to increase the sensitivity to anisotropic effects in the case of SiNWs, the measurements were performed at five AOIs ranging from 55° to 75°. Micro-focusing optics was used to create a reduced illumination spot size and thus to decrease the effects of lateral non-uniformities. At the maximum AOI (75°) this resulted in a spot size of $365 \times 470 \mu\text{m}^2$. The fitting procedures of the free parameters of the simulated models were performed on α and β .

4.2 Revealing optical and structural anisotropy for porous silicon

4.2.1 Finding the appropriate effective medium based models

To model the PSi thin layers, we can utilize the anisotropic B-EMA introduced in Ch. 1 (Eq. 1.35). Therefore, for a single layer, other than layer thickness, fitting is done on the void volumetric ratio and the depolarization factor in the z direction (L_z) while fixing the other depolarization factors to $L_x = L_y = (1 - L_z)/2$. There is no need to fit the Euler angles as the optic axis is parallel to the sample normal.

We should mention some of the other possible EMTs considered for modeling as well, not introduced in Ch. 1. For example, the Landau-Lifshitz-Looyenga formula [20,103] is better suited for highly porous layers than the isotropic B-EMA because it predicts a percolation for all porosities [85], as opposed to the isotropic B-EMA which predicts a fixed percolation threshold of 1/3. The anisotropic B-EMA, on the other hand, has a percolation threshold depending on the shape of the ellipsoids (between 0 and 1/3) [21] which makes it a good choice for PSi layers with varying degree of porosity and anisotropy. More advanced generalizations of the B-EMA exist also, such as the one introduced by Bergman [104], or that of Goncharenko [105,106]. Both introduce additional parametrized functions in the B-EMA; the spectral density function or the generalized depolarization factor, respectively. They could better simulate specific systems, but the functions are difficult to relate to microtopology and morphology.

Yet still another approach relates the deviation in the ellipsometric spectra, when modeling with simple B-EMA, to quantum confinement effects of the constituent parts. It has been shown that, as the porosities increase and the average crystalline size decreases to below 5 nm, a model parametrically describing the dispersion of the dielectric function of the Si (ϵ_{Si}) is more appropriate [72–74,107]. The critical points appearing in the UV for the imaginary part of ϵ_{Si} are shifted and smeared, and the parameters describing these critical points have even

been correlated with the size of the nanocrystals [74,107]. Because these deviations appear in the UV part of the spectra (around the critical points), and because it requires many additional fit parameters that can largely cross-correlate with each other and with our previously defined fit parameters, I have chosen to only fit the measured spectra at a restricted wavelength range, that is, only above 500 nm.

To describe the whole PSi layer, I investigated three models with different layered structures. Fig. 4.1 shows the schematic representations of these models with two auxiliary SEM images of a porous area formed with low and high current density. A dendritic-like structure is revealed for PSi-004, while a highly columnar structure can be seen for PSi-800.

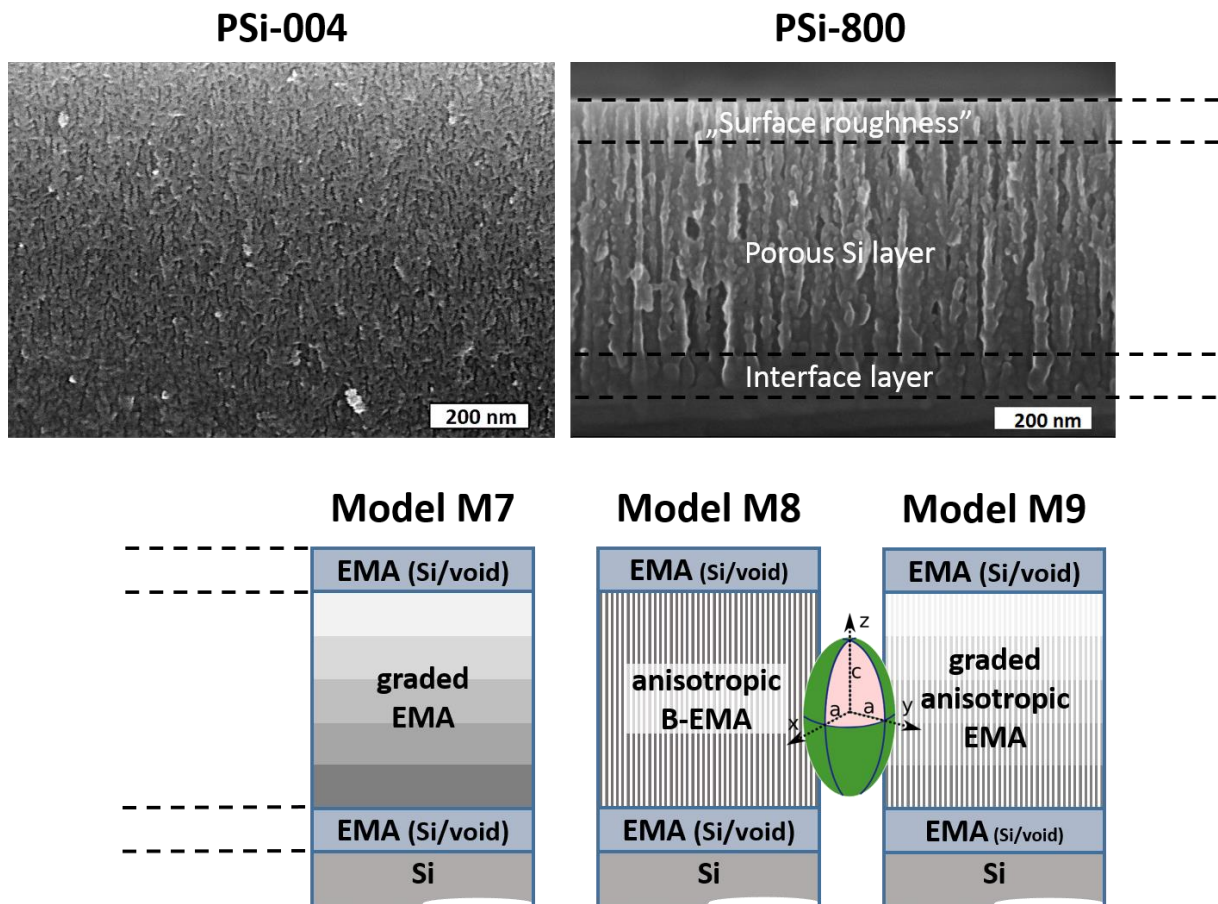


Figure 4.1: Cross-sectional SEM images (top) of sample PSi-004 showing a dendritic structure and PSi-800 revealing a highly columnar structure and the three B-EMA-based model-structures (bottom) tested for all the PSi layers. Inset is a schematic representation of the appropriate prolate spheroid for M8 and M9 where a and c are the semi-minor and semi-major axes, respectively.

Concerning the models, model M7 (continuing the labeling of the previous chapter) describes the PSi layer with an isotropic B-EMA ($L_z = 1/3$), but with a linearly varying degree of porosity as a function of the depth similarly to M3 of Ch. 3. It is best to fit the porosity of the near surface and of the Si/porous-Si interface as a separate layer. Model M7 thus has 7 independent fit parameters. Model M8, on the other hand describes the PSi layer with an anisotropic B-EMA, i.e. L_z is fitted, totaling also in 7 independent parameters. Model M9, incorporates both anisotropy and in-depth inhomogeneity in the PSi layer, with 8 independent fit parameters. I did not use M4 (or M5) of Ch. 3 (doubly-graded layer) to describe in-depth inhomogeneity, so that I could concentrate on the comparison of a graded and an anisotropic model with the same number of fit parameters. I investigated these three optical models on all the PSi samples, and compared them based on their fitted *RMSE* values.

To demonstrate the sensitivity to anisotropic effects, I present the fitted Ψ and Δ spectra on PSi-200 with M7 (*RMSE* = 29.8) along with a simulation of an isotropic simulation with the same thickness and porosity values in Fig. 4.2. We can see a significant difference between the spectra even though the only difference is the fitted $L_z = 0.237$ ($\Delta n = -0.291$) compared to the isotropic case of $L_z = 1/3$. By considering the sensitivity to Ψ and Δ , we can thus estimate a sensitivity to L_z as being ~ 0.001 .

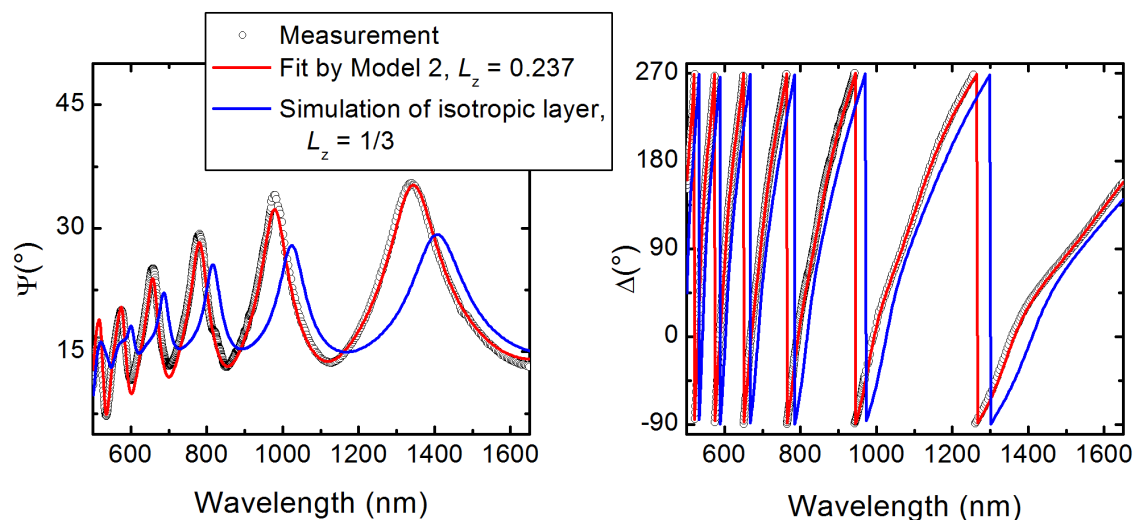


Figure 4.2: Sensitivity to anisotropic effects demonstrated on sample PSi-200. Between the fitted Model M8 and the simulation, only the depolarization factor differs.

4.2.2 Characterization results

The *RMSE* values obtained from the fit of the three model structures on the PSi samples as shown in Fig. 4.3, clearly indicate two separate PSi behaviors. At first, I compared the two main models (graded and anisotropic). For the PSi layers formed by low current densities (<100 mA/cm²) M7 fits the ellipsometric values much better (lower *RMSE*) than M8, so it can be concluded that the dominant optical effect for these samples is the in-depth (or vertical) porosity inhomogeneity rather than the pore anisotropy similarly to the results of Ch.3. On the other hand, for the PSi layers formed by high current densities (>100 mA/cm²) it is the opposite case; M8 fits much better than M7, meaning that the dominant optical effect for these samples is anisotropy (M7 yields completely off the chart fits for the most anisotropic cases). In a recent study, a similar model based separation as a function of the current density has shown these two separate optical behaviors as well [78]. Model M9 (graded anisotropic) is a mix of the two aforementioned models and thus takes advantage of those two to accomplish similar or even slightly lower *RMSE* on every characterized PSi sample. This result points out that either

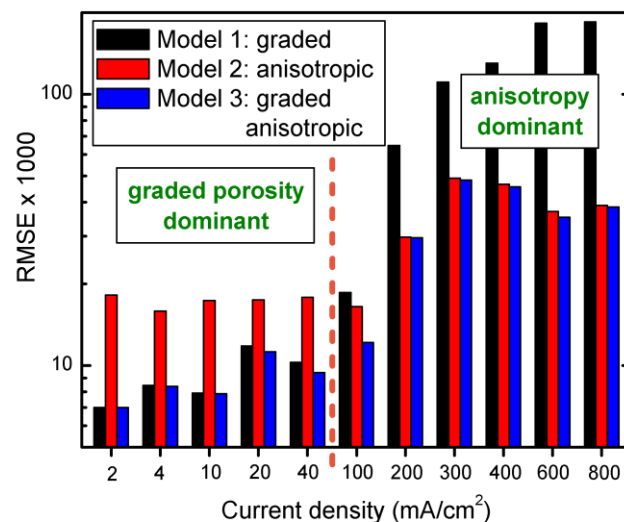


Figure 4.3: Columnar plot of *RMSE* values of the three model structures tested on the PSi layers. *RMSE* values indicate that vertical inhomogeneity for the PSi layers formed with lower current densities and anisotropy for the PSi layers with higher current densities is the dominant effect.

in-depth grading or anisotropy dominates in both thickness regions. The second most important point to note from Fig. 4.3, is that the *RMSE* values are larger when the applied current densities are above 100 mA/cm². This could be partly explained by the fact that α and β run across larger bounds across the spectra for these samples (almost from -1 to 1 for all the AOI) compared to those of the inhomogeneity dominant samples. I also extrapolated the fitted spectra from M9 down to 230 nm (without a re-fitting of the parameters) to highlight the deviations around the critical points of Si. Then, the comparison of the *RMSE* values indicates that deviations are small for low porosities but become very large for high porosities (*RMSE* > 100 for P*Si*-600 and P*Si*-800). These differences are probably due to the size effect of the nanocrystals [74,107], not accounted for in our models.

Figures 4.4 summarize the important results obtained for the P*Si* samples. Displayed thickness values are the total of the porous, interface and surface roughness layer thicknesses, while porosities, L_z and the derived Δn values are the weighted averages of the sublayer thicknesses. I compared the thickness values acquired by the analyses of SEM images with those obtained by SE fitting using M9. They are in excellent agreement with each other, showing an almost linear decrease with logarithmically increasing current density as it would be expected from P*Si* layer formation under constant charge conditions [87]. As expected, porosities increase, from $\approx 30\%$ to $\approx 72\%$ following a quadratic-like curve as a function of the logarithm of current density (cf. pp. 19–22 in Ref. [108] and [109]). The error bars of the thickness and porosity values represented are the standard deviations from fits that I performed on spectra measured at different locations on the sample. The right figure of Fig. 4.4 shows the L_z and Δn values as a function of current density (but not its logarithm to focus on the anisotropy dominant part). For completeness, TABLE 4.2 lists all the n and k values as well. The optical constants of TABLE 4.2 and Δn represented in Fig. 4.4 are taken at a wavelength of 632.8 nm. Because the surface and interface roughness layers are considered as isotropic, the average anisotropic values are slightly smaller than that of the fitted values of the

middle, graded-anisotropic B-EMA sublayer of M9. The prolate spheroid aspect ratio (c/a) calculated from Eq. 1.38 is also shown for some of the samples. Anisotropies are very high for the samples formed by the highest current densities as anticipated, but what is unexpected is that there is a peak at a current density of 400 mA/cm². This could be probably explained by the fact that at this current density sidewall smoothness attains its maximum. Beyond it, as the porous layer thickness decreases, the interface and surface roughness effects become more pronounced diminishing the anisotropy of the whole structure.

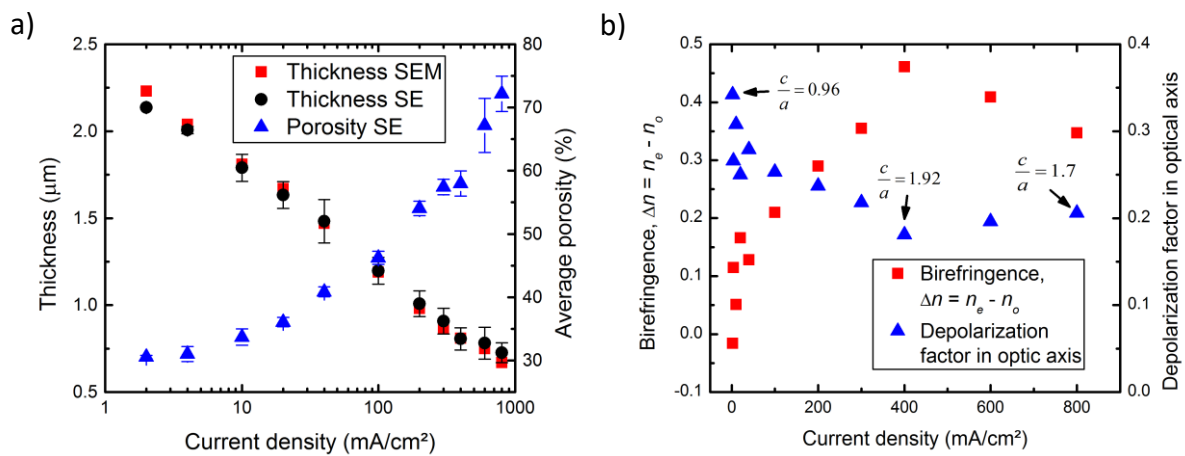


Figure 4.4: Semi-log plot of thickness values measured by SEM and average thickness values and porosities from fitted SE spectra as a function of the current densities applied for the PSi layer formations. Average values are from fits performed on spectra measured at different spots on the sample, while error bars are the standard deviations of these lateral inhomogeneities (a). Fitted depolarization factors in the z direction and derived birefringences (from ϵ^z_{eff} and ϵ^{xy}_{eff}) as a function of the current densities applied for the PSi layer formations. The refractive index as well as the birefringence values have been taken at a wavelength of 632.8 nm. Prolate spheroid aspect ratios are also shown for some of the samples (b).

TABLE 4.2: Optical constants of the ordinary and extraordinary directions taken at a wavelength of 632.8 nm

Sample notation	n_o	n_e	k_o	k_e
PSi-002	3.016	3.000	0.0105	0.0104
PSi-004	2.984	3.099	0.0103	0.0110
PSi-010	2.877	2.930	0.0097	0.0101
PSi-020	2.815	2.981	0.0093	0.0104
PSi-040	2.663	2.791	0.0085	0.0094
PSi-100	2.453	2.663	0.0073	0.0088
PSi-200	2.109	2.399	0.0051	0.0074
PSi-300	1.984	2.340	0.0043	0.0071
PSi-400	1.930	2.391	0.0039	0.0075
PSi-600	1.664	2.073	0.0023	0.0057
PSi-800	1.530	1.877	0.0016	0.0044

We should mention some of the potential applications of these high anisotropies. Anisotropic properties have important implications for the fabrication of optical elements. Indeed, the morphology induced anisotropies can attain much higher values than those of typical intrinsic (bulk crystal) anisotropies [18,69]. The easily tunable properties of porous PSi layers (pp. 201–206 in Ref. [54]) make it an excellent candidate for birefringence and dichroism based optical elements, like retarders [110] or polarization-sensitive Bragg-reflectors [111–113].

4.3 Characterization of silicon nanowires

4.3.1 Extension of Maxwell-Garnet model to the nanowires

Some studies have already shown the (limited) applicability of EMTs to similar structures as our SiNW layers (Si nanorods [114], bunched SiNW arrays [115]). The oriented nanowires of our study form in fact layers exhibiting such a high uniaxial anisotropy along the z-axis (see Fig. 4.5a), that no multi-parametrized isotropic model (with in-depth gradient of porosity) could

well describe. To account for this high anisotropy, I tested both Bruggeman and Maxwell-Garnett anisotropic EMTs. However, I decided to adopt the generalized Maxwell-Garnett EMT (MG-EMA, cf. Eq. 1.33a and b), as it is better for modeling the nanowired layers, because the high void content can represent ϵ_{host} and the SiNWs the incorporating material. Additionally, the MG-EMA models systems without a percolation threshold as opposed to the B-EMA, which would seem a better representation of the non-connected nature of the nanowire formation.

Fig. 4.5b shows the model used for the SiNWs (M10). To model the possible collapse and bundling of the nanowires, several independently fitted anisotropic (sub-)layers were used. The model development consisted in the iterative addition and fitting of increasing number of sublayers until either the *RMSE* decreases with relatively small values or the parameter errors or CCs become too large. By default, the MG-EMA was used as the mixing rule except for the interface roughness layer and when the MG-EMA displayed a Si content larger than 30% for a specific sublayer, then modeled with a B-EMA instead.

For the PSi samples, I used for the fitting only the part of the spectra above 500 nm, to avoid complications due to nanocrystallite size effects, and as such EMTs are largely applicable because the typical pore dimensions remain less than 50 nm. On the other hand, for the SiNWs, special care must be taken as the nanowires can have diameters between 30 and 100 nm and they also tend to collapse and form larger bundled groups. To maintain the applicability of the EMT only a limited part of the spectra can be used for fitting. I applied a thickness dependent cutoff wavelength (λ_{cut}).

A warning sign also appears from the color of the samples. The sample etched for 10 min has a brown, while the ones etched for 15 and 30 min have a black diffuse color meaning that there is a high scattering and absorption in the visible wavelength range. This behavior is not surprising as SiNWs have already been studied as antireflective layer for photovoltaic applications [116]. The spectra have also very little ellipsometric information in the visible wavelength range for these samples as illustrated in Fig. 4.5c.

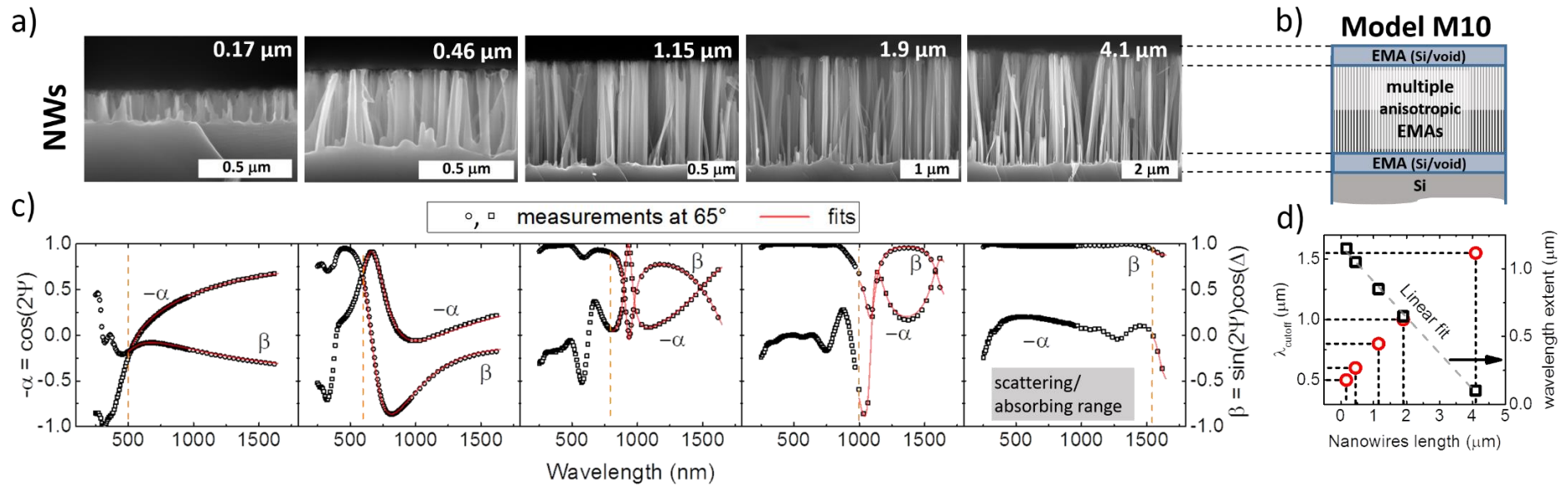


Figure 4.5: Cross-sectional SEM images of the SiNWs (a), EMT based model-structure (b), α and β measured and fitted ellipsometric values at an AOI of 65° (c), and plotted cutoff wavelength (λ_{cut}) and wavelength extent used for the fitting as a function of the nanowires length (d).

It is challenging to justify in an entirely accurate way where λ_{cut} for the fitting should be set at. For the anisotropic MG-EMA, I assumed a similar limitation to that of the B-EMA (cf. Ch. 1.6.5). Bundling of the nanowires causes the EMT models to fail because of scattering effects at wavelengths larger than that which would be caused by well separated nanowires. A more or less intuitive manner to determine λ_{cut} was to select a sufficiently large part of the upper spectra and decrease step by step the lower limit by evaluating how the *RMSE* increases (fit quality worsens). λ_{cut} was chosen before large deviations start to occur between measured and fitted ellipsometric values. A different λ_{cut} was applied to the different spectra belonging to the SiNWs. Fig. 4.5d represents this λ_{cut} with the appropriate wavelength extent (i.e. bandwidth used for the fitting in nm) as a function of the measured layer thickness. There seems to be a linear correlation, suggesting that the typical (lateral) dimension of the bundles increase with the nanowires length.

Here, let me mention some of the previous works done by myself and my group at MFA not detailed in this thesis. We applied a similar λ_{cut} for the SE characterization of monolayers build up from silica nanospheres [O15] and in another study to periodic (with long range spatial correlation) electron-lithographed holes in polymethyl methacrylate photoresist on c-Si [O10]. We also found strong correlations between the typical feature sizes (silica diameter, hole diameter, hole periodicity) and the λ_{cut} .

4.3.2 Characterization results

The measured thickness and porosity values are summarized in Fig. 4.6a. Thickness by SE agrees well with that obtained from SEM image analyses. Additionally, fitted porosities are relatively high with a decreasing value as a function of the layer thickness. Anisotropy results can be seen in Fig. 4.6b. The represented n and Δn values are the result of two averaging. First, the spectral mean is taken for each EML and then the thickness weighted averages of these sublayer mean values are calculated. Of course, with the EMT formulas (after fitting the porosities and depolarization factors), it is possible to extrapolate n to any wavelength.

c/a calculated from Eq. 1.38 is also shown for the lowest fitted L_z obtained for the sample etched for 10 min (1.1 μm thick). This c/a is close to the real aspect ratio of a typical nanowire for this sample seen by SEM as the nanowires diameter range from 50 to 100 nm, indicating that the SiNWs are well oriented, without any or few collapsed to bundles. For the two thinnest samples, anisotropy is smaller, but with a high void volume ratio because at these stages random nucleation of the SiNWs has just started with a high Si dissolution. The preferential orientation of the SiNWs etched 10 and 15 minutes presents an even higher structural anisotropy than those of PSi layers paving the way to photonic devices [99].

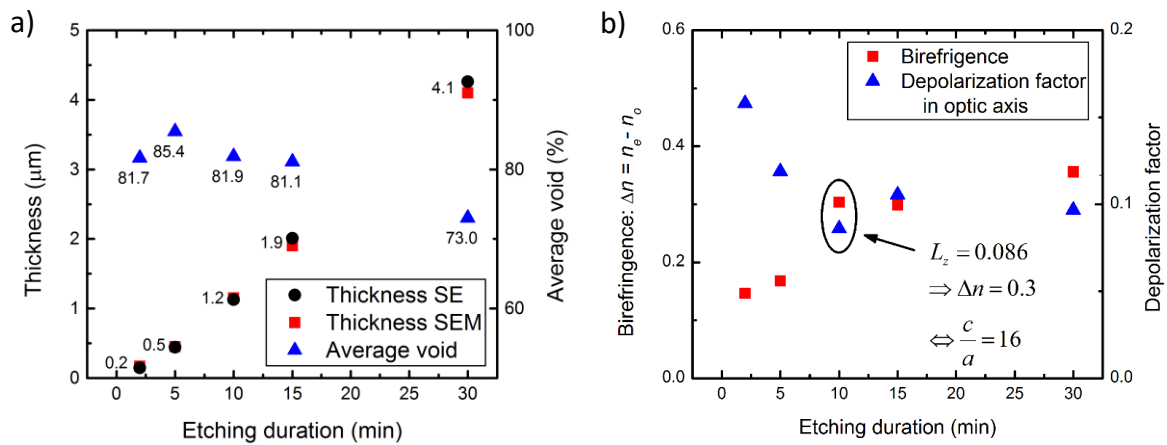


Figure 4.6: (a) Thickness values measured by SEM and thickness values and average void volume ratios from fitted SE spectra as a function of the etching durations of the SiNWs. Average void ratios are calculated from the thickness weighted void volume ratios of the B-EMA sublayers. (b) Fitted depolarization factors in the z direction and derived birefringences (from ε_{eff}^z and ε_{eff}^{xy}) as a function of the etching durations of the SiNWs. Prolate spheroid aspect ratio is also shown for the lowest fitted depolarization factor obtained for the sample etched for 10 min (1.1 μm thick).

It is important to note, that the very short wavelength range for the thickest sample where EMT could be applied (1550–1650 nm, cf. Fig. 4.5c and d), makes the fitted results questionable at best. For future SiNW characterizations with SE modeled by EML, we suggest applying a similar cutoff wavelength depending on the SiNW length and the spectral range of the ellipsometer. Characterization of SiNWs is thus not only handicapped by scattering as it

greatly limits the gathered specularly reflected light, but also by the models used for the evaluations. In the following, last chapter however, I will show the applicability of finite element modeling to ellipsometry of Si roughness; similar simulations could possibly extend the characterizable wavelength range to the scattering regime for nanowires as well. In our case of visible-near-IR SE measurements and EMT based evaluations though, light scattering induced by the collapse of the nanowires permitted a characterization up to a layer thickness of around 4 μm . To effectively evaluate with EMT models beyond this limit, we suggest the use of mid-IR spectroscopy, preferentially IR ellipsometry.

4.4 Conclusions

In this chapter, I showed the characterization of columnar PSi and SiNW. I followed a similar approach for the development of the optical models for the two types of samples focusing on the anisotropic features. Generalized Bruggeman and Maxwell-Garnett EMTs were used to describe the samples as stacked multi-layers. SE characterization revealed that anisotropy increases as a function of the applied current during the etching process of PSi layers, but for low current densities (below 100 mA/cm^2 in the current conditions), isotropic effective medium models with in-depth inhomogeneities describe sufficiently the samples. For current densities larger than 100 mA/cm^2 , anisotropy becomes a dominant factor when characterizing the ellipsometric spectra (additionally to the mean porosities and layer thicknesses). SiNW evaluations revealed that the layers are highly anisotropic as well, but derived prolate spheroid aspect ratios showed that the best ordered orientation is obtained for the sample formed of ≈ 1 μm nanowires. For the thicker layers, the long nanowires start to collapse into bundled states, decreasing the anisotropy. Finally, EMT-based SiNW evaluations of visible-near-IR ellipsometric measurements is limited because of light scattering, in our case, to around 4 μm .

5 Simulation of microscopic surface roughness

In chapters 3 and 4, I introduced an effective medium model to describe the surface roughness of the different silicon based materials. In fact, characterizing surface roughness with ellipsometry has become a routine practice since the birth of SE because of its fast, non-destructive and in-line capabilities. At the beginning of SE some studies have already shown that neglecting the surface roughness in the optical model system may largely bias the ellipsometric measurements and thus the evaluation of the optical constants [117,118]. For example, for the correct determination of the dielectric functions of a bulk material, the surface roughness has to be taken into account [119]. The determination of the optical constants is of high interest in solar cell materials, especially the bandgap energy that is proportional to the voltage output, and neglecting the surface roughness in the ellipsometric models biases the fitted results [120]. The most widely used models describe the surface roughness with an effective dielectric function mixed from the dielectric functions of the two media separating the rough interface. Such simplification, similarly for all effective medium theory-based models, is valid only when the typical feature sizes of the roughness are much smaller than the wavelength of illumination, i.e. the system is in the quasi-static regime.

The important question that remains open is how the surface morphology and the effective medium layer (EML) roughness correlate? An excellent summary about this relationship can be found in the book chapter of Yanquas-Gil and Wormeester [121], of which some will be mentioned in this chapter. Usually, maps of microscopic surface topology can be obtained by scanning probe microscopy technique such as atomic-force microscopy (AFM). In fact, many experimental comparisons have been made between the EML thickness measured by ellipsometry and the morphology measured by AFM for different Si samples: wet etched and thermally annealed Si [122], CVD deposited poly-Si [77,123] and poly-Si-on-oxide [124], as well

as for *in situ* growth of amorphous hydrogenated Si [125] and CVD deposited microcrystalline-Si on amorphous Si [126]. These works all concluded at a positive linear relationship between EML roughness and AFM root-mean-square height, but all with different linear parameter values (slope and offset). One study even showed a negative correlation [127], stating that AFM measurements indicate an increase in root-mean-square height while ellipsometry suggests a smoothing of roughness. To better grasp the kaleidoscope of these different results, in this chapter the simulations of ellipsometric response of a large number of random Si surfaces with well-defined root-mean-square heights and lateral correlation lengths will be presented and the results discussed [T2]. I made the numerical simulations by finite element method (FEM). I considered the ellipsometric simulations of the random rough surfaces in our case as the “measured” samples and the effective medium roughness as the model to be fitted. This approach reveals many interesting effects concerning the relationship between the surface morphology and the thickness of the EML.

5.1 Simulation details

5.1.1 Stochastic surface generation

A simple description of the surface topology is to assign a unique height distribution function to it. Although this simplification disregards overhangs and porosities, it remains a good approximation for many experimental systems. From the height distribution function many scalar quantities can be defined, but I will focus on the two most commonly used parameters, the root-mean-square height (R_{RMS}) and the lateral correlation length (ξ).

I generated the topographic points of the surface with D. Bergström’s Open Source MATLAB code [128] in such a way that the height distribution followed a Gaussian statistics. I concentrated only on 1-dimensional surface roughness to drastically diminish computational costs. For visualization, a portion of the simulation mesh of a surface with a ξ of 10 nm and a R_{RMS} of 2.5 nm is shown in Fig. 5.1a (left) with the height distribution histogram (right). An easy

way to achieve such a height distribution is to convolute a predefined Gaussian filter on an uncorrelated (Gaussian) distribution of surface points generated by random numbers (i.e. white noise) [129]. The advantage of this approach is that the standard deviation of the uncorrelated distribution and of the Gaussian filter will be inherited, and account for the R_{RMS} and the ξ of the surface, respectively. Of course, due to the stochastic nature of the structure, small deviations will be present between the predefined standard deviations and the R_{RMS} values. To achieve adequate Gaussian statistics and diminish deviations from nominal values, the characteristic length scale of the surface to be simulated (L) was chosen such that $L/\xi \geq 500$. Additionally, L was at least $5 \mu\text{m}$ so that diffraction due to periodic boundary conditions would be negligible. The number of generated random points was set in a way that the Nyquist sampling criterion would be largely fulfilled; $> 2L/\xi$. The simulated topographical parameters for ξ were 2.5, 5, 10 and 20 nm, while for the R_{RMS} were 0.5, 1, 1.5, 2.5, 3.5, 5, 7.5, 10, 15 and 20 nm (see TABLE 5.1). The combinations of all these parameter values are simulated, totaling in 40 points.

TABLE 5.1: Topographical parameters used for the simulations.

Root-mean-square roughness, R_{RMS} (nm)	0.5	1	1.5	2.5	3.5	5	7.5	10	15	20
Correlation length, ξ (nm)	2.5		5			10		20		
Length scale, L (μm)	5			10			20			

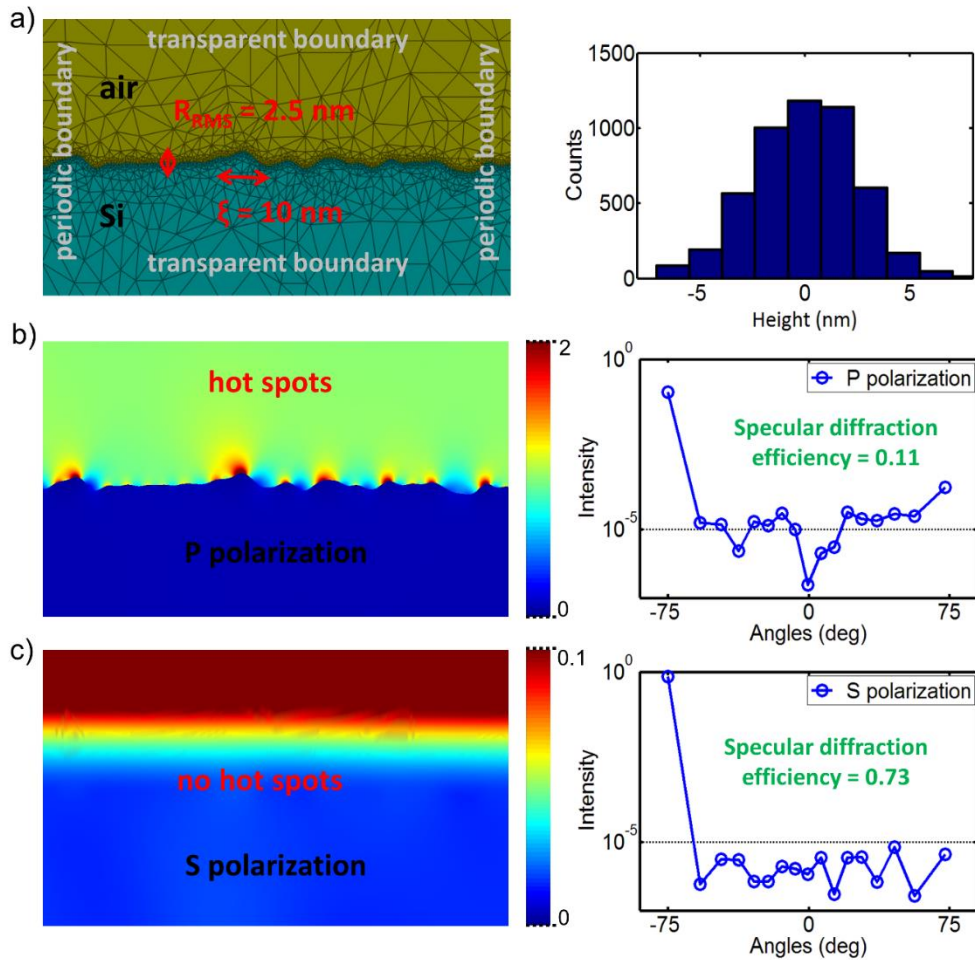


Figure 5.1: Scattering simulation of one of the generated surface roughness for a plane wave incident at 75° at a wavelength of 600 nm. (a) Local grid structure after one refinement step (left) and the Gaussian distribution of surface heights (right). Near field intensity image and far field intensity angular distribution for (b) p polarization and (c) for s polarization (with -75° meaning the specular reflection).

5.1.2 Finite element method details

I simulated the electromagnetic near fields resulting from the plane wave illumination of silicon surfaces with different roughness using the finite element solver JCMSuite (version 2.16). Specular reflection amplitudes (and intensities) were obtained from far field results computed in post-process as a spatial (discrete) Fourier spectrum. Although the Maxwell equations are solved as stationary wave solutions in frequency domain, from the complex scattered electric fields both the amplitude and phase information can be obtained. As the

electric fields of the incident plane waves polarized parallel (p) and perpendicular (s) to the plane of incidence in our finite element simulations are defined with unit amplitudes, the ellipsometric complex ρ is obtained as the ratio of the reflected complex amplitudes of the p and s polarizations. The spectra were simulated in a wavelength range from 200 to 1000 nm, in steps of 10 nm, for AOI of 65° and 75°. The near-field amplitudes had to be computed individually for each wave vector of the illumination, because of the optical dispersion of the Si material [39].

For computational reduction, I choose the simulation domain to be 2-dimensional, with a translational symmetry in the direction perpendicular to the plane of incidence. This very useful simplification is based on the assumption that cross-polarizations due to the anisotropic nature of the simulated surface (as opposed to a real randomly rough 2D surface) are negligible, as the surface features are much smaller than the wavelength of illumination. Furthermore, to eliminate scattering-like artifacts at the edge of the surface, periodic boundary conditions were used at these lateral sides of the computational domain. For the two remaining sides, transparent boundary condition was applied.

JCMSuite permits adaptive mesh refinement, i.e., after a pre-generated grid (following the curvature of the geometry), local grid refinements are applied as a function of the previously solved field amplitude gradients and a new refined mesh is calculated. These steps can be iterated to achieve adequate convergence and necessary precision. Faster convergences can be achieved when using higher FEM degrees. In my simulations, computational costs and ellipsometric angle convergences as a function of the refinement steps and the FEM degree were also investigated for optimization purposes. Fig. 5.2 summarizes the ψ and Δ convergences for a typical surface roughness but with L of only 2 μm . The differences presented are the average of the differences at 5 simulation wavelengths between 200 and 600 nm. These are 5 points around the middle and near UV critical points in the ϵ_2 of the monocrystalline Si used for the simulations. Near field gradients can be much higher around boundary interfaces

where the dielectric function contrasts of the two bulk materials are higher, and so convergences are more sensitive to local mesh refinements and FEM degrees. I considered that an adequate convergence had been attained when the Ψ and Δ differences between the last and the previous step was less than 0.1° . Computation costs are shown in Fig. 5.3. The computation times were achieved by an Intel Core i5-3230M CPU with a core frequency of 2.6 GHz. Simulation unknowns are related to the number of mesh vertices and they are responsible for the quantity of memory consumption. For the investigated morphologies (ξ and R_{RMS} are smaller than λ), a suitable compromise for computation costs was 1 refinement step and a FEM degree of 3, with which a Ψ convergence smaller than 10^{-2} and a Δ convergence smaller than 10^{-1} degree were achieved. At these system options, processing one wavelength at one AOI took ~ 12 s (~ 30 min for two spectra having 80 wavelengths at 2 AOI) and resulted in 130 000 model unknowns consuming a peak memory of around 1 GB.

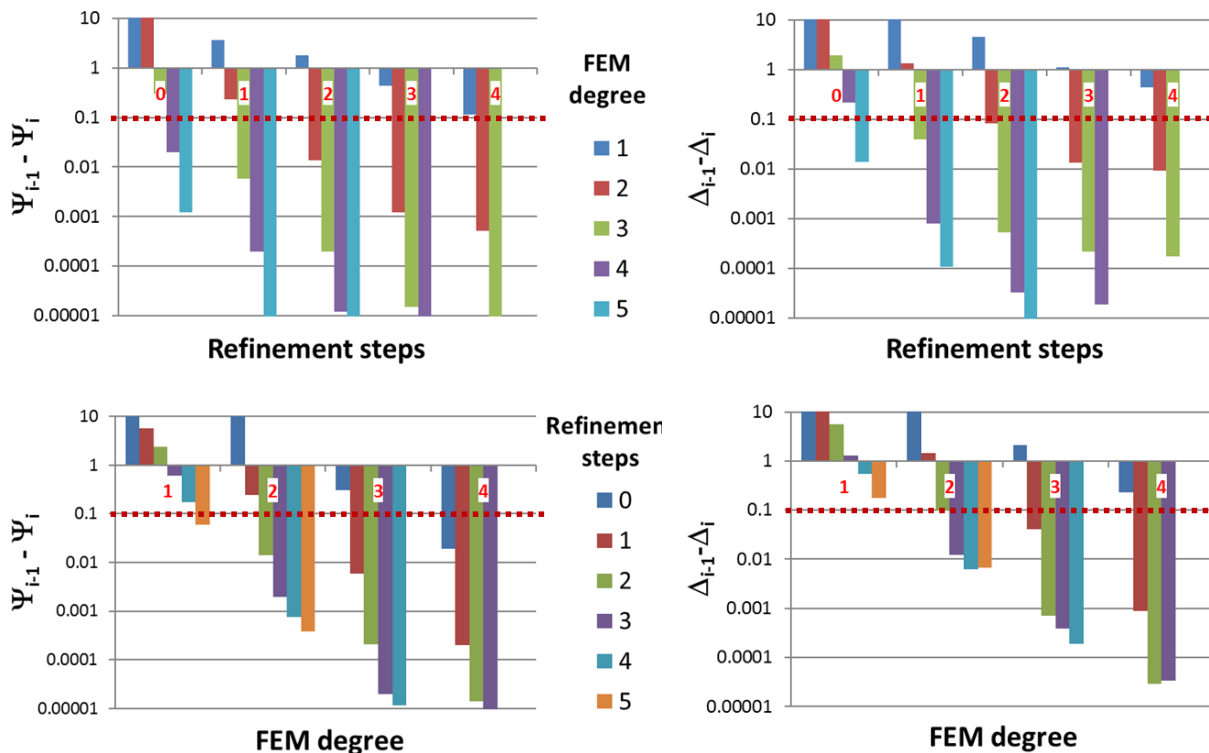


Figure 5.2: Ψ (top and bottom left) and Δ (top and bottom right) convergences as a function of the automated mesh refinement steps (top left and right) and FEM degrees (bottom left and right) set for the simulations. The 'i' index represents the last convergence step for the number of refinement steps or for the FEM degree.

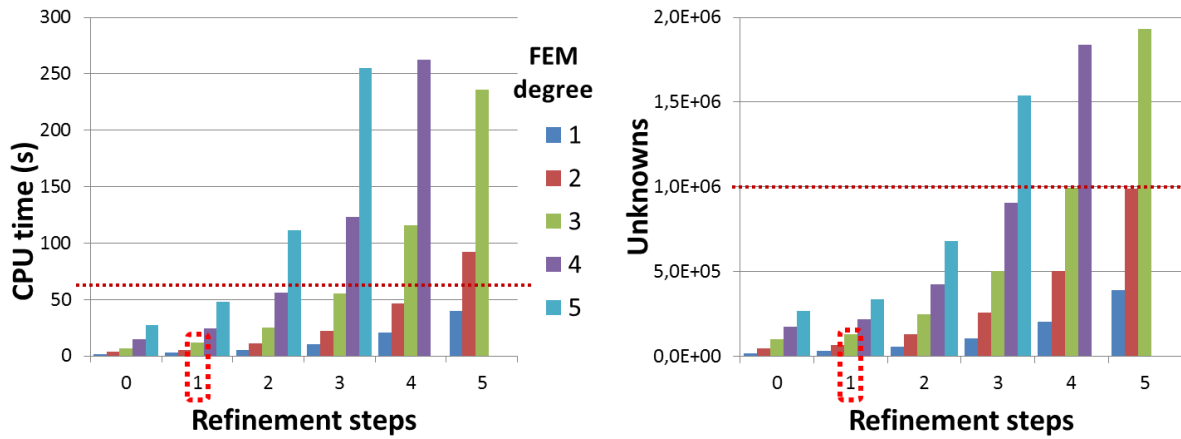


Figure 5.3: Computational time (left) and model unknowns (right) as a function of the number of refinement steps and FEM degree set for the simulation of a typical surface roughness.

5.1.3 Effective medium layer details

I fitted the FEM simulated spectra with a planar thin layer structure using TMM, where the surface roughness is considered to be an effective medium volumetrically composed of 50–50% of the two media (cf. pp. 181–184 in Ref. [3]). D. E. Aspnes et al. concluded that the Bruggeman type effective medium approximation (B-EMA) showed the best fit results for the ellipsometric evaluations of various rough surfaces [130], and has been extensively used for such evaluations since then, so we will also focus on B-EMA. The simplest single layer B-EMA representing the surface roughness has only one fit parameter, namely its thickness value (d_{EMA}). A depiction of how the B-EMA relates to the surface roughness can be seen in Fig. 5.4. The surface roughness was simulated in a void ambient, that is an excellent approximation to model air ambient as well for ellipsometry, so the effective refractive index (n_{eff}) is a function of only the refractive index of Si ($n_{\text{Si}}(\lambda)$). The void is kept fixed at 50% as mentioned above, as the screening parameter as well, kept fixed at a value of 1/3, representing spherical inclusions in the B-EMA model. The introduced intermediate layer has a d_{EMA} that is some measure of the

average height variation. The $RMSE$ in our case (from Eq. 1.26), for one fitted parameter, shall take the following form:

$$RMSE = \sqrt{\frac{1}{J-2} \sum_{j=1}^J \left\{ (\Psi_j^{FEM} - \Psi_j^{EMA})^2 + (\Delta_j^{FEM} - \Delta_j^{EMA})^2 \right\}}, \quad (5.1)$$

where the superscripts 'FEM' and 'EMA' of Ψ and Δ indicate the FEM simulation values and the fitted B-EMA based values respectively.

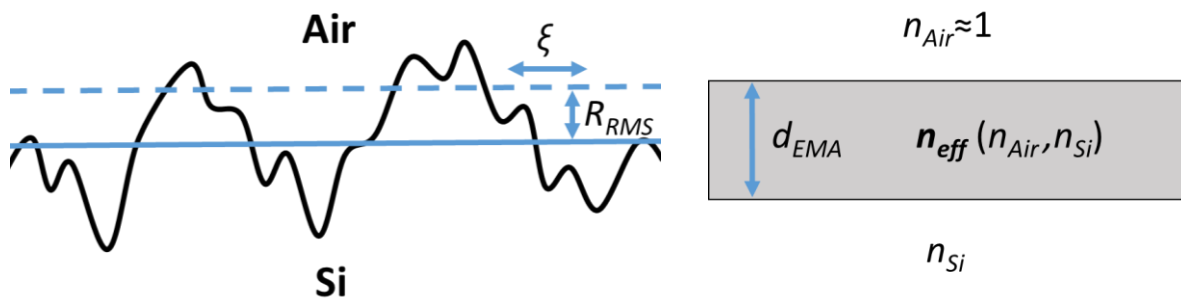


Figure 5.4: Schematic depiction of a microsurface roughness profile of Si in air ambient (left) and a corresponding three-phase model structure based on effective medium approximation (right).

5.2 Comparison of effective medium approximation and finite element method results

5.2.1 Limitations of the simulations

The small surface features cause high intensity spots in the near field around the sharp features of surface protrusions for the p polarization, which are not present for the s polarization (see left images of Figs. 5.1b and c, respectively, for plane wave illumination at an angle of incidence of 75° , and a wavelength of 600 nm). The difference for the two polarizations is clearly accountable in the diffracted far field intensity values as well. The right-hand side images of Figs. 5.1b and c show the angular intensity distributions of the two polarizations. Although the ellipsometric angles were calculated solely from the 0th order (specular) diffracted amplitudes, it is interesting to note that apart from the specular intensity differences

(diffraction efficiency of 0.11 for p polarization and 0.73 for s polarization), there is generally an order of magnitude difference in the higher order diffracted angles between the two polarizations. For cases where λ is much larger than the typical feature size of the surface roughness, non-specular scattering would be negligible for ellipsometric considerations and also B-EMA models are applicable. At wavelengths comparable to the typical feature size, scattering starts to dominate and B-EMA clearly fails to describe the roughness. To demonstrate this phenomenon, Fig. 5.5 shows the B-EMA-fitted spectra on simulations with an increasing R_{RMS} value ($R_{\text{RMS}} = 1, 5$ and 10 nm for Figs. 5.5a, b and c, respectively) for an identical $\xi = 10$ nm. For the $R_{\text{RMS}} = 1$ nm ($d_{\text{EMA}} = 0.3$ nm), an almost perfect match can be fitted, while for the $R_{\text{RMS}} = 5$ nm case ($d_{\text{EMA}} = 6.7$ nm), small deviations at the UV part of the spectra start to appear with an increase in the *RMSE* value. Finally, for the $R_{\text{RMS}} = 10$ nm case ($d_{\text{EMA}} = 24$ nm), fitting on the whole spectra would be inappropriate, biasing the evaluated roughness. The fit example shown in Fig. 5.5c was made in a wavelength range of 800–1000 nm only (*RMSE* = 1.0), and the ψ and Δ angles were generated (extrapolated) to the whole range to point out the huge deviations from the FEM simulations below $\lambda = 600$ nm. These deviations are more pronounced than what would be expected in case of a real measurement fitted with B-EMA models at these R_{RMS} values. The difference is probably because of the simplification of using 2D models. Here I should mention that 3D simulations are mainly constrained by hardware capabilities. The number of unknowns of the simulation problem and thus the memory consumption scales as a power of 1.5. For example, a 1D surface roughness consuming 1 GB of memory would need around 300 GB of memory for its 2D counterpart. With domain decompositions this amount could be reduced but then it would greatly increase the computational time required (orders of magnitude), and so probably parallel grid computation should be used.

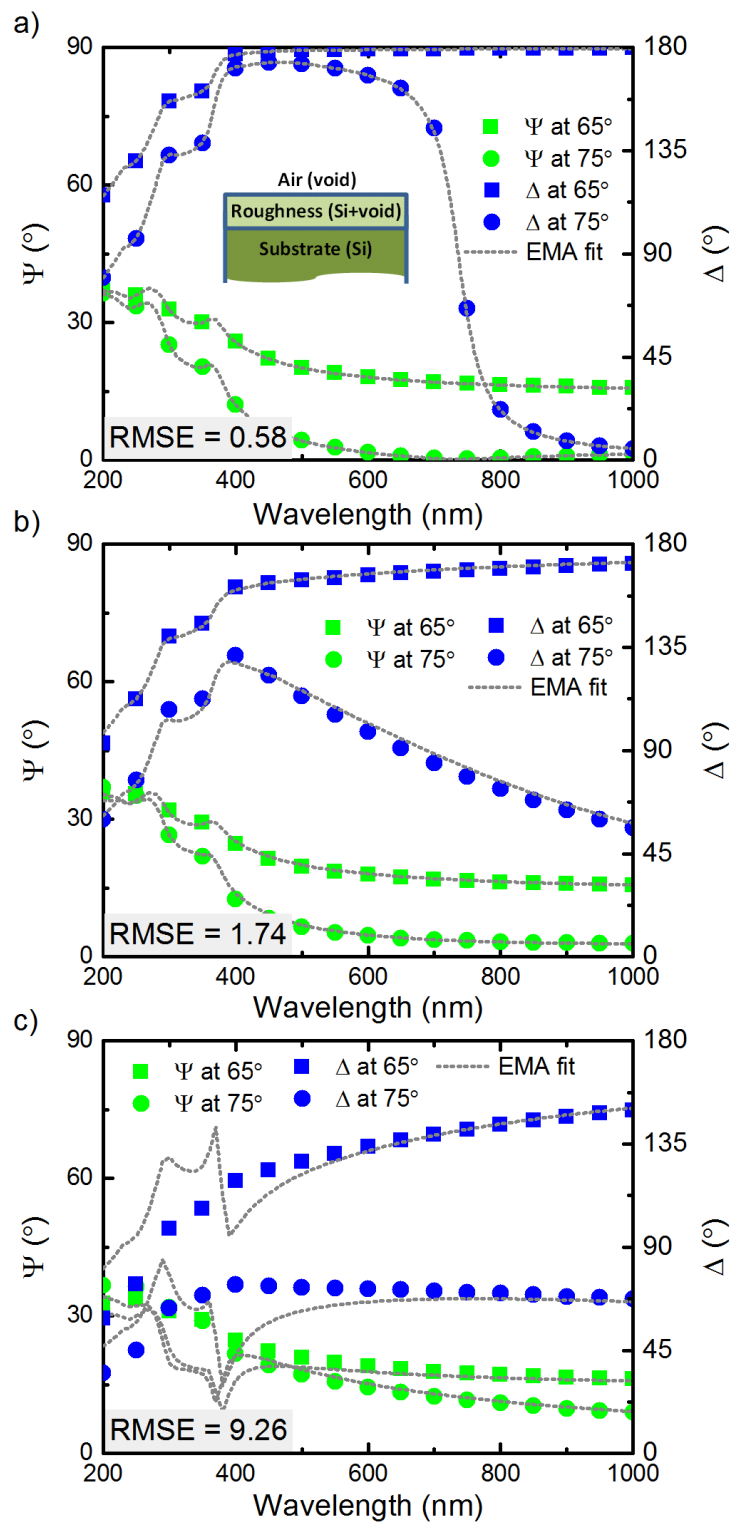


Figure 5.5: FEM simulations of Ψ and Δ spectra fitted with a B-EMA surface roughness (see the model inset) of the samples with a nominal correlation length (ξ) of 10 nm and with a nominal root-mean-square roughness of (a) 1 nm, (b) 5 nm and (c) 10 nm. Root-mean-square errors (RMSE) are also included in the graphs.

5.2.2 Quadratic relation between root-mean-square roughness and effective medium thickness

For the following discussion, only the simulations where the whole spectral range can be fitted with the B-EMA model ($RMSE < 3$) are considered. Fig. 5.6 summarizes the dependence of d_{EMA} on the R_{RMS} and ξ values. The most conspicuous effect is that separate relations can be established between the d_{EMA} and the R_{RMS} , depending on ξ . Interestingly, quadratic relation fits are much more accurate than simple linear ones at these parameter ranges. Additionally, the different “curvatures” indicate that ellipsometry is more sensitive to sharper surface roughness features in the microscopic regime, i.e., for shorter ξ values, fitted d_{EMA} increases at a higher pace as a function of R_{RMS} than for longer ξ values. This effect agrees well with the conclusion made in Ref. [127] that ellipsometry is sensitive on roughness only on relatively short length scales, also demonstrated by 2 linear fits with different slopes in Ref. [122]. In other words, the high-wavenumber contributions of the power spectral density of the surface points dominate the polarization change.

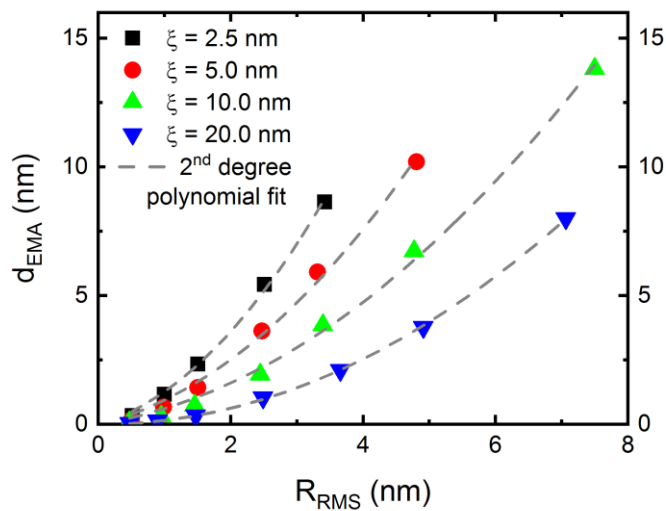


Figure 5.6: 2nd degree polynomial correlation between the root-mean-square roughness (R_{RMS}) and the thickness of the effective medium roughness (d_{EMA}) for different correlation lengths (ξ).

5.2.3 Revealing another correlation

The quadratic relation between d_{EMA} and R_{RMS} was also shown to exist in Ref. [131], where the change in polarization due to the interaction of light with the microscopically rough surface was calculated by second-order Rayleigh-Rice formalism (developed by Franta and Ohlidal [132]) and fitted to the B-EMA calculations. Furthermore, Yanguas-Gil et al. [133] calculated a small correlation length approximation of the Rayleigh-Rice theory for self-affine surfaces. Such surfaces have R_{RMS} values that scale as L^α , where α is the roughness exponent, an additional characteristic parameter originating from the dynamics of roughness growth. In the calculations, a $d_{\text{EMA}} \sim R_{\text{RMS}}^2/\xi^\alpha$ relationship was proven. Similarly to the interpretation done in Ref. [133], that the average surface slope (R_{dq} , root-mean-square average of the local slope, see Ref. [134]) scales as $R_{\text{RMS}}/\xi^\alpha$, the d_{EMA} value can be plotted as a function of the product of this R_{dq} and the R_{RMS} value. Fig. 5.7 reveals a linear correlation for the present study. Excellent linear fit is achieved for $R_{\text{RMS}} \cdot R_{\text{dq}}$ values smaller than 2 nm. For larger values, downward deviations from the extrapolated line appear, hinting at higher order corrections in the

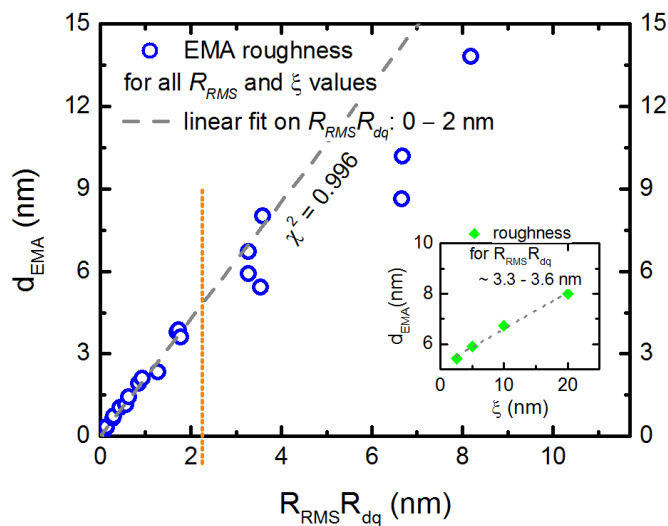


Figure 5.7: Correlation between the product of RMS roughness and RMS slope ($R_{\text{RMS}} \cdot R_{\text{dq}}$) and the thickness of the effective medium roughness (d_{EMA}) with linear fit for abscissa values smaller than 2 nm. The inset shows the secondary effect of correlation length (ξ) on d_{EMA} for points which have an $R_{\text{RMS}} \cdot R_{\text{dq}}$ value of ~ 3.4 nm.

Rayleigh-Rice formalism with, for example, a secondary effect of ξ on d_{EMA} at a unique $R_{\text{RMS}} \cdot R_{\text{dq}}$ value (see inset in Fig. 5.7). The linear relationship, mentioned in the many experimental reports, between R_{RMS} measured by AFM and d_{EMA} measured by ellipsometry can be explained by the fact that the slopes remain constant in most roughening dynamics [121].

5.3 Conclusions

Finite element method proves to be a very useful tool to simulate the ellipsometric response of light reflected from microscopic stochastic surface roughness. Not hindered by the sample preparation and the experimental conditions, I was able to define ideal Gaussian random surfaces with well-defined morphological parameters, such as the RMS roughness and the lateral correlation length in my case. As the Bruggeman effective medium approximation is the most widely used model in ellipsometric evaluations of surface roughness, the focus of this chapter was aimed at the correlation between the fitted B-EMA thickness and the RMS roughness. I found a linear relationship between the d_{EMA} and the product of the RMS roughness and the average surface slope for smaller d_{EMA} values, in accordance with the results analytically calculated with Rayleigh-Rice formalism and with the vast experimental measurements reported in previous studies. The deviation from the linear relationship foreshadows further corrections between the relationship of d_{EMA} and the surface morphological parameters.

Acknowledgments

The present work would not have been possible to realize without the help of many academics, coworkers, friends and family.

Firstly, I would like to thank the directors of the institutes and university of whom I was affiliated to during PhD studies for their financial and academic support that made possible to realize my research projects:

Dr. Ákos Horváth, director of the Center for Energy Research, Prof. István Bársony, former, and Dr. Béla Pécz, current director of the Institute for Technical Physics and Materials Science. Dr. Daniel Alquier, former director of the French GREMAN laboratory affiliated to the Francois Rabelais University of Tours. Prof. János Hebling, director of the Doctoral School of Physics, Faculty of Science, University of Pécs.

I greatly thank Dr. Péter Petrik, my supervisor, for accepting my application to become a PhD student and giving me the possibility to realize my thesis. He not only oversaw my work but also gave me valuable advice and relentless support in the harshest times, like last minute corrections and the replacement of my “broken” notebook.

I also thank Dr. Miklós Fried for the organization of the projects I took part of and for the expansion of my knowledge, even on literature and cinema.

I greatly acknowledge the reviewers, Dr. Péter Basa and Dr. János Volk for their thorough revision, and for the questions and advices that helped me improve the thesis. I also thank Dr. Judit Budai for accepting to review the thesis for the defence.

Many thanks go to my Hungarian, French and German coauthors, Dr. Sven Burger, Dr. Péter Kozma, Dr. Emil Agócs, Benjamin Kalas, Dr. Gaël Gautier, Dr. Thomas Defforge, Dr. Benjamin Bardet, Dr. Frédéric Cayrel. Without their knowledge and effort my research could not have been realized and my papers published.

Special thanks to colleagues for the technical support and advice: Dr. Tivadar Lohner, Dr. Norbert Nagy, Dr. David Chouteau, Dr. Damien Valente and László Makai.

I appreciate the good mood and the positive work environment that my colleagues provided during all the years; thank you Andi, Bogi, Jutka, András, Milán, Magali, Georgio, Hugo, Jaweb, Rami and Sanahan.

Last but not least, I would like to thank my closest friends, my family and my beloved for their relentless encouragement and loving support.

Summary

In the present thesis work, I have applied spectroscopic ellipsometry (SE) to describe several different silicon-based nanostructures. I characterized the SE measurements that I made on the samples presented in Chapters 2, 3, and 4 with effective medium theory-based models in such a way as to obtain the most morphological information possible. The models that I developed could be easily implemented to *ex situ* characterizations of similar nanostructured materials or even to *in situ* process control (in an industrial production line).

In Chapter 2, I described the in-depth profile of implantation induced defects, and of post-annealing induced cavities formed in various helium-implanted c-Si wafers covered with a sacrificial oxide layer. In Chapter 3, I presented the characterization of as-formed and post-oxidized porous silicon (PSi) layers that I measured with an optical and an infrared ellipsometer. This wide spectral range permitted the accurate characterization of the PSi properties from the top of the surface to the bottom of the layer with thicknesses from several hundred nanometers up to a few tens of micrometers. I dedicated Chapter 4 to the description of the optical and geometrical anisotropy of electrochemically etched porous silicon (PSi) formed by a wide range of current density and of some highly anisotropic layers composed of silicon nanowires (SiNW). Finally, in Chapter 5, I presented the ellipsometric results of simulations that I made with finite element method of a large number of rough silicon surfaces. I made a simple Bruggeman effective medium approximation fitting of the roughness layer and correlated the well-defined surface roughness parameters to the effective medium layer thickness.

The following theses summarize the results supported by publications (see **Publications strictly related to the thesis**) as my own contribution to the present work:

1. I had developed a multilayer, multi-parametric optical model that I successfully used to determine the influence of the masking oxide layer, fluence and heat treatment on the depth

distribution of cavities formed in helium implanted single-crystalline silicon. I have shown that spectroscopic ellipsometry is suitable for determining the depth distribution of cavities in a resolution comparable to or greater than electron microscopy and thereby suitable for rapid, high-sensitivity and non-destructive testing of these samples. I have found that the total volume of the cavities greatly increases with increasing ion fluence, while the peak density of the cavity distribution becomes more localized to the surface region. [T4, T8].

2. I had developed optical models for ultraviolet-near-infrared (191–1690 nm) and mid-infrared (1.7–16.7 μm) wavelength range, with which I was able to determine the thickness, average porosity, in-depth porosity distribution, lateral inhomogeneity, oxidation level and surface roughness of porous silicon (PSi) layers of a broad thickness range (0.7–52 μm). I showed with ellipsometry the uneven in-depth porosity distribution of thick PSi layers (25–52 μm). By analyzing the volume ratio of porous and oxidized content, I have shown that the oxidation of the porous structure reproduces the same volume expansion as would be obtained when oxidizing plane wafers [T3, T7].

3. I had created optical models and a qualification procedure based on them for anisotropic porous silicon (PSi) and silicon nanowire (SiNW) layers, with which I revealed that the optical behavior of PSi layers etched with low current density (2–40 mA/cm^2) is dominated by the in-depth gradient of the porosity (beyond the average porosity and the layer thickness), but in the case of the samples created at high current density (200–800 mA/cm^2), anisotropy becomes the dominant feature. I have also shown that the SiNW layers are highly anisotropic and the fibrous structure revealing the best orientation is obtained for the 1 μm wire length. I have shown that the SiNW layers formed up to a thickness of ~ 4 μm can be described by effective medium approximation-based models, above this thickness, light scattering from the layers is significant in the visible, near-infrared range [T1, T5].

4. I have shown that ellipsometric spectra of rough surfaces simulated by finite element method and by effective medium approximation are in good agreement for random surfaces with a Gaussian distribution if the wavelength of illumination is much larger than the root-mean-square height. I revealed quadratic relations between the root-mean-square heights and the effective medium layer thickness for given auto-correlation lengths. I have shown that these quadratic relations can be expressed as a linear relationship between the effective medium thickness and the product of the root-mean-square height (in case it is less than 5 nm) and the average surface slope [T2, T6].

Összefoglaló

Az értekezésemben spektroszkópai ellipszometriát alkalmaztam különböző szilícium alapú nanostruktúrák tanulmányozására. A 2., 3. és 4. fejezetekben bemutatott mintákon elvégzett mérések kiértékeléséhez olyan effektív közeg elméletre alapuló modelleket dolgoztam ki, amelyek révén a legtöbb morfológiai információt tudtam meghatározni a mintákról. A kidolgozott modellek könnyen implementálhatók hasonló nanostrukturált anyagok *ex situ* jellemzéséhez vagy akár *in situ* folyamatszabályozáshoz (egy ipari gyártósoron).

A 2. fejezetben tanulmányoztam az implantáció okozta mélységbeli roncsoltsági profilokat és a hőkezelés hatására képződő üregeloszlás profilokat különböző He implantációnak alávetett egykristályos szilícium mintákban. Az implantáció árnyékoló oxid rétegeken keresztül történt, hogy az üregeloszlást kontroláljuk. A 3. fejezetben különböző módszerekkel oxidált és oxidálatlan pórusos szilícium vékonyrétegeket mértem meg látható és infravörös ellipszométerekkel, és modelleket dolgoztam ki a mért spektrumok értelmezésére. A két műszer által lefedett széles hullámhossztartomány révén ki tudtam pontosan értékelni a vékonyrétegeket a felülettől a határfelületig néhány száz nanométeres réteg vastagságoktól egészen néhány tíz mikrométeres réteg vastagságokig. A 4. fejezetet több, nagyban eltérő áramsűrűség mellett maratott pórusos szilícium vékonyréteg és orientált nanoszálakból álló vékonyréteg optikai és geometriai anizotrópia leírására szántam. Végezetül az 5. fejezetben nagyszámú végeeselemes módszerrel szimulált érdes szilícium felület ellipszometriai eredményeit mutattam be. Egy egyrétegű Bruggeman effektív közeg közelítésen alapuló réteggel illesztettem a felületi érdesség szimulált spektrumait, és e réteg vastagságát a jól definiált felületi érdességet leíró paraméterek függvényében tanulmányoztam.

Az alábbi, publikációkkal alátámasztott tézispontjaim foglalják össze az értekezésben szereplő saját eredményeimet:

1. Sokréteges, sokparaméteres optikai modellt alkottam, amely segítségével meghatároztam az árnyékoló oxid réteg, a fluencia és a hőkezelés hatását a héliummal implantált egykristályos szilíciumban létrejövő üregek mélységeloszlására. Megmutattam, hogy a spektroszkópai ellipszometria alkalmas az üregek mélységeloszlásának az elektronmikroszkópiával összemérhető vagy azt meghaladó felbontású meghatározására, és rámutattam, hogy ezáltal a módszer alkalmas ilyen minták gyors, nagyérzékenységű és roncsolásmentes minősítésre. Megállapítottam, hogy növekvő fluencia mellett az üregek teljes térfogati aránya nagymértékben növekszik és az üregeleszlás sűrűségének csúcsa a felülethez közelebb kerül. [T4, T8].

2. Ultraibolya-közeli-infravörös (191–1690 nm) és közép-infravörös (1.7–16.7 μm) hullámhossztartományokhoz olyan optikai modelleket dolgoztam ki, amelyek révén széles vastagságtartományon (0.7–52 μm) belül tudtam meghatározni pórusos szilícium (PSi) rétegek vastagságát, átlagos porozitását, a porozitás mélységbeli eloszlását, laterális inhomogenitását, felületi érdességét és oxidációs szintjét. Rámutattam a vastag PSi rétegek (25–52 μm) porozitásának ellipszometriával meghatározható egyenetlen mélységeloszlására. A pórusos és oxidált térfogatarányok elemzésével megmutattam, hogy a pórusos szerkezet oxidációja ugyanolyan térfogati változást mutat, mint amit sík szilícium rétegek oxidálása esetében kapnánk [T3, T7].

3. Anizotróp pórusos szilícium (PSi) és szilícium nanoszál (SiNW) rétegekhez olyan optikai modelleket és ezekre épülő minősítési eljárást alkottam, amelyek segítségével megállapítottam, hogy az alacsony marási áramsűrűséggel (2–40 mA/cm^2) kialakított PSi rétegek optikai viselkedését a porozitás mélységbeli gradiense dominálja (az átlagos porozitáson és rétegvastagságon túl), viszont a nagy áramsűrűség (200–800 mA/cm^2) mellett létrehozott minták esetén az anizotrópia válik optikailag meghatározóvá. Megmutattam, hogy a SiNW-ból álló rétegek erősen anizotrópák, továbbá a leginkább orientált szálas szerkezet az

1 μm szálhosszúság esetén érhető el. Megmutattam, hogy az általunk előállított SiNW-ból álló rétegek maximum 4 μm vastagságig leírhatók egyszerű effektív közeg közelítéssel, efelett a rétegek fényszórása jelentős a látható-közeli infra tartományban [T1, T5].

4. Megmutattam, hogy a végeselem módszerrel és az effektív közeg közelítéssel számolt ellipszometriai spektrumok Gauss eloszlással rendelkező véletlen érdességű felületekre jó egyezést mutatnak, amennyiben a megvilágítás hullámhossza sokkal nagyobb, mint a négyzetes középmagasság. Kvadratikus kapcsolatot fedtem föl a négyzetes középmagasság és az effektív közegből álló réteg vastagsága között egy adott autokorrelációs hossz esetén. Megmutattam, hogy ezen kvadratikus kapcsolat kifejezhető egy lineáris összefüggéssel az effektív közeg vastagsága (<5 nm esetében) és a négyzetes középmagasságból és közepes dőlésből álló szorzat között [T2, T6].

List of publications

Publications strictly related to the thesis

Articles published in peer-reviewed journals:

- [T1] **B. Fodor**, T. Defforge, E. Agócs, M. Fried, G. Gautier, P. Petrik , “Spectroscopic ellipsometry of columnar porous Si thin films and Si nanowires”, Applied Surface Science, 421 (2017) 39, DOI: [10.1016/j.apsusc.2016.12.063](https://doi.org/10.1016/j.apsusc.2016.12.063).
- [T2] **B. Fodor**, P. Kozma, S. Burger, M. Fried, P. Petrik, “Effective medium approximation of ellipsometric response from random surface roughness simulated by finite-element method”, Thin Solid Films 617 (2016) 20, DOI: [10.1016/j.tsf.2016.01.054](https://doi.org/10.1016/j.tsf.2016.01.054).
- [T3] **B. Fodor**, E. Agocs, B. Bardet, T. Defforge, F. Cayrel, D. Alquier, M. Fried, G. Gautier, P. Petrik, “Porosity and thickness characterization of porous Si and oxidized porous Si layers – an ultraviolet-visible-mid infrared ellipsometry study”, Microporous and Mesoporous Materials 127: (2016) 112, DOI: [10.1016/j.micromeso.2016.02.039](https://doi.org/10.1016/j.micromeso.2016.02.039).
- [T4] **B. Fodor**, F. Cayrel, P. Petrik, E. Agocs, D. Alquier, M. Fried: “Characterization of in-depth cavity distribution after thermal annealing of helium-implanted silicon and gallium nitride”, Thin Solid Films 571 (2014) 567, DOI: [10.1016/j.tsf.2014.02.014](https://doi.org/10.1016/j.tsf.2014.02.014).

Results presented at conferences:

- [T5] **B. Fodor**, T. Defforge, B. Bardet, E. Agócs, F. Cayrel, M. Fried, G. Gautier, P. Petrik, “Spectroscopic Ellipsometry of Columnar Porous Si Thin Films and Si Nanowires”,

ICSE-VII (7th International Conference on Spectroscopic Ellipsometry), poster presentation, 2016.06.06–10, Berlin, Germany.

[T6] **B. Fodor**, P. Kozma, S. Burger, M. Fried, P. Petrik, “Comparison of effective medium and finite element methods for photonic structures”, EMRS 2015 Spring, oral presentation, 2015.05.11–15, Lille, France.

[T7] **B. Fodor**, E. Agocs, G. Gautier, T. Defforge, B. Bardet, D. Alquier, M. Fried, P. Petrik, “Ellipsometric Characterization of Porous Silicon and Oxidized Porous Silicon Layers within a Wide Spectral Range”, EVC13 (13th European Vacuum Conference), poster presentation, 2014.09.08–12, Aveiro, Portugal.

[T8] **B. Fodor**, F. Cayrel, P. Petrik, E. Agocs, D. Alquier, M. Fried, “Characterization of in-depth cavity distribution after thermal annealing of helium-implanted silicon and gallium nitride”, ICSE-VI (6th International Conference on Spectroscopic Ellipsometry), poster presentation, 2013.05.26–31, Kyoto, Japan.

Other publications

Articles published in peer-reviewed journals:

[O1] E. Agocs, Z. Zolnai, A.K. Rossall, J.A. van den Berg, **B. Fodor**, D. Lehninger, L. Khomenkova, S. Ponomaryov, O. Dugymenko, V. Yukhymchuk, B. Kalas, J. Heitmann, P. Petrik, “Optical and structural characterization of Ge clusters embedded in ZrO₂”, *Applied Surface Science*, 421 (2017) 283, DOI: [10.1016/j.apsusc.2017.03.153](https://doi.org/10.1016/j.apsusc.2017.03.153).

[O2] E. Agócs, P. Kozma, J. Nádor, A. Hámori, M. Janosov, B. Kalas, S. Kurunczi, **B. Fodor**, E. Ehrentreich-Förster, M. Fried, R. Horvath, P. Petrik, “Grating coupled optical waveguide interferometry combined with in situ spectroscopic ellipsometry to monitor surface processes in aqueous solutions”, *Applied Surface Science*, 421 (2017)

289, DOI: [10.1016/j.apsusc.2016.07.166](https://doi.org/10.1016/j.apsusc.2016.07.166).

- [O3] P. Petrik, E. Agocs, B. Kalas, **B. Fodor**, T. Lohner, J. Nador, A. Saftics, S. Kurunczi, T. Novotny, E. Perez-Feró, R. Nagy, A. Hamori, R. Horvath, Z. Hózer, M. Fried, "Nanophotonics of biomaterials and inorganic nanostructures", J. Phys.: Conf. Ser 794 (2017) 012004, DOI: [10.1088/1742-6596/794/1/012004](https://doi.org/10.1088/1742-6596/794/1/012004).
- [O4] B. Lu, T. Defforge, **B. Fodor**, B. Morillon, D. Alquier, G. Gautier, "Optimized plasma-polymerized fluoropolymer mask for local porous silicon formation", Journal of Applied Physics, 119 21 (2016) 213301, DOI: [10.1063/1.4953088](https://doi.org/10.1063/1.4953088).
- [O5] P. Petrik, N. Kumar, M. Fried, **B. Fodor**, G. Juhasz, S. F. Pereira, S. Burger, H. P. Urbach, "Fourier ellipsometry - An ellipsometric approach to Fourier scatterometry", JEOS:RP 10 (2015) 15002, DOI: [10.2971/jeos.2015.15002](https://doi.org/10.2971/jeos.2015.15002).
- [O6] P. Petrik, E. Agocs, B. Kalas, P. Kozma, **B. Fodor**, J. Nador, C. Major, M. Fried, "Multiple angle of incidence, spectroscopic, plasmon-enhanced, internal reflection ellipsometry for the characterization of solid-liquid interface processes", Proc. SPIE - Int. Soc. Opt. Eng., 95290W (2015), DOI: [10.1117/12.2184850](https://doi.org/10.1117/12.2184850).
- [O7] P. Petrik, **B. Fodor**, E. Agocs, P. Kozma, J. Nador, N. Kumar, J. Endres, G. Juhasz, C. Major, S.F. Pereira, T. Lohner, H.P. Urbach, B. Bodermann, M. Fried, "Methods for optical modeling and cross-checking in ellipsometry and scatterometry", Proc. SPIE - Int. Soc. Opt. Eng., 95260S (2015), DOI: [10.1117/12.2184833](https://doi.org/10.1117/12.2184833).
- [O8] J. Landwehr, R. Fader, M. Rumler, M. Rommel, A. Bauer, L. Frey, B. Simon, **B. Fodor**, P. Petrik, A. Schiener, B. Winter, E. Spieker, "Optical polymers with tunable refractive index for nanoimprint technologies", Nanotechnology (2014) 25 505301, DOI: [10.1088/0957-4484/25/50/505301](https://doi.org/10.1088/0957-4484/25/50/505301).
- [O9] E. Agocs, **B. Fodor**, B. Pollakowski, B. Beckhoff, A. Nutsch, M. Jank, P. Petrik "Approaches to calculate the dielectric function of ZnO around the band gap", Thin Solid Films (2014), DOI: [10.1016/j.tsf.2014.03.028](https://doi.org/10.1016/j.tsf.2014.03.028).
- [O10] P. Petrik, E. Agocs, J. Volk, I. Lukacs, **B. Fodor**, P. Kozma, T. Lohner, S. Oh, Y. Wakayama,

- T. Nagata, M. Fried, „Resolving lateral and vertical structures by ellipsometry using wavelength range scan”, *Thin Solid Films* (2014), DOI: [10.1016/j.tsf.2014.02.008](https://doi.org/10.1016/j.tsf.2014.02.008).
- [O11] P. Petrik, N. Kumar, G. Juhasz, C. Major, **B. Fodor**, E. Agocs, T. Lohner, S.F. Pereira, H.P. Urbach, M. Fried, “Optical characterization of macro-, micro- and nanostructures using polarized light”, *J. Phys.: Conf. Ser* 558 (2014) 012008, DOI: [10.1088/1742-6596/558/1/012008](https://doi.org/10.1088/1742-6596/558/1/012008).
- [O12] A. Saftics, E. Agócs, **B. Fodor**, D. Patkó, P. Petrik, K. Kolari, T. Aalto, P. Fürjes, R. Horvath, S. Kurunczi, “Investigation of thin polymer layers for biosensor applications”, *Applied Surface Science* (2013), DOI: [10.1016/j.apsusc.2012.12.042](https://doi.org/10.1016/j.apsusc.2012.12.042).
- [O13] Szekeres, S. Alexandrova, P. Petrik, **B. Fodor**, S. Bakalova, “Ellipsometric study of crystalline silicon hydrogenated by plasma immersion ion implantation”, *Applied Surface Science* (2013), DOI: [10.1016/j.apsusc.2012.12.024](https://doi.org/10.1016/j.apsusc.2012.12.024).
- [O14] P. Petrik, T. Gumprecht, A. Nutsch, G. Roeder, M. Lemberger, G. Juhasz, O. Polgar, C. Major, P. Kozma, M. Janosov, **B. Fodor**, E. Agocs, M. Fried, “Comparative measurements on atomic layer deposited Al₂O₃ thin films using ex situ table top and mapping ellipsometry, as well as X-ray and VUV reflectometry”, *Thin Solid Films* (2013), DOI: [10.1016/j.tsf.2012.12.091](https://doi.org/10.1016/j.tsf.2012.12.091).
- [O15] P. Kozma, **B. Fodor**, A. Deak, P. Petrik, “Optical Models for the Characterization of Silica Nanosphere Monolayers Prepared by the Langmuir-Blodgett Method Using Ellipsometry in the Quasistatic Regime”, *Langmuir* (2010), DOI: [10.1021/la1028838](https://doi.org/10.1021/la1028838).

Results presented at conferences:

- [O16] **Fodor B.**, Petrik P., „Szilika nanogömbökből álló vékonyrétegek tanulmányozása ellipszometriával”, MTA TTK Doctoral Conference, oral presentation, 2014.12.10–12, Budapest, Hungary.
- [O17] **B. Fodor**, P. Petrik, J. Volk, I. Lukacs, S. Oh, Y. Wakayama, T. Nagata, M. Fried, “Mueller Matrix Ellipsometry of Two-Dimensional Periodic Submicron Structures”, EMRS 2012 Fall, poster presentation, 2012.09.17–21, Warsaw, Poland.

- [O18] **B. Fodor**, P. Kozma, N. Nagy, Z. Zolnai, P. Petrik, M. Fried, “Ellipsometric Characterization of Ion Irradiated Monolayers Prepared from Submicron Silica Particles”, EMRS 2012 Spring, oral presentation, 2012.05.14–18, Strasbourg, France.
- [O19] **B. Fodor**, P. Kozma, A. Deak , N. Nagy , Z. Zolnai , P. Petrik , M. Fried, “Spectroscopic Ellipsometry Investigation of Silica Nanosphere Monolayers before and after Ion Irradiation-induced Shape Transformation”, EuroNanoForum, poster presentation, 2011.05.30–06.01, Budapest, Hungary.
- [O20] **B. Fodor**, P. Kozma, A. Deak, Z. Zolnai, P. Petrik, M. Fried, “Optical Models for the Characterization of Silica Nanosphere Monolayers investigated by Spectroscopic Ellipsometry”, 6th Workshop Ellipsometry, oral presentation, 2011.02.21–24, Berlin, Germany.

Bibliography

- [1] International Technology Roadmap for Semiconductors 2.0, Executive Report, 2015.
- [2] H.G. Tompkins, W.A. McGahan, Spectroscopic Ellipsometry and Reflectometry: A User's Guide to Ellipsometry, John Wiley & Sons, Ltd., New York, 1999.
- [3] H. Fujiwara, Spectroscopic Ellipsometry: Principles and Applications, Wiley, New York, 2007. doi:10.1002/9780470060193.
- [4] H.G. Tompkins, E.A. Irene, Handbook of ellipsometry, William Andrew, Norwich, NY, 2005.
- [5] R.M.A. Azzam, N.M. Bashara, Ellipsometry and Polarized Light, Fourth imp, Elsevier Science B.V., Amsterdam, 1987.
- [6] M. Losurdo, K. Hingerl, eds., Ellipsometry at the Nanoscale, Springer Berlin Heidelberg, Berlin, Heidelberg, 2013. doi:10.1007/978-3-642-33956-1.
- [7] M. Born, E. Wolf, Principles of optics, Sixth edit, Pergamon Press, London, 1968.
- [8] G.E. Jellison, Use of the biased estimator in the interpretation of spectroscopic ellipsometry data., Appl. Opt. 30 (1991) 3354–3360. doi:10.1364/AO.30.003354.
- [9] C.M. Herzinger, P.G. Snyder, B. Johs, J. A. Woollam, InP optical constants between 0.75 and 5.0 eV determined by variable-angle spectroscopic ellipsometry, J. Appl. Phys. 77 (1995) 1715–1724. doi:10.1063/1.358864.
- [10] G.E. Jellison, F.A. Modine, Parameterization of the optical functions of amorphous materials in the interband region, Appl. Phys. Lett. 69 (1996) 371–373. doi:10.1063/1.118064.
- [11] G.E. Jellison, F.A. Modine, Erratum: “Parameterization of the optical functions of amorphous materials in the interband region” [Appl. Phys. Lett. 69 , 371 (1996)], Appl. Phys. Lett. 69 (1996) 2137–2137. doi:10.1063/1.118155.
- [12] G.E. Jellison, V.I. Merkulov, A.A. Puretzky, D.B. Geohegan, G. Eres, D.H. Lowndes, J.B. Caughman, Characterization of thin-film amorphous semiconductors using

- spectroscopic ellipsometry, *Thin Solid Films*. 377–378 (2000) 68–73. doi:10.1016/S0040-6090(00)01384-5.
- [13] J. Tauc, R. Grigorovici, A. Vancu, Fridman, Optical Properties and Electronic Structure of Amorphous Germanium, *Phys. Status Solidi*. 15 (1966) 627–637. doi:10.1002/pssb.19660150224.
- [14] D.E. Aspnes, Optical properties of thin films, *Thin Solid Films*. 89 (1982) 249–262. doi:10.1016/0040-6090(82)90590-9.
- [15] D.E. Aspnes, Microstructural Information From Optical Properties In Semiconductor Technology, in: D.E. Aspnes, R.F. Potter, S.S. So (Eds.), *SPIE Proc.*, 1981: pp. 188–195. doi:10.1117/12.931705.
- [16] A.H. Sihvola, J.A. Kong, Effective permittivity of dielectric mixtures, *IEEE Trans. Geosci. Remote Sens.* 26 (1988) 420–429. doi:10.1109/36.3045.
- [17] J. Spanier, I. Herman, Use of hybrid phenomenological and statistical effective-medium theories of dielectric functions to model the infrared reflectance of porous SiC films, *Phys. Rev. B*. 61 (2000) 10437–10450. doi:10.1103/PhysRevB.61.10437.
- [18] V.Y. Timoshenko, L.A. Osminkina, A.I. Efimova, L.A. Golovan, P.K. Kashkarov, D. Kovalev, N. Künzner, E. Gross, J. Diener, F. Koch, Anisotropy of optical absorption in birefringent porous silicon, *Phys. Rev. B*. 67 (2003) 113405. doi:10.1103/PhysRevB.67.113405.
- [19] A. Sihvola, Dielectric Polarization and Particle Shape Effects, *J. Nanomater.* 2007 (2007). doi:10.1155/2007/45090.
- [20] L.D. Landau, L.P. Pitaevskii, E.M. Lifshitz, *Electrodynamics of Continuous Media*, 2nd Ed., 1984. doi:10.1119/1.1937882.
- [21] P. Xu, Z.Y. Li, Effect of particle shape on the effective dielectric response of nanocomposite close to the percolation threshold, *Phys. B Condens. Matter*. 348 (2004) 101–107. doi:10.1016/j.physb.2003.11.077.
- [22] W.G. Egan, D.E. Aspnes, Finite-wavelength effects in composite media, *Phys. Rev. B*. 26 (1982) 5313–5320. doi:10.1103/PhysRevB.26.5313.

- [23] D. Stroud, F.P. Pan, Self-consistent approach to electromagnetic wave propagation in composite media: Application to model granular metals, *Phys. Rev. B.* 17 (1978) 1602–1610. doi:10.1103/PhysRevB.17.1602.
- [24] V. Raineri, M. Saggio, E. Rimini, Voids in Silicon by He Implantation: From Basic to Applications, *J. Mater. Res.* 15 (2000) 1449–1477. doi:10.1557/JMR.2000.0211.
- [25] M. Bruel, Separation of silicon wafers by the smart-cut method, *Mater. Res. Innov.* 3 (1999) 9–13. doi:10.1007/s100190050119.
- [26] D. Alquier, F. Cayrel, L. Ventura, F. Roqueta, Gettering by helium implantation applied to a device: Impact of metal and dopant segregation, *Microelectron. Eng.* 66 (2003) 496–503. doi:10.1016/S0167-9317(02)00925-5.
- [27] F. Cayrel, D. Alquier, C. Dubois, R. Jérésian, Boron diffusion in presence of defects induced by helium implantation, *Mater. Sci. Eng. B.* 124–125 (2005) 271–274. doi:10.1016/j.mseb.2005.08.008.
- [28] O. Marcelot, A. Claverie, D. Alquier, F. Cayrel, W. Lerch, S. Paul, L. Rubin, V. Raineri, F. Giannazzo, H. Jaouen, Diffusion and Activation of Ultra Shallow Boron Implants in Silicon in Proximity of Voids, *Solid State Phenom.* 131–133 (2008) 357–362. doi:10.4028/www.scientific.net/SSP.131-133.357.
- [29] P. Petrik, O. Polgár, M. Fried, T. Lohner, N.Q. Khánh, J. Gyulai, Ellipsometric characterization of damage profiles using an advanced optical model, *J. Appl. Phys.* 93 (2003) 1987. doi:10.1063/1.1539306.
- [30] M. Fried, P. Petrik, T. Lohner, N.Q. Khánh, O. Polgár, J. Gyulai, Dose-dependence of ion implantation-caused damage in silicon measured by ellipsometry and backscattering spectrometry, *Thin Solid Films.* 455–456 (2004) 404–409. doi:10.1016/j.tsf.2004.01.027.
- [31] P. Petrik, T. Lohner, O. Polgar, M. Fried, Ellipsometry on ion implantation induced damage, in: 2008 16th IEEE Int. Conf. Adv. Therm. Process. Semicond., IEEE, 2008: pp. 93–101. doi:10.1109/RTP.2008.4690541.
- [32] I. Mohacsi, P. Petrik, M. Fried, T. Lohner, J.A. Van Den Berg, M.A. Reading, D. Giubertoni, M. Barozzi, A. Parisini, Characterisation of ultra-shallow disorder profiles and dielectric functions in ion implanted Si, *Thin Solid Films.* 519 (2011) 2847–2851.

doi:10.1016/j.tsf.2010.12.076.

- [33] D. Shamiryan, D. V. Likhachev, Spectroscopic Ellipsometry of Ion-Implantation-Induced Damage, in: Ion Implant., InTech, 2012. doi:10.5772/37758.
- [34] W. Fukarek, J.R. Kaschny, Cavities in helium implanted and annealed silicon characterized by spectroscopic ellipsometry, *J. Appl. Phys.* 86 (1999) 4160–4165. doi:10.1063/1.371341.
- [35] P. Petrik, F. Cayrel, M. Fried, O. Polgár, T. Lohner, L. Vincent, D. Alquier, J. Gyulai, Depth distribution of disorder and cavities in high dose helium implanted silicon characterized by spectroscopic ellipsometry, *Thin Solid Films.* 455–456 (2004) 344–348. doi:10.1016/j.tsf.2004.01.020.
- [36] P. Petrik, M. Fried, T. Lohner, O. Polgár, J. Gyulai, F. Cayrel, D. Alquier, Optical models for cavity profiles in high-dose helium-implanted and annealed silicon measured by ellipsometry, *J. Appl. Phys.* 97 (2005) 1–6. doi:10.1063/1.1937469.
- [37] P. Petrik, W. Lehnert, C. Schneider, T. Lohner, M. Fried, J. Gyulai, H. Rysse, In situ measurement of the crystallization of amorphous silicon in a vertical furnace using spectroscopic ellipsometry, *Thin Solid Films.* 383 (2001) 235–240. doi:10.1016/S0040-6090(00)01792-2.
- [38] CompleteEASE Data Analysis Manual, J. A. Woollam Co., Inc, Lincoln, 2011.
- [39] C.M. Herzinger, B. Johs, W.A. McGahan, J.A. Woollam, W. Paulson, Ellipsometric determination of optical constants for silicon and thermally grown silicon dioxide via a multi-sample, multi-wavelength, multi-angle investigation, *J. Appl. Phys.* 83 (1998) 3323–3336. doi:10.1063/1.367101.
- [40] M. Fried, T. Lohner, E. Jároli, N.Q. Khanh, C. Hajdu, J. Gyulai, Nondestructive determination of damage depth profiles in ion-implanted semiconductors by multiple-angle-of-incidence single-wavelength ellipsometry using different optical models, *J. Appl. Phys.* 72 (1992) 2197–2201. doi:10.1063/1.351611.
- [41] J.F. Ziegler, SRIM-2003, *Nucl. Instruments Methods Phys. Res. Sect. B Beam Interact. with Mater. Atoms.* 219–220 (2004) 1027–1036. doi:10.1016/j.nimb.2004.01.208.

-
- [42] T. Lohner, E. Kótai, N.Q. Khánh, Z. Tóth, M. Fried, K. Vedam, N.V. Nguyen, L.J. Hanekamp, A. van Silfhout, Ion-implantation induced anomalous surface amorphization in silicon, *Nucl. Instruments Methods Phys. Res. Sect. B Beam Interact. with Mater. Atoms.* 85 (1994) 335–339. doi:10.1016/0168-583X(94)95839-4.
- [43] T. Lohner, M. Fried, N.Q. Khánh, P. Petrik, H. Wormeester, M.A. El-Sherbiny, Comparative study of ion implantation caused anomalous surface damage in silicon studied by spectroscopic ellipsometry and Rutherford backscattering spectrometry, *Nucl. Instruments Methods Phys. Res. Sect. B Beam Interact. with Mater. Atoms.* 147 (1999) 90–95. doi:10.1016/S0168-583X(98)00594-1.
- [44] A.I. Titov, V.S. Belyakov, A.Y. Azarov, Formation of surface amorphous layers in semiconductors under low-energy light-ion irradiation: Experiment and theory, *Nucl. Instruments Methods Phys. Res. Sect. B Beam Interact. with Mater. Atoms.* 212 (2003) 169–178. doi:10.1016/S0168-583X(03)01486-1.
- [45] S.E. Donnelly, V.M. Vishnyakov, R.C. Birtcher, G. Carter, The effects of radiation damage and impurities on void dynamics in silicon, *Nucl. Instruments Methods Phys. Res. Sect. B Beam Interact. with Mater. Atoms.* 175–177 (2001) 132–139. doi:10.1016/S0168-583X(00)00612-1.
- [46] S. Frabboni, F. Corni, C. Nobili, R. Tonini, G. Ottaviani, Nanovoid formation in helium-implanted single-crystal silicon studied by in situ techniques, *Phys. Rev. B - Condens. Matter Mater. Phys.* 69 (2004) 1–6. doi:10.1103/PhysRevB.69.165209.
- [47] P. Sigmund, ed., *Ion Beam Science : Solved and Unsolved Problems*, Copenhagen, 2006.
- [48] J.H. Evans, Mechanisms of void coarsening in helium implanted silicon, *Nucl. Instruments Methods Phys. Res. Sect. B Beam Interact. with Mater. Atoms.* 196 (2002) 125–134. doi:10.1016/S0168-583X(02)01290-9.
- [49] L. Pizzagalli, M.L. David, M. Bertolus, Molecular dynamics simulation of the initial stages of He bubbles formation in silicon, *Model. Simul. Mater. Sci. Eng.* 21 (2013) 65002. doi:10.1088/0965-0393/21/6/065002.
- [50] A.G. Cullis, L.T. Canham, P.D.J. Calcott, The structural and luminescence properties of porous silicon, *J. Appl. Phys.* 82 (1997) 909–965. doi:10.1063/1.366536.

-
- [51] G. Gautier, P. Leduc, Porous silicon for electrical isolation in radio frequency devices: A review, *Appl. Phys. Rev.* 1 (2014) 11101. doi:10.1063/1.4833575.
- [52] M.S. Salem, M.J. Sailor, F.A. Harraz, T. Sakka, Y.H. Ogata, Electrochemical stabilization of porous silicon multilayers for sensing various chemical compounds, *J. Appl. Phys.* 100 (2006) 83520. doi:10.1063/1.2360389.
- [53] B. Gupta, Y. Zhu, B. Guan, P.J. Reece, J.J. Gooding, Functionalised porous silicon as a biosensor: emphasis on monitoring cells in vivo and in vitro., *Analyst.* 138 (2013) 3593–615. doi:10.1039/c3an00081h.
- [54] L. Canham, Tunable Properties of Porous Silicon, in: *Handb. Porous Silicon*, Springer International Publishing, Cham, 2014: pp. 201–206. doi:10.1007/978-3-319-05744-6_19.
- [55] A. Loni, T. Defforge, E. Caffull, G. Gautier, L.T. Canham, Porous silicon fabrication by anodisation: Progress towards the realisation of layers and powders with high surface area and micropore content, *Microporous Mesoporous Mater.* 213 (2015) 10–13. doi:10.1016/j.micromeso.2015.03.006.
- [56] M.J. Sailor, *Porous Silicon in Practice*, Wiley-VCH Verlag GmbH & Co. KGaA, Weinheim, Germany, 2011. doi:10.1002/9783527641901.
- [57] G. Gautier, S. Kouassi, Integration of porous silicon in microfuel cells: a review, *Int. J. Energy Res.* 39 (2014) 1–25. doi:10.1002/er.3206.
- [58] N. Ennejah, S. Aouida, B. Bessais, Ultra thin porous silicon films investigated by X-ray reflectometry, *Phys. Status Solidi Curr. Top. Solid State Phys.* 8 (2011) 1931–1935. doi:10.1002/pssc.201000083.
- [59] V. Chamard, P. Bastie, D. Le Bolloch, G. Dolino, E. Elkaïm, C. Ferrero, J.-P. Lauriat, F. Rieutord, D. Thiaudière, Evidence of pore correlation in porous silicon: An x-ray grazing-incidence study, *Phys. Rev. B.* 64 (2001) 245416. doi:10.1103/PhysRevB.64.245416.
- [60] S.A. Alekseev, V. Lysenko, V.N. Zaitsev, D. Barbier, Application of Infrared Interferometry for Quantitative Analysis of Chemical Groups Grafted onto the Internal Surface of Porous Silicon Nanostructures, *J. Phys. Chem. C.* 111 (2007) 15217–15222. doi:10.1021/jp0712452.

-
- [61] B. Bardet, D. De Sousa Meneses, T. Defforge, J. Billoué, G. Gautier, In situ investigation of mesoporous silicon oxidation kinetics using infrared emittance spectroscopy, *Phys. Chem. Chem. Phys.* (2016). doi:10.1039/C6CP02086K.
- [62] E. Segal, L.A. Perelman, F. Cunin, F. Di Renzo, J.-M. Devoisselle, Y.Y. Li, M.J. Sailor, Confinement of Thermoresponsive Hydrogels in Nanostructured Porous Silicon Dioxide Templates, *Adv. Funct. Mater.* 17 (2007) 1153–1162. doi:10.1002/adfm.200601077.
- [63] F. Ferrieu, A. Halimaoui, D. Bensahel, Optical characterisation of porous silicon layers by spectrometric ellipsometry in the 1.5–5 eV range, *Solid State Commun.* 84 (1992) 293–296. doi:10.1016/0038-1098(92)90124-R.
- [64] U. Rossow, U. Frotscher, M. Thönissen, M.G. Berger, S. Frohnhoff, H. Münder, W. Richter, Influence of the formation conditions on the microstructure of porous silicon layers studied by spectroscopic ellipsometry, *Thin Solid Films.* 255 (1995) 5–8. doi:10.1016/0040-6090(94)05676-5.
- [65] M. Fried, T. Lohner, O. Polgár, P. Petrik, É. Vázsonyi, I. Bársony, J.P. Piel, J.L. Stehle, Characterization of different porous silicon structures by spectroscopic ellipsometry, *Thin Solid Films.* 276 (1996) 223–227. doi:10.1016/0040-6090(95)08058-9.
- [66] S. Zangoonie, R. Jansson, H. Arwin, Microstructural control of porous silicon by electrochemical etching in mixed HCl/HF solutions, *Appl. Surf. Sci.* 136 (1998) 123–130. doi:10.1016/S0169-4332(98)00328-6.
- [67] T. Lohner, M. Fried, P. Petrik, O. Polgár, J. Gyulai, W. Lehnert, Ellipsometric characterization of oxidized porous silicon layer structures, *Mater. Sci. Eng. B Solid-State Mater. Adv. Technol.* 69 (2000) 182–187. doi:10.1016/S0921-5107(99)00257-3.
- [68] M. Fried, O. Polgár, T. Lohner, S. Strehlke, C. Levy-Clement, Comparative study of the oxidation of thin porous silicon layers studied by reflectometry , spectroscopic ellipsometry and secondary ion mass spectroscopy, *J. Lumin.* 80 (1999) 147–152. doi:10.1016/S0022-2313(98)00086-6.
- [69] H. Krzyżanowska, M. Kulik, J. Żuk, Ellipsometric study of refractive index anisotropy in porous silicon, *J. Lumin.* 80 (1998) 183–186. doi:10.1016/S0022-2313(98)00093-3.
- [70] É. Vázsonyi, E. Szilágyi, P. Petrik, Z.E. Horváth, T. Lohner, M. Fried, G. Jalsovszky, Porous

- silicon formation by stain etching, *Thin Solid Films*. 388 (2001) 295–302. doi:10.1016/S0040-6090(00)01816-2.
- [71] C. Wongmanerod, S. Zangoie, H. Arwin, Determination of pore size distribution and surface area of thin porous silicon layers by spectroscopic ellipsometry, *Appl. Surf. Sci.* 172 (2001) 117–125. doi:10.1016/S0169-4332(00)00847-3.
- [72] P. Petrik, É. Vázquez, M. Fried, J. Volk, G.T. Andrews, A.L. Tóth, C.S. Daróczy, I. Bársony, J. Gyulai, Optical models for the ellipsometric characterisation of porous silicon structures, *Phys. Status Solidi C Conf. 2* (2005) 3319–3323. doi:10.1002/pssc.200461153.
- [73] P. Petrik, M. Fried, É. Vázquez, T. Lohner, E. Horváth, O. Polgár, P. Basa, I. Bársony, J. Gyulai, Ellipsometric characterization of nanocrystals in porous silicon, *Appl. Surf. Sci.* 253 (2006) 200–203. doi:10.1016/j.apsusc.2006.05.087.
- [74] P. Petrik, M. Fried, E. Vazsonyi, P. Basa, T. Lohner, P. Kozma, Z. Makkai, Nanocrystal characterization by ellipsometry in porous silicon using model dielectric function, *J. Appl. Phys.* 105 (2009) 1–6. doi:10.1063/1.3068479.
- [75] M.R. Baklanov, K.P. Mogilnikov, V.G. Polovinkin, F.N. Dultsev, Determination of pore size distribution in thin films by ellipsometric porosimetry, *J. Vac. Sci. Technol. B Microelectron. Nanom. Struct.* 18 (2000) 1385. doi:10.1116/1.591390.
- [76] M. Fried, H. Wormeester, E. Zoethout, T. Lohner, O. Polgár, I. Bársony, In Situ Spectroscopic Ellipsometric Investigation of Vacuum Annealed and Oxidized Porous Silicon Layers, *Thin Solid Films*. 313–314 (1998) 459. doi:10.1016/S0040-6090(97)00864-X.
- [77] P. Petrik, T. Lohner, M. Fried, L.P. Biró, N.Q. Khánh, J. Gyulai, W. Lehnert, C. Schneider, H. Ryssel, Ellipsometric study of polycrystalline silicon films prepared by low-pressure chemical vapor deposition, *J. Appl. Phys.* 87 (2000) 1734–1742. doi:10.1063/1.372085.
- [78] Z. Montiel-González, S. Escobar, R. Nava, J.A. Del Río, J. Tagüeña-Martínez, Role of an Oxidant Mixture as Surface Modifier of Porous Silicon Microstructures Evaluated by Spectroscopic Ellipsometry, *Sci. Rep.* 6 (2016) 2–9. doi:10.1038/srep24798.
- [79] R. Kitamura, L. Pilon, M. Jonasz, Optical constants of silica glass from extreme ultraviolet to far infrared at near room temperature., *Appl. Opt.* 46 (2007) 8118–8133.

doi:10.1364/AO.46.008118.

- [80] K.S.W. Sing, D.H. Everett, R.A.W. Haul, L. Moscou, R. A. Pierotti, J. Rouquérol, T. Siemieniewska, Reporting physisorption data for gas/solid systems with special reference to the determination of surface area and porosity, *Pure Appl. Chem.* 57 (1985) 603–619. doi:10.1351/pac198557040603.
- [81] K.B. Clark, J.A. Bardwell, J.M. Baribeau, Physical characterization of ultrathin anodic silicon oxide films, *J. Appl. Phys.* 76 (1994) 3114–3122. doi:10.1063/1.357493.
- [82] G.E. Jellison, The Calculation of Thin Film Parameters from Spectroscopic Ellipsometry Data, *Thin Solid Films.* 29 (2008) 40–45. doi:10.1016/S0040-6090(96)09009-8.
- [83] R.W. Collins, I. An, J. Lee, J.A. Zapien, Multichannel Ellipsometry, in: H.G. Tompkins, E.A. Irene (Eds.), *Handb. Ellipsom.*, Elsevier, 2005: pp. 481–566. doi:10.1016/B978-081551499-2.50009-5.
- [84] W. Theiss, S. Henkel, M. Arntzen, Connecting microscopic and macroscopic properties of porous media: choosing appropriate effective medium concepts, *Thin Solid Films.* 255 (1995) 177–180. doi:10.1016/0040-6090(94)05649-X.
- [85] W. Theiss, Optical properties of porous silicon, *Surf. Sci. Rep.* 29 (1997) 91–192. doi:10.1016/S0167-5729(96)00012-X.
- [86] L.A.A. Pettersson, L. Hultman, H. Arwin, Porosity Depth Profiling of Thin Porous Silicon Layers by use of Variable-Angle Spectroscopic Ellipsometry: A Porosity Graded-Layer Model, *Appl. Opt.* 37 (1998) 4130. doi:10.1364/AO.37.004130.
- [87] V. Lehmann, R. Stengl, A. Luigart, On the morphology and the electrochemical formation mechanism of mesoporous silicon, *Mater. Sci. Eng. B Solid-State Mater. Adv. Technol.* 69 (2000) 11–22. doi:10.1016/S0921-5107(99)00286-X.
- [88] R. Herino, Porosity and Pore Size Distributions of Porous Silicon Layers, *J. Electrochem. Soc.* 134 (1987) 1994. doi:10.1149/1.2100805.
- [89] S.E. Foss, P.Y.Y. Kan, T.G. Finstad, Single beam determination of porosity and etch rate in situ during etching of porous silicon, *J. Appl. Phys.* 97 (2005) 114909. doi:10.1063/1.1925762.

-
- [90] T.D. James, A.J. Keating, G. Parish, C.A. Musca, Pulsed Anodization for Control of Porosity Gradients and Interface Roughness in Porous Silicon, *J. Electrochem. Soc.* 156 (2009) H744. doi:10.1149/1.3174319.
- [91] A. Loni, Porous Silicon Formation by Anodization, in: L. Canham (Ed.), *Handb. Porous Silicon*, Springer International Publishing, Cham, 2014: pp. 11–22. doi:10.1007/978-3-319-05744-6_2.
- [92] K.W. Kolasinski, Porous Silicon Formation by Galvanic Etching, in: *Handb. Porous Silicon*, Springer International Publishing, Cham, 2014: pp. 23–33. doi:10.1007/978-3-319-05744-6_3.
- [93] Y.H. Ogata, T. Tsuboi, T. Sakka, S. Naito, Oxidation of Porous Silicon in Dry and Wet Environments under Mild Temperature Conditions, *J. Porous Mater.* 7 (2000) 63–66. doi:10.1023/A:1009694608199.
- [94] K. Barla, R. Herino, G. Bomchil, Stress in oxidized porous silicon layers, *J. Appl. Phys.* 59 (1986) 439–441. doi:10.1063/1.337036.
- [95] S.F. Chuang, S.D. Collins, R.L. Smith, Preferential propagation of pores during the formation of porous silicon: A transmission electron microscopy study, *Appl. Phys. Lett.* 55 (1989) 675–677. doi:10.1063/1.101819.
- [96] M. Fujii, J. Diener, Optical Birefringence of Porous Silicon, in: L. Canham (Ed.), *Handb. Porous Silicon*, Springer International Publishing, Cham, 2014: pp. 245–253. doi:10.1007/978-3-319-05744-6_26.
- [97] X. Li, P.W. Bohn, Metal-assisted chemical etching in HF/H₂O produces porous silicon, *Appl. Phys. Lett.* 77 (2000) 2572. doi:10.1063/1.1319191.
- [98] Z. Huang, N. Geyer, P. Werner, J. de Boer, U. Gösele, Metal-Assisted Chemical Etching of Silicon: A Review, *Adv. Mater.* 23 (2011) 285–308. doi:10.1002/adma.201001784.
- [99] R. Agarwal, C.M. Lieber, Semiconductor nanowires: Optics and optoelectronics, *Appl. Phys. A Mater. Sci. Process.* 85 (2006) 209–215. doi:10.1007/s00339-006-3720-z.
- [100] A.I. Hochbaum, D. Gargas, Y.J. Hwang, P. Yang, Single Crystalline Mesoporous Silicon Nanowires, *Nano Lett.* 9 (2009) 3550–3554. doi:10.1021/nl9017594.

- [101] X. Zhong, Y. Qu, Y.C. Lin, L. Liao, X. Duan, Unveiling the formation pathway of single crystalline porous silicon nanowires, *ACS Appl. Mater. Interfaces*. 3 (2011) 261–270. doi:10.1021/am1009056.
- [102] M. Schubert, Generalized ellipsometry and complex optical systems, *Thin Solid Films*. 313–314 (1998) 323–332. doi:10.1016/S0040-6090(97)00841-9.
- [103] H. Looyenga, Dielectric constants of heterogeneous mixtures, *Physica*. 31 (1965) 401–406. doi:10.1016/0031-8914(65)90045-5.
- [104] D.J. Bergman, The dielectric constant of a composite material-A problem in classical physics, *Phys. Rep.* 43 (1978) 377–407. doi:10.1016/0370-1573(78)90009-1.
- [105] A. V. Goncharenko, Generalizations of the Bruggeman equation and a concept of shape-distributed particle composites, *Phys. Rev. E*. 68 (2003) 41108. doi:10.1103/PhysRevE.68.041108.
- [106] A. V. Goncharenko, E.F. Venger, Percolation threshold for Bruggeman composites, *Phys. Rev. E - Stat. Nonlinear, Soft Matter Phys.* 70 (2004) 1–4. doi:10.1103/PhysRevE.70.057102.
- [107] E. Agocs, A.G. Nassiopoulou, S. Milita, P. Petrik, Model dielectric function analysis of the critical point features of silicon nanocrystal films in a broad parameter range, *Thin Solid Films*. 541 (2013) 83–86. doi:10.1016/j.tsf.2012.10.126.
- [108] P. Allongue, Porous silicon formation mechanisms, in: L. Canham (Ed.), *Prop. Porous Silicon*, INSPEC, 1997.
- [109] C.S. Solanki, R.R. Bilyalov, J. Poortmans, J.-P. Celis, J. Nijs, R. Mertens, Self-Standing Porous Silicon Films by One-Step Anodizing, *J. Electrochem. Soc.* 151 (2004) C307. doi:10.1149/1.1688797.
- [110] D. Kovalev, G. Polisski, J. Diener, H. Heckler, N. Künzner, F. Koch, Anisotropically nanostructured silicon as an efficient optical retarder, *Phys. Status Solidi Appl. Res.* 180 (2000) 78–80. doi:10.1002/1521-396X(200008)180:2<R8::AID-PSSA99998>3.0.CO;2-E.
- [111] J. Diener, N. Künzner, D. Kovalev, E. Gross, V.Y. Timoshenko, G. Polisski, F. Koch, Dichroic Bragg reflectors based on birefringent porous silicon, *Appl. Phys. Lett.* 78 (2001) 3887–

3889. doi:10.1063/1.1378045.
- [112] J. Diener, N. Künzner, D. Kovalev, E. Gross, F. Koch, M. Fujii, Dichroic behavior of multilayer structures based on anisotropically nanostructured silicon, *J. Appl. Phys.* 91 (2002) 6704–6709. doi:10.1063/1.1471581.
- [113] J. Diener, N. Künzner, E. Gross, D. Kovalev, M. Fujii, Planar silicon-based light polarizers, *Opt Lett.* 29 (2004) 195–197. doi:10.1364/OL.29.000195.
- [114] S.H. Hsu, E.S. Liu, Y.C. Chang, J.N. Hilfiker, Y.D. Kim, T.J. Kim, C.J. Lin, G.R. Lin, Characterization of Si nanorods by spectroscopic ellipsometry with efficient theoretical modeling, *Phys. Status Solidi Appl. Mater. Sci.* 205 (2008) 876–879. doi:10.1002/pssa.200777832.
- [115] M. Khorasaninejad, S. Patchett, J. Sun, N. O, S.S. Saini, Polarization-resolved reflections in ordered and bunched silicon nanowire arrays, *J. Opt. Soc. Am. B.* 29 (2012) 3063. doi:10.1364/JOSAB.29.003063.
- [116] K. Peng, Y. Xu, Y. Wu, Y. Yan, S.T. Lee, J. Zhu, Aligned single-crystalline Si nanowire arrays for photovoltaic applications, *Small.* 1 (2005) 1062–1067. doi:10.1002/sml.200500137.
- [117] C.A. Fenstermaker, F.L. McCrackin, Errors arising from surface roughness in ellipsometric measurement of the refractive index of a surface, *Surf. Sci.* 16 (1969) 85–96. doi:10.1016/0039-6028(69)90007-7.
- [118] V. Brusic, M.A. Genshaw, J.O. Bockris, On the possible influence of surface roughening on ellipsometric data in electrochemical studies, *Surf. Sci.* 29 (1972) 653–662. doi:10.1016/0039-6028(72)90243-9.
- [119] S. Boultadakis, S. Logothetidis, S. Ves, Comparative Study of Thin Poly-Si Films Grown by Ion Implantation and Annealing with Spectroscopic Ellipsometry, Raman Spectroscopy, and Electron Microscopy, *J. Appl. Phys.* 72 (1992) 364. doi:10.1063/1.352308.
- [120] H. Fujiwara, S. Fujimoto, M. Tamakoshi, M. Kato, H. Kadowaki, T. Miyadera, H. Tampo, M. Chikamatsu, H. Shibata, Determination and interpretation of the optical constants for solar cell materials, *Appl. Surf. Sci.* (2016). doi:10.1016/j.apsusc.2016.09.113.
- [121] A. Yanguas-Gil, H. Wormeester, Relationship Between Surface Morphology and

- EffectiveMedium Roughness, in: M. Losurdo, K. Hingerl (Eds.), *Ellipsom. Nanoscale*, Springer Berlin Heidelberg, Berlin, Heidelberg, 2013: pp. 179–202. doi:10.1007/978-3-642-33956-1.
- [122] S.J. Fang, W. Chen, T. Yamanaka, C.R. Helms, Comparison of Si surface roughness measured by atomic force microscopy and ellipsometry, *Appl. Phys. Lett.* 68 (1996) 2837. doi:10.1063/1.116341.
- [123] P. Petrik, L.P. Biró, M. Fried, T. Lohner, R. Berger, C. Schneider, J. Gyulai, H. Ryssel, Comparative study of surface roughness measured on polysilicon using spectroscopic ellipsometry and atomic force microscopy, *Thin Solid Films.* 315 (1998) 186–191. doi:10.1016/S0040-6090(97)00349-0.
- [124] P. Petrik, M. Fried, T. Lohner, R. Berger, L.P. Biró, C. Schneider, J. Gyulai, H. Ryssel, Comparative Study of Polysilicon-On-Oxide Using Spectroscopic Ellipsometry, Atomic Force Microscopy, and Transmission Electron Microscopy, *Thin Solid Films.* 313–314 (1998) 259. doi:10.1016/S0040-6090(97)00829-8.
- [125] H. Fujiwara, J. Koh, P. Rovira, R. Collins, Assessment of effective-medium theories in the analysis of nucleation and microscopic surface roughness evolution for semiconductor thin films, *Phys. Rev. B.* 61 (2000) 10832–10844. doi:10.1103/PhysRevB.61.10832.
- [126] H. Fujiwara, M. Kondo, A. Matsuda, Real-time spectroscopic ellipsometry studies of the nucleation and grain growth processes in microcrystalline silicon thin films, *Phys. Rev. B.* 63 (2001) 1–9. doi:10.1103/PhysRevB.63.115306.
- [127] B.A. Sperling, J.R. Abelson, Simultaneous short-range smoothing and global roughening during growth of hydrogenated amorphous silicon films, *Appl. Phys. Lett.* 85 (2004) 3456–3458. doi:10.1063/1.1777414.
- [128] D. Bergström, http://www.mysimlabs.com/surface_generation.html, (2012).
- [129] N. Garcia, E. Stoll, Monte Carlo Calculation for Electromagnetic-Wave Scattering from Random Rough Surfaces, *Phys. Rev. Lett.* 52 (1984) 1798–1801. doi:10.1103/PhysRevLett.52.1798.
- [130] D.E. Aspnes, J.B. Theeten, F. Hottier, Investigation of effective-medium models of microscopic surface roughness by spectroscopic ellipsometry, *Phys. Rev. B.* 20 (1979)

3292–3302. doi:10.1103/PhysRevB.20.3292.

- [131] D. Franta, I. Ohlídal, Comparison of effective medium approximation and Rayleigh-Rice theory concerning ellipsometric characterization of rough surfaces, *Opt. Commun.* 248 (2005) 459–467. doi:10.1016/j.optcom.2004.12.016.
- [132] D. Franta, I. Ohlídal, Ellipsometric parameters and reflectances of thin films with slightly rough boundaries, *J. Mod. Opt.* 45 (1998) 903–934. doi:10.1080/095003498151456.
- [133] A. Yanguas-Gil, B.A. Sperling, J.R. Abelson, Theory of light scattering from self-affine surfaces: Relationship between surface morphology and effective medium roughness, *Phys. Rev. B.* 84 (2011) 85402. doi:10.1103/PhysRevB.84.085402.
- [134] G. Palasantzas, Static and dynamic aspects of the rms local slope of growing random surfaces, *Phys. Rev. E.* 56 (1997) 1254–1257. doi:10.1103/PhysRevE.56.1254.